Few-Cycle and Sub-Cycle Metrology for the Characterization of High Harmonics

by

Erik P. Power

A dissertation submitted in partial fulfillment
of the requirements for the degree of
Doctor of Philosophy
(Electrical Engineering)
in The University of Michigan
2009

Doctoral Committee:

Professor Karl M. Krushelnick, Co-Chair
Professor Louis F. DiMauro, Co-Chair, The Ohio State University
Professor Yue Ying Lau
Professor Duncan G. Steel
Professor Philip H. Bucksbaum, Stanford University

To my beautiful wife Alice, my children Jack and Elizabeth, my parents Max and Marjorie, and a fictional man named Shakey. I love you all.

ACKNOWLEDGEMENTS

First and foremost, I wish to thank my wife, Alice, for all her love and support through many years of trials and tribulations. Without her, none of my efforts would have come to fruition. Thanks also to my parents, Max and Marjorie, for their love, undying belief, and commitment to my success. I wish to thank Prof. Lou DiMauro and Prof. Karl Krushelnick, both of whom stepped into my graduate career at just the right moment and provided the opportunity for me to finish my work in a timely fashion. Thanks to Prof. Duncan Steel, whose sage advice through the years has always helped me keep the ship afloat, and to my other committee members, Prof. Phil Bucksbaum and Prof. Y.Y. Lau.

Much credit is due my colleagues and collaborators in Michigan and around the globe. Dr. Aghapi Mordovanakis, Joe Pentland, James Easter, Pascal Rousseau, Dr. Takeshi Matsuoka, Dr. Steve Reed, Dr. Bixue Hou, Dr. Anatoly Maksimchuk, Dr. Victor Yanovsky, John Nees, Prof. Gerard Mourou, Peter Diehr, and Marc Wilcox were all participants in my efforts at CUOS–thank you all. Dr. Rodrigo Lopez-Martens was instrumental to the success of my split-mirror autocorrelation work, providing me access to the required resources to complete the testing of the device. Thanks also to Dr. Davide Boschetto, Dr. Michele Merano, Dr. Federico Canova, Dr. Thierry Ruchon, and Prof. Anne L'Huillier, each of whom made some contribution. I wish particulary to thank Dr. Christoph Hauri, the only individual to take part in some aspect of all my experimental work and the most astonishingly

productive experimentalist I have encountered.

To my collaborators at Ohio State, I greatly enjoyed the opportunity to work with you, and welcome any opportunity to continue our relationship in the future. Special thanks to Anne Marie March and Emily Sistrunk, who were invaluable to the ultimate success of the mid-IR harmonics XFROG, and also to Cosmin Blaga for his efforts characterizing the self-compressed 2μm pulses. To Dr. Fabrice Catoire, Dr. Gilles Doumy, and Dr. Anthony DiChiara–all I can think to say is that Lou really knows how to choose his post-docs. Thank you all for your intellect and your willingness to contribute towards finding a solution to any problem, no matter the size or complexity. Thanks also to Prof. Pierre Agostini for contributing to my deeper understanding of the subtleties of strong field harmonic generation. Also, I wish to thank Chris Roedig, Jonathan Wheeler, Razvan Chirla, Dr. Ilya Lachko, Dr. Phil Colosimo, and Dr. Kevin Schultz for their contributions and sharp insights. Finally, I must thank Prof. Linn van Woerkom, Dr. Enam Chowdhury, and John Morrison for their generous equipment donations in a pinch–without their help, efforts on the mid-IR harmonics XFROG would have been significantly delayed.

-EPP, Ann Arbor, MI, 2008

TABLE OF CONTENTS

LIST OF TABLES

Table

LIST OF FIGURES

Figure

ABSTRACT

Few-Cycle and Sub-Cycle Metrology for the Characterization of High Harmonics

by
Erik P. Power

Co-Chairs: Karl M. Krushelnick and Louis F. DiMauro

The rapid advances in the generation of ultra-short optical pulses in recent decades have often outstripped the ability of metrologists to accurately measure the pulses' temporal profiles. With each reduction in pulse duration, existing measurement techniques must be re-evaluated and often times partially or completely replaced with newer schemes providing the required temporal sensitivity. Frequency or time-domain metrology performed after a short pulse interaction with a physical system can provide volumes of information about the governing physics of the system. Two new techniques for the temporal characterization of ultra-broadband few-cycle and sub-cycle radiation are presented, along with experimental results and analysis.

A dispersion-free autocorrelator designed to characterize attosecond pulses generated through relativistic laser-plasma interactions is demonstrated. As opposed to all other dispersion-free autocorrelation designs, this device is capable of measuring a linear autocorrelation as well as a nonlinear autocorrelation, and hence is suitable for complete characterization of ultrafast pulses in-situ. Experimental results demonstrate that this autocorrelator produces pulse reconstructions that are

in good agreement with measurements performed using an alternative time-resolved technique.

In the strong-field regime, a cross-correlation frequency-resolved optical gating scheme is presented. The XFROG is designed for characterizing harmonics generated by a scaled system: a $\lambda_0 = 3.6\mu$m laser driving a cesium source. Unlike more widely-used time-domain measurements, this scheme is sensitive to the relative arrival time between harmonic orders. A novel technique employing the XFROG itself to completely characterize the unknown dispersive properties of the cesium heat pipe output window is demonstrated, allowing the removal of the window dispersion from the data and the reconstruction of the harmonics inside the heat pipe. Error analysis demonstrates that the XFROG is sensitive to the relative delay between harmonic orders to within $\pm$180as. The observed negative dispersion on the harmonics' spectral phase and the observed harmonic yield versus frequency are shown to be qualitatively consistent with 1-D time-dependent Schrödinger equation calculations.

Additional measurements are presented demonstrating self-compressed, spectrally broadened pulses emerging from filamentary propagation at both $\lambda_0 = 800$nm and $\lambda_0 = 2\mu$m with high energy transmission. The 2μm self-compressed pulses are shown to maintain carrier-envelope phase stability through the filamentary propagation process with pulse durations < 3 optical cycles.

CHAPTER I

Introduction

Since the 1958 proposal [1] and 1960 demonstration [2] of the laser, investigations of physical phenomena on ever-decreasing time scales have yielded dramatic results. Two years after the first CW laser was reported, it was quickly surpassed in peak power by the development of the Q-switched laser [3], producing pulses with $\tau \sim$ 120ns (120×10^{-9}s) with a peak power of 300kW per beam. Two years later, in 1964, mode-locking was first proposed [4] and then demonstrated [5], with mode-locked pulse duration of $\tau \sim$ 2.5ns. Since then, significant improvements have been made in mode-locking. The current state of the art is a passively mode-locked Kerr-lens Ti:sapphire oscillator which produces a pulse duration $\tau = 4.8$fs (4.8×10^{-15}s) [6].

While mode-locking opens the door for time-resolved studies on the few-femtosecond time scale, the peak power of these pulses is quite low (typically several hundreds of kilowatts). Direct amplification of mode-locked oscillator pulses is useful only up to tens of microjoules, after which the pulse intensity induces a nonlinear response in the amplifier crystal and can ultimately damage the crystal. A seminal moment for science occurred with the advent of chirped pulse amplification (CPA) [7], leading to the wide availability of lasers with pulse durations in the tens of femtoseconds and energies of several millijoules. CPA has also led to the development of lasers with

peak powers in excess of one petawatt (10^{15}W) [8] and access to focused intensities up to $\sim 2 \times 10^{22}\text{W/cm}^2$ [9].

Recent experiments in the strong field regime, where the laser electric field is of the same order as the Coulomb field of the atom [10, 11, 12] ($I \sim 10^{14}\text{W/cm}^2$ for hydrogen) have yielded pulse trains [13] and isolated pulses [14] with duration on the order of hundreds of attoseconds (1as = 10^{-18}s). Synthesized by the coherent addition of multiple high harmonic orders generated by the laser-atom interaction [15], these pulses provide a tool capable of probing dynamics on the time scale of a single Bohr orbit of a bound electron in hydrogen ($\sim$ 150as). Indeed, recent measurements have demonstrated isolated 80as pulses [16].

In the regime of relativistic intensities, defined as intensities where the quiver energy of an electron in the laser field exceeds its rest mass energy, attosecond pulse production is also predicted to occur [17, 18, 19] via laser interaction with an overdense plasma. The threshold for relativistic behavior is usually defined through the normalized vector potential a_0,

$$a_0 = \frac{eE}{m_e \omega c} \tag{1.1}$$

where e is the electron charge, E is the electric field strength, m_e is electron mass, and ω is the laser frequency. The relativistic threshold is defined as $a_0 = 1$, when quiver oscillation of the electron becomes relativistic: $p_{osc} = m_e c$. For 800nm laser light, $a_0 = 1$ corresponds to an intensity $I \simeq 2.16 \times 10^{18}\text{W/cm}^2$. The particle-in-cell simulations that predict the existence of relativistically-produced attosecond pulses also forecasts that these pulses will be extremely efficient, carrying perhaps 10% of the input pulse energy, as opposed to the 10^{-6} efficiency for attosecond pulses generated via strong field interactions at more modest intensities.

For pulses with $>$ 100ps duration, it is possible to measure the pulse duration di-

rectly using a fast photodiode and an oscilloscope. Below the 100ps limit, however, direct electronic measurement becomes difficult, and below $\sim$ 50ps measurements are limited by the bandwidth of the photodiode. Fortunately, great advances have been made in the field of ultrafast metrology. Time-domain interferometry techniques such as autocorrelation and cross-correlation [20, 21, 22] are often used due to the simplicity of experimental setup and versatility when a quick pulse measurement is required or when measuring pulses in a spectral range where more sophisticated techniques are either not possible or too expensive. However, autocorrelations can be ambiguous [23], and thus pulse retrievals from the de-convolution of autocorrelation data must be treated as good estimates only. For most femtosecond applications it is almost always possible to construct a measurement device based on frequency-resolved optical gating (FROG) [24] or spectral phase interferometry for direct electric field reconstruction (SPIDER) [25]. These techniques require more work to set up, but produce more accurate pulse reconstructions. Both schemes have proven to be quite versatile in measuring extremely short pulses: FROG measurements of 4.5fs pulses have been demonstrated [26], as have SPIDER measurements of 5.8fs pulses [27].

The greater part of this thesis treats the development, demonstration, and analysis of two novel schemes for the temporal characterization of few-cycle and sub-cycle ultra-broadband radiation in regimes where traditional measurement techniques either do not exist or are too cumbersome for the target application. A smaller section is dedicated to experiments demonstrating self-compression of short pulses to even shorter duration via filamentary propagation.

1.1 Metrology for Relativistically Generated Attosecond Pulses

The potential for high energy sub-fs pulses with spectra spanning the UV-VIS-NIR range [18] presents significant challenges for ultrafast metrology. The measurement apparatus designed to temporally characterize this transient broadband radiation should ideally be capable of dispersion-free in-situ measurement of the pulses, since propagating the pulses through a window and out of the vacuum adds an unacceptable amount of dispersion. Among the three most commonly used pulse measurement schemes (nonlinear autocorrelation, SPIDER, and FROG), autocorrelation-based measurements require the least experimental setup and provide a reasonable reconstruction of the measured pulses.

With the exception of cross-correlation FROG, all three of the major pulse measurement schemes require the use of a beam splitter to interfere the unknown pulse with either a replica of itself or a spectral shearing field in the presence of a nonlinearity. The requirement that a pulse be split into two nominally equal replicas presents the first of two serious problems in implementing a pulse measurement device for multi-octave spanning pulses. Most commercial beam splitters are either layered dielectric stacks or thin metallic partial reflectors deposited on a glass substrate. Propagation through the substrate was deemed untenable for the application in this thesis; thus, designs built around the most common beam splitter types were discarded. Beam splitter coatings deposited on ultra-thin ($\sim 2\mu$m) pellicles are also available, however the pellicle materials generally do not transmit in the UV region, and their wavefront surface quality is poor.

As an alternative to transmissive beam splitters, spatially dividing the beam into two equal halves (assuming azimuthal symmetry) via reflection from a split mirror is

an attractive alternative. Autocorrelators based on a split mirror [28] with motorization of one mirror to produce a relative delay between the two pulse halves have been used to measure 14fs pulses at $\lambda_0 = 800$nm in an interferometric arrangement [29] and 10fs pulses at $\lambda_0 = 600$nm in a non-collinear geometry [30]. In the attosecond domain, 780as pulses in the XUV spectral region have also been measured using a variation on the split-mirror autocorrelator [31]. It should be noted that an alternate scheme involving the use of a transmission grating as a beam splitter was also proposed [32], however the design and fabrication of the grating is non-trivial and it may not be feasible to obtain a grating with a satisfactory diffraction efficiency over the desired spectral range [33].

Another barrier to the design of an appropriate pulse measurement system is in finding a material with an appropriate nonlinear response. In the IR and visible regions there are two options for obtaining the desired nonlinearity: use a $\chi^{(2)}$ crystal or material with a strong $\chi^{(3)}$ response, or use a large-bandgap photodiode or photoconductive switch. $\chi^{(2)}$ and $\chi^{(3)}$ materials are less attractive due to phase-matching considerations. In order to phase match very broadband spectra, very thin $\sim O(10\mu\text{m})$ samples must be used. Over interaction lengths this short the conversion efficiency into the signal beam is extremely low, and signal-to-noise becomes a significant problem. Two-photon induced photocurrent in a large-bandgap GaAsP photodiode has been successfully used to measure 6fs pulses at $\lambda_0 = 800$nm with a nearly-uniform two-photon response demonstrated over $720\text{nm} - 950\text{nm}$ [34], and at shorter wavelengths a two-photon response from a photoconductive switch built on fused silica has also been demonstrated, measuring 110fs pulses at $\lambda_0 = 267$nm [35]. Recent advances in semiconductor devices have also yielded a new class of solar-blind photodiodes [36] based on III-V compound semiconductors which exhibit an

even larger bandgap than GaAsP diodes, however the use of these devices in a multi-photon response regime has yet to be demonstrated.

1.2 Post-CPA Spectral Broadening and Compression

Filamentary propagation, where light is spatially confined to a self-generated channel by competing focusing and de-focusing effects [37], has received significant attention in recent years as a potential alternative source for high energy few-cycle pulses [38, 39, 40, 41]. In contrast to hollow-core fiber schemes [42], where confinement at high intensity is provided by grazing incidence total internal reflection within a hollow capillary, filamentation-based pulse compressors are insensitive to beam pointing fluctuations and are more easily scaled to millijoule-level energies [43]. The process of filamentary propagation for pulse compression is a balance between the self-action effects of the third-order susceptibility $\chi^{(3)}$ of a bulk medium, ionization, plasma de-focusing, and diffraction. The critical power for self-focusing is given by [44]

$$P_{cr} = \alpha \frac{\lambda^2}{4\pi n_0 n_2} \tag{1.2}$$

where n_0 is the refractive index of the medium and n_2 is the medium's nonlinear refractive index, which is related to $\chi^{(3)}$ via $n_2 = 3\chi^{(3)}_{1111}/4n_0^2\epsilon_0 c$. The parameter α can take a range of values, depending on the beam profile; for a Gaussian beam, $\alpha \approx 1.8962$, a Townes profile has $\alpha \approx 1.86225$, and a 4^{th}-order super-Gaussian has $\alpha \approx 2.0267$. At high intensities, the refractive index of a medium can be modeled as $n = n_0 + n_2 I$. It is quite easy to see that the intensity-dependent refractive index effectively produces a gradient index lens, causing self-focusing of the beam. This same intensity-dependent refractive index also causes self-phase modulation (SPM), whereby the instantaneous frequency of the pulse $\omega(t)$ is modified, giving rise to new

frequency content:

$$\omega(t) = \omega_0 - \frac{2\pi L}{\lambda_0}\frac{\mathrm{d}n(I)}{\mathrm{d}t} \tag{1.3}$$

where L is the propagation distance and λ_0 is the wavelength in free space. In the case of filamentary propagation, the self-focusing of a pulse is arrested when sufficient free electron density has been created via ionization such that the electron plasma contribution to the refractive index approximately counters the contribution from n_2. The pulse then propagates over many Rayleigh lengths in a confined channel, undergoing significant spectral and temporal modification due to SPM (plasma contributions to the nonlinear polarization must also be included). Filamentary propagation terminates when the pulse power has been reduced below the threshold where self-focusing can balance the plasma de-focusing and diffraction. This power loss is a combination of energy loss due to ionization, energy loss due to diffraction, and temporal re-shaping of the pulse. After exiting the filament, a pulse with reduced energy and significantly broader spectrum is observed; the exact amounts of energy loss and spectral broadening / temporal shaping depend on the physical parameters of both the input pulse and the bulk medium chosen. Under the proper conditions the input pulse spectrum can be broadened and compressed to create a pulse duration of less than 3 optical cycles [45, 46, 47, 48]. Under certain circumstances it is even possible to obtain self-compressed pulses, where the need for a complex external compressor is alleviated by the flattening of the spectral phase as the pulse exits filamentary propagation.

1.3 Strong Field High Harmonics in the Scaled System

The study of the strong field processes leading to high harmonic generation have been the subject of intense research since first being reported over two decades

ago [49, 50]. Theoretical modeling using solutions to the time-dependent Schrödinger equation (TDSE) [15] under the single electron approximation [51] predict that the maximum energy for an emitted harmonic photon is given by

$$U_{max} = I_p + 3.17U_p \tag{1.4}$$

where I_p is the ionization potential of the atomic system and the ponderomotive potential U_p is the cycle average of the quiver energy of a free electron in the presence of the driving laser field given by

$$U_p = \frac{e^2E^2}{4m_e\omega_0^2} = 9.33 \times 10^{-14} I\lambda^2 \text{ [eV]} \tag{1.5}$$

and e is electron charge, E is the electric field of the driving laser, m_e is the electron mass, ω_0 is the carrier frequency of the laser, λ is the corresponding laser wavelength in μm and I is the peak laser intensity given in W/cm^2.

The rescattering, or 3-step model [11, 12, 52] provides a quasi-classical view of the strong field process leading to harmonic generation using a three step process. First, the Coulomb barrier of the atom is suppressed by the presence of a strong, slowly varying, linearly polarized laser field. The field modification to the potential creates a barrier with finite width, which allows a ground state valence electron to tunnel through the barrier into the continuum. Once free, the electron propagates classically in the driving laser field. Depending on the initial kinetic energy of the electron and the phase of the driving laser field, a free electron may return to its parent ion, where it can either: (i) miss the ion entirely and continue to propagate, (ii) re-scatter off of the ion either elastically or inelastically, or (iii) re-combine with the core, dropping into the ground state and giving up an $I_p + U_{kinetic}$ photon. For very high laser intensities the initial Coulomb barrier is suppressed below the ground state energy of the valence electron and over-the-barrier ionization [53] dominates.

At intensities where over-the-barrier ionization becomes important, the magnetic $\mathbf{v} \times \mathbf{B}$ component of the Lorentz force becomes non-negligible and the electron trajectory becomes three-dimensional. Consequently, the electron is swept away from its parent ion and misses the core on its return, thus failing to re-combine and emit harmonic radiation. For very low intensities, the barrier suppression provided by the driving laser is insufficient for tunneling to occur, and the dominant mechanism for harmonic generation is given by perturbation theory expansion of the atomic system's susceptibility χ.

The different ionization regimes can be conveniently described by the Keldysh adiabaticity parameter γ [10],

$$\gamma = \frac{\omega_{laser}}{\omega_{tunneling}} = \sqrt{\frac{I_p}{2U_p}} = \frac{\text{tunneling time}}{\text{laser period}} \tag{1.6}$$

where ω_{laser} is the laser frequency and $\omega_{tunneling}$ is the frequency of tunnel ionization. For $\gamma < 1$ the dominant ionization mechanism is tunneling, and for $\gamma > 1$ the dominant process is multi-photon. For $\gamma \sim 1$ the $\mathbf{v} \times \mathbf{B}$ component of the Lorentz force is still negligible, as are relativistic effects, and the larger U_p leads to generation of higher harmonic orders. Under the Keldysh picture different atomic systems excited to equal values of γ should exhibit the same physical behavior. Thus, driving Ar ($I_p = 15.76$eV) at $I = 1.32 \times 10^{14}$W/cm^2 with a $\lambda_0 = 800$nm laser and Cs ($I_p = 3.89$eV) at 1.61×10^{12}W/cm^2 with a $\lambda_0 = 3.6\mu$m laser both produce $\gamma = 1$. The 3.6μm system is a scaled version of the 800nm system and should therefore exhibit a similar single-atom response.

It should also be noted that Eq. 1.5 provides strong motivation for moving to longer wavelength driving lasers [54]. Since U_p scales as λ^2, the expected cutoff energy of the highest order harmonics should correspondingly increase; this wavelength scaling has been observed [55], although it should be noted that electron

wave packet spreading during the longer cycle time of long-wavelength interactions severely reduces the electron-core collision probability, and harmonic production efficiency drops. Also, taking advantage of long-wavelength scaling for U_p may increase the electron velocity enough that the magnetic component of the Lorentz force again becomes important, causing the electron to miss the core on its return [56, 57].

To date, experimental attempts to verify the wavelength scaling in the Keldysh picture have been primarily limited to measuring just the generated harmonics spectra. Earlier work [58] made some attempts to characterize the temporal profile of scaled system harmonics, however in this work the experimental setup used was incapable of measuring the relative phase between harmonic orders. A meaningful measurement of the relative phase between harmonic orders would provide significant insight into the physics of the laser-atom interactions in the scaled system. The relative phase of harmonics in the XUV generated by 800nm light has been measured with a variety of techniques [13, 59, 60, 61].

The strong field approximation (SFA) [62, 63, 64, 65] predicts that below the $I_p + 3.2U_p$ cutoff, two competing electron trajectories exist which lead to harmonic generation; these are coined the short and long trajectories in reference to the amount of time taken by the electron to propagate in the continuum between ionizing and returning to the core. The path taken by an electron is determined by which side of the electric field half-cycle ionizes the electron. Short trajectory electrons all return near the 2^{nd} zero crossing of the electric field following ionization, while long trajectory electrons return at some later time when the field is non-zero. Short and long trajectories are characterized by opposite signs for the dispersion of the harmonics. Harmonics generated by the short path electrons have positive dispersion, while long path trajectories produce harmonics with negative dispersion. In a system

where both trajectories play an active role in harmonic generation, the observed harmonic spectra are distorted by the interference between these two competing paths. It has been demonstrated that the short path can be exclusively selected by placing the gas target slightly after the laser focus, or by using a small aperture to spatially filter the output beam [66, 67, 68].

Two different mechanisms exist to contribute to the observed chirp on the spectral phase of the harmonic radiation. The first is due to the intensity envelope of the laser: due to the non-constant intensity from one cycle to the next, the time between ionization and return/recombination changes as a function of the fixed kinetic energy required to emit a given harmonic order q. The second, called the attochirp, occurs even for CW excitation, and exists due to the differing electron trajectories (different ionization/return times) required for the electron to obtain the kinetic energies needed to emit differing harmonics [69]. For attosecond pulse generation, the presence of the attochirp limits the number of harmonic orders that can be used in pulse synthesis to some optimal number [70]. Since the chirp rate scales as $1/I\lambda$, the use of longer wavelength lasers should also allow for the synthesis of shorter attosecond pulses through the inclusion of more harmonic orders.

Time-resolved studies of scaled system dynamics will provide important insight into the accuracy and applicability of the wavelength scalings predicted in the Keldysh picture. Additionally, study of the scaled system harmonics affords the opportunity to explore harmonics that lie on on the bound-bound transitions below I_p, since these harmonics lie in the UV-VIS-NIR region and are easily accessible with commonly available spectrometers. For scaled system harmonics below I_p, the most fundamental question to be answered before attempting to compare with previous time-domain measurements is to determine the physics behind the generation of the

harmonics. Perturbative harmonics have been observed up to the 15^{th} order [71], thus it is important to first verify that the harmonic generation mechanism is the same strong field process underlying above-threshold harmonic generation.

1.4 Thesis Organization

This dissertation is organized as follows. Chapter II describes a dispersion-free measurement system designed to temporally characterize sub-fs pulses generated through relativistic laser-plasma interactions. The mechanical design and optical layout are detailed, including a new technique which greatly improves the fringe contrast for nonlinear autocorrelations and also provides the system with the ability to collect a 1^{st}-order autocorrelation. Operating procedures for the device are then presented. The next section discusses the autocorrelation functions produced by this interferometer and introduces an approximation that significantly reduces the computational time needed for pulse reconstruction. The adaptive genetic algorithm selected as the functional minimization routine for the pulse retrieval algorithm is then described, and the chapter concludes with a presentation of experimental results and discussion. The work presented in this chapter was published in Ref. [72].

Chapter III presents experimental results demonstrating self-compressed pulses emerging from filamentary propagation. Results at $\lambda_0 = 800$nm are presented first, followed by results at $\lambda_0 = 2\mu$m. The presented 800nm results were published in Ref. [73], and the 2μm results were published in Ref. [74].

Chapter IV is dedicated to time-resolved measurement of high harmonics from a $\lambda_0 = 3.6\mu$m laser. The chapter begins by analyzing the expected pulse energy and spectral content to determine the type of FROG geometry to employ. The design parameters for the nonlinear medium are then discussed, along with the analysis

used to select the proper crystals. The next section describes the layout for the FROG and discusses the various techniques employed to isolate the FROG signal from the background and improve signal-to-noise. The dispersion management techniques used for this measurement are then presented, including a novel method for completely characterizing the dispersive effects of an unknown window and removing its contribution from the data. Alignment and operating procedures are then described. A discussion of the algorithm used to reconstruct the harmonic pulses from the measured FROG traces follows, including the introduction of a new type of constraint employed in the standard retrieval algorithm which dramatically improves the self-consistency and convergence levels of reconstructed pulses across the entire FROG data set. Experimental results are presented, demonstrating the successful operation of the FROG, followed by error analysis. Analysis of the pulses recovered from the FROG data follows. 1-D TDSE simulation results are presented, and the experimental results are shown to compare favorably with these calculations. Analysis of the combined experimental and theoretical results is presented. The work presented in this chapter is under preparation for publication as of the writing of this thesis.

Chapter V provides a summary of experimental results and reiterates the key concepts behind the new time-resolved measurement schemes and the pulse self-compression measurements presented in this thesis. Future experiments making use of these techniques are proposed.

CHAPTER II

All-Reflective Split Mirror Autocorrelator for In-situ Measurement of Ultra-broadband Pulses

The potential high-efficiency relativistic source of attosecond pulses described in Chapter I mandates that new techniques be developed for in-situ time-resolved measurements. Addressing the future need for a dispersion-free pulse measurement device constructed from a minimal number of components, an all-reflective split-mirror autocorrelator using photodiode detection was designed and tested [72]. This chapter details the operational theory, optical layout / mechanical design, alignment procedures, and experimental results. An in-depth discussion of the pulse reconstruction algorithm is provided, along with a technique for reducing the required computation time for pulse reconstruction to an acceptable value, without the use of advanced computing facilities. The device was tested using $\lambda_0 \sim 800$nm pulses with bandwidth supporting ~ 10fs pulses, allowing for the use of a GaAsP photodiode as a second-order detector.

2.1 Autocorrelator Design, Layout, and Operation

The layout for the split mirror autocorrelator is shown in Fig. 2.1. The input pulse, assumed to be linearly polarized and have azimuthal symmetry, is spatially divided into two equal beams using a reflection from a split mirror. One half of the

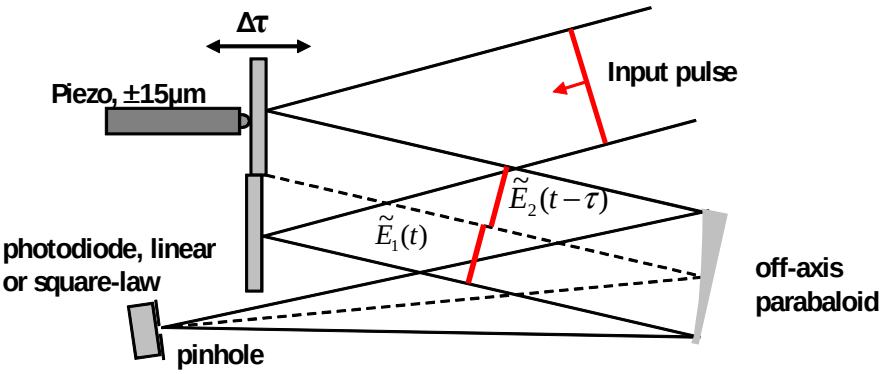

Figure 2.1: Optical layout for the split mirror autocorrelator.

split mirror is actuated by a piezo, affecting a relative delay τ between the two pulse halves. The pulse halves are then focused using an off-axis parabaloidal mirror, and a spatial filter and detector are placed in the focal plane.

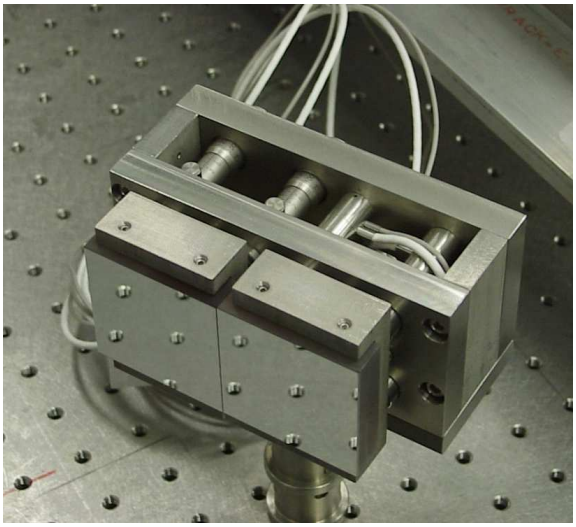

Figure 2.2: Mount for the split mirror.

Fig. 2.2 shows the physical realization of the mount for the split mirror. The mirrors were manufactured using a 4" x 2" x 1/2" Zerodur substrate, chosen for its low thermal expansion coefficient. The substrate was polished to a surface figure of $< \lambda/20$ at 632nm over a 90% clear aperture with 40-20 scratch-dig. After polishing, the mirror blank was cut in two 2" x 2" squares with a chip edge specified at less

than 50μm. The mirrors were then coated with a UV-enhanced aluminum coating, overcoated by an extremely thin 10nm MgF protective layer to prevent oxidation. Since the vendor could not guarantee that every mirror would have no chips to within 50μm of the cut edge, 10 mirrors were ordered, and only the mirrors with the best visible edge quality were selected for experimental use.

The mirror mount was custom fabricated from 303ss stainless steel, the same grade of stainless steel used in the housings for the piezo actuators. The two mirror holders were machined with three grooves on the back surface in a right-triangular arrangement to accept three ball-tip actuators. 0.5mm thick sapphire plates were glued into these grooves to provide a low-friction contact point for the actuator tips.

Both mirror holders are held in place by two springs which each exert an 80N force when extended to the designed operating length. This stronger than usual retention force was selected to minimize the possibility of the mirror holders slipping laterally when an actuator is adjusted. The stationary mirror is actuated by three high resolution micrometers with 0.5μm resolution and a 3-point non-influencing locking mechanism to prevent unintended motion when locking after alignment. The motorized mirror is actuated by three pre-loaded piezo-electric actuators. Each actuator is equipped with an ohmic strain gauge sensor for closed-loop feedback, providing 6Å resolution over a 30μm displacement. For an incidence angle of 20°, this translates to an uncertainty of $\pm$1.9as in the position of each piezo, or $\pm$1.1as RMS uncertainty in the position of the mirror. The use of three piezo actuators allows for ultra-fine tip/tilt control over the motorized mirror, producing a much higher degree of parallelism between the two mirrors than is possible with the manual actuators alone. The focusing mirror is an uncoated Zerodur off-axis parabaloid with a 13° off-axis angle and a focal length of 1.016m. The mirror has a surface figure $< \lambda/20$ at 632nm

and a scratch-dig no worse than 60-40. Original plans were to coat this mirror with UV-enhanced aluminum, however it was determined experimentally that there was almost always a need to reduce the pulse energy by orders of magnitude to avoid detector saturation. It became convenient to use the mirror not only for focusing but also as a beam dump, only focusing the Fresnel-reflected portion of the beam.

A piece of 50μm-thick aluminum foil is used when installing the mirrors into their respective holders. The foil is used to separate the two mirrors and prevent their edges from colliding during coarse alignment. Once the mirrors are secured in their mounts, this foil is removed. The split mirror mount is placed on a linear translation stage with a direction of motion parallel to the surface of the mirrors. The translation stage is moved until the input beam reflects entirely off of the piezo-actuated mirror. A microscope objective is placed to image the focal plane of the parabaloidal mirror onto a CCD. The parabaloid is then aligned using standard alignment techniques. Once aligned, the focal spot looks similar to that shown in Fig. 2.3(a).

Once the parabaloid is aligned, the linear stage is moved so that the beam is cut into two equal halves. Equality between the two pulse halves is defined to be when the total integrated energy, measured by integrating the counts in the CCD image, is equal for both pulse halves. The three piezo actuators are then manually commanded to move to 15μm, or half of their total available displacement. Coarse alignment between the two mirrors is an iterative process to achieve parallelism between the mirrors with zero temporal delay. First, the beam from the manually-actuated mirror is blocked, and the centroid of the CCD image of the pulse half from the piezo-actuated mirror, shown in Fig. 2.3(b), is noted. Next, the beam from the manually-actuated mirror is unblocked and the beam from the piezo-actuated mirror is blocked. The micrometers on the manually-actuated mirror are then adjusted so

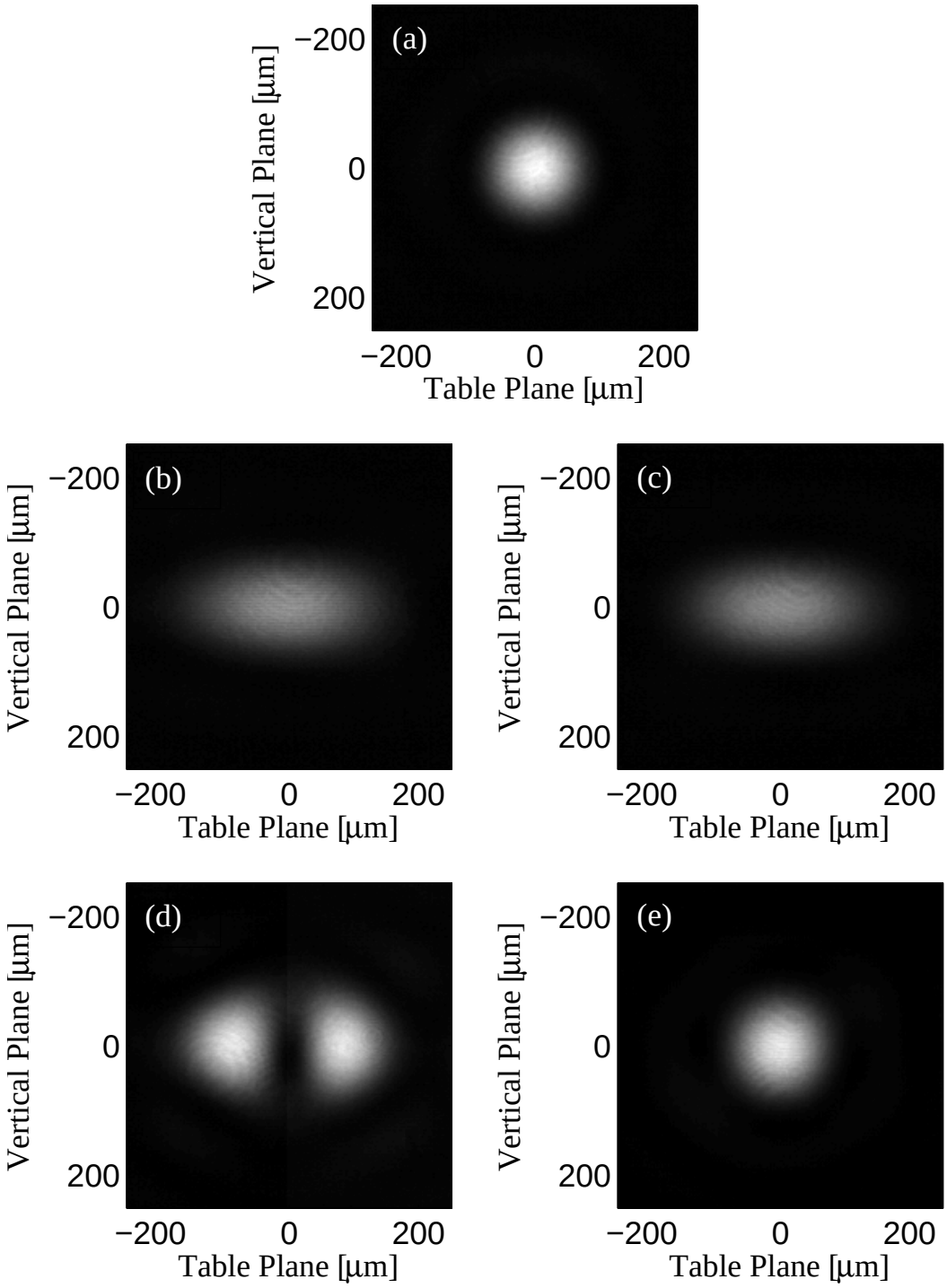

Figure 2.3: Beam profile in the focal plane: (a) focal spot using a single mirror, (b) focal spot for the beam from the piezo-actuated mirror, (c) focal spot for the beam from the manually-actuated mirror, (d) spatial interference pattern with $\tau \sim T/2$ delay, (e) spatial interference pattern with $\tau = 0$ delay. All images are on the same intensity scale and were acquired using $\lambda_0 = 800$nm, $\tau \approxeq 30$fs pulses.

that the centroid of the beam from the manually-actuated mirror falls in exactly the same location as the previously measured centroid, as shown in Fig. 2.3(c). Next, the beam from the piezo-actuated mirror is unblocked, and a check is made for spatial fringes. If the spatial profile observed on the CCD does not change when both beams are allowed through, the temporal separation between the beams must be large, and more adjustment is needed. The manual micrometer responsible for z-axis motion of the manually-actuated mirror is adjusted, and the steps for obtaining spatial overlap are repeated, followed by another check for temporal overlap. Once the delay between the two pulse halves is small, spatial fringes become evident in the CCD image. Near $\tau = 0$ delay, the spatial profile observed on the CCD exhibits one dark fringe with high contrast, which appears to "walk" horizontally across the profile as the delay is adjusted. As shown in Fig. 2.3(d), at a delay of $\tau = \pm T/2$, where T is the laser period, the spatial profile is a two-lobed structure with equal energy in both lobes and a dark fringe in the middle. At $\tau = 0$ the beam profile looks identical to the profile observed when aligning the parabaloid (i.e. using a single mirror instead of a split mirror), shown in Fig. 2.3(e). Mis-alignment of the manually-actuated mirror so that the beams are not collinear up and down results in a tilting of the fringe pattern so that the fringes are no longer vertical. Mis-alignment of the manually-actuated mirror so that the beams are crossing or diverging side-to-side results in multiple vertical fringes, rather than a single fringe.

For longer pulses ($>$ 20fs) it can be difficult to find $\tau = 0$ exactly, since the spatial distribution at $\tau = \pm 3T/2$ or even $\tau = \pm 5T/2$ looks much the same as the distribution at $\tau = \pm T/2$. Thus, it is almost impossible to identify the two-lobed profiles that occur at one-half wave delay in either direction of $\tau = 0$. However, this problem is not too substantial; even if the determination of $\tau = 0$ happens to be off

by 2 waves for $\lambda_0 = 800$nm pulses, this corresponds to a 751nm displacement (at 20° incidence angle) of the piezo-actuated mirror, or only 2.5% of the total displacement range. In practice this means that the autocorrelation traces will not have $\tau = 0$ at exactly the 50% displacement point for the piezos, but the traces will still fit comfortably within the total accessible temporal rage.

It is clear from examination of Fig. 2.3 that placing a detector with a linear response in the focal plane will result in a DC value read from the diode for all delays τ, since all the energy in the original pulse is always present in focus; only the spatial distribution has changed. Furthermore, while a detector with a 2-photon response will certainly produce an interferometric signal as τ is varied, the fringe contrast will be degraded ($\sim$4.6:1 vs 8:1 for a whole-beam interferometer) [29], since the difference in peak intensity between the $\tau = 0$ and $\tau = \pm T/2$ spatial distributions is small. However, it should be noted that the simple addition of a small pinhole at focus solves both of these problems. At delays $\tau = \pm nT/2$, n an integer, the pinhole will be centered on the dark fringe and the energy transmission is minimized as shown in Fig. 2.4(a), while for delays $\tau = \pm nT$ the energy transmission through the pinhole will be maximized, as shown in Fig. 2.4(b). Consequently, it becomes possible to use a linear detector to collect an interferogram (and thus measure the pulses' spectral power) and the fringe contrast for 2^{nd}-order detection is improved to nearly 8:1, the theoretical maximum for an interferometric autocorrelation using a whole beam (Michelson, Mach-Zender, etc.) interferometer.

After the determination of $\tau = 0$ the manual micrometers are locked and the piezos are commanded to the $\tau = T/2$ position. Fine adjustments are then made to the tip and tilt piezos to make the observed spatial interference pattern resemble theory as closely as possible. A pinhole is then placed in an x-y translation mount

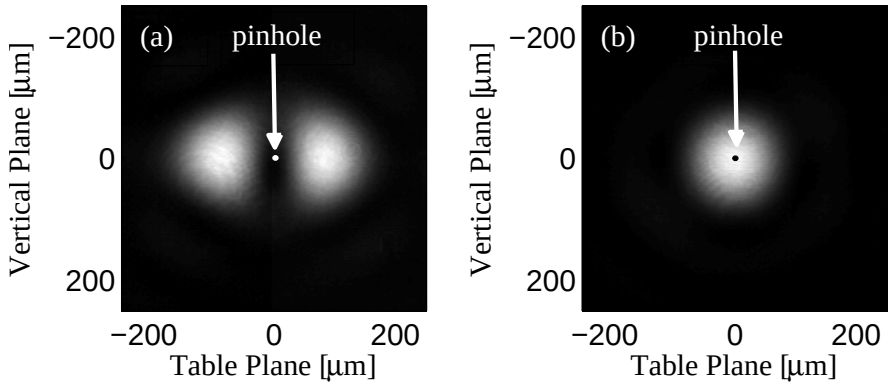

Figure 2.4: Beam profile in the focal plane with 15μm pinhole location superimposed: (a) $\tau \sim T/2$, (b) $\tau = 0$.

and placed in the focal plane (the microscope objective and CCD are left in place). The pinhole is scanned in the x-dimension until the energy collected onto the CCD is maximized, then in the y-dimension to maximize the energy again. After completing this the pinhole is properly positioned in y, but is off-center in x. The pinhole is then scanned in the x-dimension until the energy on the CCD is minimized and increases with motion in either direction in x. The pinhole is now properly positioned, and the objective and CCD are removed. A linear or 2^{nd}-order detector is placed immediately behind the pinhole (as close to the pinhole as is possible) and data collection follows.

2.2 Autocorrelation Functions

Define the light to be measured to be linearly polarized with a Gaussian spatial profile. For a monochromatic Gaussian beam with frequency ω, the fields at focus from each half of the split mirror are described as [29] :

$$\tilde{H}_{1,2}(x,y,\omega) = \frac{i}{\omega}\frac{cf}{\mathrm{w}_0^2(\omega)}\exp\left(-\frac{x^2+y^2}{\mathrm{w}_0^2(\omega)}\right) \times\left\{1 \pm i\frac{2}{\sqrt{\pi}}\frac{x}{\mathrm{w}_0(\omega)}{}_1F_1\left[\frac{1}{2},\frac{3}{2},\left(\frac{x}{\mathrm{w}_0(\omega)}\right)^2\right]\right\} \tag{2.1}$$

where f is the mirror focal length, ${}_1F_1$ is the confluent hypergeometric function, $w_0(\omega)$ is the beam waist in the focal plane in the absence of the split mirror, and the separation between the split mirrors is assumed to be negligible. It is clear that the intensity distribution for both beams is identical; the only difference between the two beams is their phase, as is simulated in Fig. 2.5.

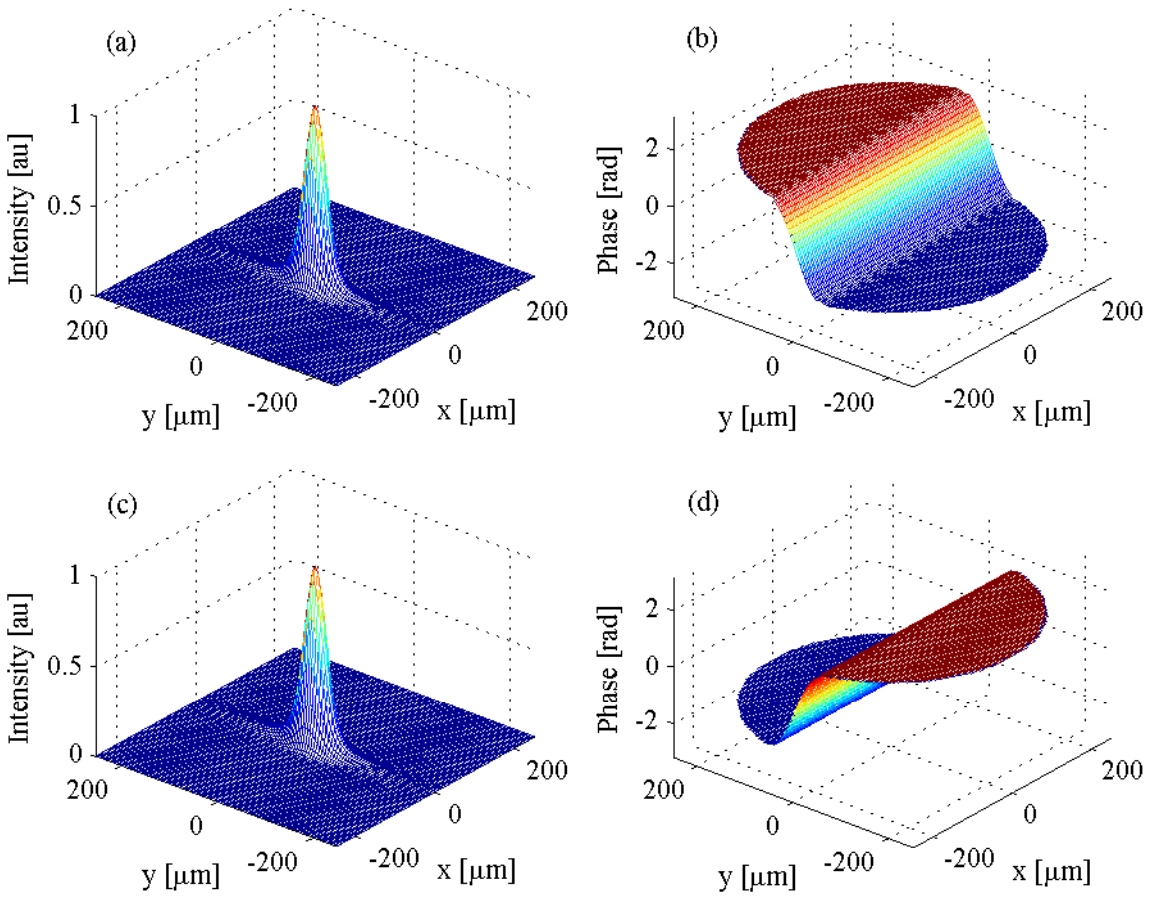

Figure 2.5: Intensity and phase for the two beams described by Eq. 2.1: (a) $|\tilde{H}_1(x,y,\omega)|^2$, (b) $\phi_1(x,y,\omega)$, (c) $|\tilde{H}_2(x,y,\omega)|^2$, (d) $\phi_2(x,y,\omega)$.

At focus, the interference between $\tilde{H}_1(x,y,\omega)$ and $\tilde{H}_2(x,y,\omega)$ is thus clearly seen to be caused by the crossing of two identical beams with oppositely tilted wavefronts. Fig. 2.6 shows the intensity distribution resulting from the interference of $\tilde{H}_1(x,y,\omega)$ with $\tilde{H}_2(x,y,\omega)$.

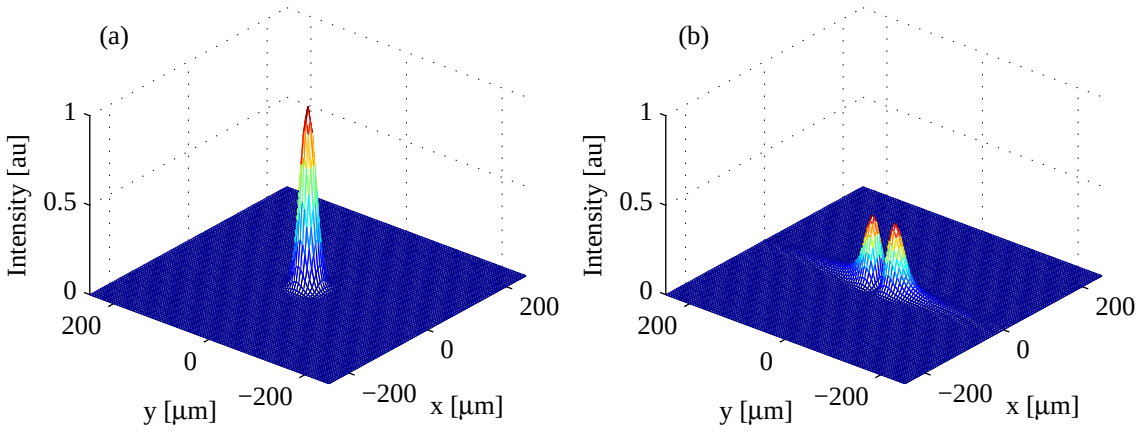

Figure 2.6: Intensity when interfering $\tilde{H}_1(x,y,\omega)$ with $\tilde{H}_2(x,y,\omega)$ for (a) $\tau = 0$ delay, and (b) $\tau = T/2$.

For a polychromatic pulse Eq. 2.1 can be viewed as describing a spatially dependent frequency-domain transfer function, and the fields at focus are expressed as

$$\tilde{E}'_{1,2}(x,y,\omega) = \tilde{E}(\omega)\tilde{H}_{1,2}(x,y,\omega) \tag{2.2}$$

or in the time domain as

$$\tilde{E}'_{1,2}(x,y,t)e^{-i\omega_0 t} = \frac{1}{\sqrt{2\pi}}\int_{-\infty}^{\infty}\tilde{E}(\omega)\tilde{H}_{1,2}(x,y,\omega)e^{-i\omega t}d\omega \tag{2.3}$$

where $\tilde{E}(\omega)$ is the original pulse. Delaying $\tilde{E}'_2(x,y,t)$ by τ, the total field at focus is then expressed as

$$\begin{aligned}\tilde{E}'_1(x,y,t)e^{-i\omega_0 t} + \tilde{E}'_2(x,y,t-\tau)e^{-i\omega_0(t-\tau)} \\ = \frac{1}{\sqrt{2\pi}}\int_{-\infty}^{\infty}\tilde{E}(\omega)\tilde{H}_1(x,y,\omega)e^{-i\omega t}d\omega \\ + \frac{1}{\sqrt{2\pi}}\int_{-\infty}^{\infty}\tilde{E}(\omega)\tilde{H}_2(x,y,\omega)e^{-i\omega(t-\tau)}d\omega\end{aligned} \tag{2.4}$$

2.2.1 First-order Autocorrelation Function

A linear detector immediately behind a pinhole of radius r will collect an interferogram $S_1(\tau)$ as

$$\begin{aligned} S_1(\tau) &= \int_{-r}^{r} dx \int_{-\sqrt{r^2-x^2}}^{\sqrt{r^2-x^2}} dy \int_{-\infty}^{\infty} \left| \tilde{E}_1'(x,y,t)e^{-i\omega_0 t} + \tilde{E}_2'(x,y,t-\tau)e^{-i\omega_0(t-\tau)} \right|^2 dt \\ &= \int_{-r}^{r} dx \int_{-\sqrt{r^2-x^2}}^{\sqrt{r^2-x^2}} dy \int_{-\infty}^{\infty} \left| \tilde{E}_1'(x,y,t) \right|^2 dt \\ &\quad + \int_{-r}^{r} dx \int_{-\sqrt{r^2-x^2}}^{\sqrt{r^2-x^2}} dy \int_{-\infty}^{\infty} \left| \tilde{E}_2'(x,y,t-\tau) \right|^2 dt \\ &\quad + 2\mathrm{Re}\left[\int_{-r}^{r} dx \int_{-\sqrt{r^2-x^2}}^{\sqrt{r^2-x^2}} dy \int_{-\infty}^{\infty} \tilde{E}_1'(x,y,t)\tilde{E}_2'^{*}(x,y,t-\tau)e^{-i\omega_0\tau} dt \right] \end{aligned} \tag{2.5}$$

Adopting the normalization

$$\int_{-r}^{r} dx \int_{-\sqrt{r^2-x^2}}^{\sqrt{r^2-x^2}} dy \int_{-\infty}^{\infty} \left| \tilde{E}_{1,2}'(x,y,t) \right|^2 dt = \frac{1}{2} \tag{2.6}$$

Eq. 2.5 becomes

$$S_1(\tau) = 1 + \mathrm{Re}\left[\int_{-r}^{r} dx \int_{-\sqrt{r^2-x^2}}^{\sqrt{r^2-x^2}} dy \int_{-\infty}^{\infty} \tilde{E}_1'(x,y,t)\tilde{E}_2'^{*}(x,y,t-\tau)e^{-i\omega_0\tau} dt \right] \tag{2.7}$$

Applying the cross-correlation theorem [75], the Fourier transform of Eq. 2.7 yields

$$\mathfrak{F}\big[S_1(\tau) - 1\big] = \mathrm{Re}\left[\int_{-r}^{r} dx \int_{-\sqrt{r^2-x^2}}^{\sqrt{r^2-x^2}} dy \tilde{E}_1'(x,y,\omega)\tilde{E}_2'^{*}(x,y,\omega) \right] \tag{2.8}$$

Substituting Eq. 2.2 and noting $\tilde{H}_1(x,y,\omega) = \tilde{H}_2^{*}(x,y,\omega)$,

$$\begin{aligned} \mathfrak{F}\big[S_1(\tau) - 1\big] &= \mathrm{Re}\left[\int_{-r}^{r} dx \int_{-\sqrt{r^2-x^2}}^{\sqrt{r^2-x^2}} dy \tilde{E}(\omega)\tilde{H}_1(x,y,\omega)\tilde{E}^{*}(\omega)\tilde{H}_2^{*}(x,y,\omega) \right] \\ &= \left|\tilde{E}(\omega)\right|^2 \mathrm{Re}\left[\int_{-r}^{r} dx \int_{-\sqrt{r^2-x^2}}^{\sqrt{r^2-x^2}} dy \tilde{H}_1^2(x,y,\omega) \right] \end{aligned} \tag{2.9}$$

Re-arranging, we see that the spectral power $\left|\tilde{E}(\omega)\right|^2$ can be exactly obtained from the interferogram $S_1(\tau)$ using

$$\left|\tilde{E}(\omega)\right|^2 = \frac{\mathfrak{F}\left[S_1(\tau) - 1\right]}{\mathrm{Re}\left[\int_{-r}^{r} dx \int_{-\sqrt{r^2-x^2}}^{\sqrt{r^2-x^2}} dy \tilde{H}_1^2(x,y,\omega)\right]} \tag{2.10}$$

With the exception of the denominator, this expression is identical to that obtained with a whole beam interferometer [21].

2.2.2 Second-order Autocorrelation Function

A detector with a purely quadratic response inserted behind a pinhole of radius r will collect a second-order autocorrelation $S_2(\tau)$ according to

$$S_2(\tau) = 1 + 2A_0(\tau) + 2\mathrm{Re}\left[A_1(\tau)e^{-i\omega_0\tau}\right] + \mathrm{Re}\left[A_2(\tau)e^{-i2\omega_0\tau}\right] \tag{2.11}$$

where

$$\begin{aligned}
A_0(\tau) &= \int_{-r}^{r} dx \int_{-\sqrt{r^2-x^2}}^{\sqrt{r^2-x^2}} dy \int_{-\infty}^{\infty} I_1'(x,y,t) I_2'(x,y,t-\tau) dt \\
A_1(\tau) &= \int_{-r}^{r} dx \int_{-\sqrt{r^2-x^2}}^{\sqrt{r^2-x^2}} dy \int_{-\infty}^{\infty} \left[I_1'(x,y,t) + I_2'(x,y,t-\tau)\right] \\
&\qquad \times \tilde{E}_1'(x,y,t)\tilde{E}_2'^{*}(x,y,t-\tau) dt \\
A_2(\tau) &= \int_{-r}^{r} dx \int_{-\sqrt{r^2-x^2}}^{\sqrt{r^2-x^2}} dy \int_{-\infty}^{\infty} \tilde{E}_1'^2(x,y,t)\tilde{E}_2'^{*2}(x,y,t-\tau) dt
\end{aligned} \tag{2.12}$$

and we define

$$I_{1,2}'(x,y,t) = \left|\tilde{E}_{1,2}'(x,y,t)\right|^2 \tag{2.13}$$

and adopt the normalization

$$\int_{-r}^{r} dx \int_{-\sqrt{r^2-x^2}}^{\sqrt{r^2-x^2}} dy \int_{-\infty}^{\infty} I_{1,2}'^2(x,y,t) dt = 1 \tag{2.14}$$

As with the first-order autocorrelation, the expression for the second-order autocorrelation in Eq. 2.11 and Eq. 2.12 is identical to that obtained with a whole beam interferometer [22], with the exception of the additional integration over x and y for each of the three terms A_0, A_1, and A_2. Unfortunately, Eq. 2.11 and Eq. 2.12 cannot be used to retrieve the spectral phase without supercomputing capabilities; iterative phase-retrieval techniques require the evaluation of the second-order autocorrelation function hundreds of times to refine the spectral phase. The exact expression for the second-order autocorrelation requires the discretization of the area within the pinhole to N points per unit radius in both the x and y dimensions. For each evaluation of the second-order autocorrelation function, the $S_2(x, y, \tau)$ response must first be computed at each sample point, and the results must then be integrated spatially to yield the desired result. Such an operation requires $O(N^2)$ computations of $S_2(x, y, \tau)$ responses to yield a single evaluation of $S_2(\tau)$. Thus an approximation is needed to reduce the problem to a size manageable on average-quality laboratory computers.

The approximation is as follows: if $r \ll \mathrm{w}_0$, we assume that the response at some point (x, y), $y \neq 0$ within the pinhole area is simply an amplitude-weighted copy of the response at $(x, 0)$. Under this assumption, the integral over y can be wholly attributed to the transfer functions $\tilde{H}_{1,2}(x, y, \omega)$ and only need be computed one time, resulting in a set of dimensionally-reduced transfer functions

$$\begin{aligned}\tilde{H}'_{1,2}(x,\omega) = \sqrt[4]{\alpha(x,\omega)}\sqrt{T(\omega)}\frac{i}{\omega}\frac{cf}{\mathrm{w}_0^2(\omega)}\exp\left(\frac{-x^2}{\mathrm{w}_0^2(\omega)}\right) \\ \times\left\{1 \pm i\frac{2}{\sqrt{\pi}}\frac{x}{\mathrm{w}_0(\omega)}{}_1F_1\left[\frac{1}{2},\frac{3}{2},\left(\frac{x}{\mathrm{w}_0(\omega)}\right)^2\right]\right\}\end{aligned} \tag{2.15}$$

where

$$\alpha(x,\omega) = \frac{1}{2}\sqrt{\pi}\mathrm{w}_0(\omega)\mathrm{erf}\left(\frac{2\sqrt{r^2-x^2}}{\mathrm{w}_0(\omega)}\right) \tag{2.16}$$

and $T(\omega)$ is the spatially integrated power transmission through the pinhole at each frequency ω, used as a normalization term.

Replacing $\tilde{H}_{1,2}(x, y, \omega)$ in Eq. 2.3 with $\tilde{H}_{1,2}(x, \omega)$ from Eq. 2.15 and re-deriving the second-order autocorrelation function, we again find that

$$S_2(\tau) = 1 + 2A_0(\tau) + 2\mathrm{Re}\big[A_1(\tau)e^{-i\omega_0\tau}\big] + \mathrm{Re}\big[A_2(\tau)e^{-i2\omega_0\tau}\big] \tag{2.17}$$

with new definitions for A_0, A_1, and A_2:

$$\begin{aligned} A_0(\tau) &= \int_{-r}^{r} dx \int_{-\infty}^{\infty} I_1'(x,t) I_2'(x,t-\tau) dt \\ A_1(\tau) &= \int_{-r}^{r} dx \int_{-\infty}^{\infty} \big[I_1'(x,t) + I_2'(x,t-\tau)\big] \tilde{E}_1'(x,t) \tilde{E}_2'^{*}(x,t-\tau) dt \\ A_2(\tau) &= \int_{-r}^{r} dx \int_{-\infty}^{\infty} \tilde{E}_1'^{2}(x,t) \tilde{E}_2'^{*2}(x,t-\tau) dt \end{aligned} \tag{2.18}$$

and we define

$$I_{1,2}'(x,t) = \big|\tilde{E}_{1,2}'(x,t)\big|^2 \tag{2.19}$$

and adopt the normalization

$$\int_{-r}^{r} dx \int_{-\infty}^{\infty} I_{1,2}'^{2}(x,t) dt = 1 \tag{2.20}$$

The size of the problem is further reduced by taking advantage of the symmetry $S_2(-x, y, \tau) = S_2(x, y, -\tau)$ for all points (x, y) within the pinhole area, $x \neq 0$. Application of this symmetry allows us to reduce the limits of integration in the x-dimension from $[-r, r]$ to $(0, r]$ by adding two new terms to each expression in Eq. 2.18. The first new term is an $x = 0$ term, which must be explicitly added since the observed symmetry is not applied at $x = 0$. The second new term in each expression is almost identical to the original term, integrating over $(0, r]$ in x and

$(-\infty, \infty)$ in t and changing $t-\tau$ terms to $t+\tau$. Terms involving $t+\tau$ need not be explicitly computed; it is sufficient to compute only the $t-\tau$ terms and time-reverse these results to obtain the required $t+\tau$ terms. The final dimensionally-reduced expressions for A_0, A_1, and A_2 are then:

$$
\begin{aligned}
A_0(\tau) &= \int_{-\infty}^{\infty} I_1'(0,t) I_2'(0,t-\tau)\,dt \\
&\quad + \int_{0+}^{r} dx \int_{-\infty}^{\infty} I_1'(x,t) I_2'(x,t-\tau)\,dt \\
&\quad + \int_{0+}^{r} dx \int_{-\infty}^{\infty} I_1'(x,t) I_2'(x,t+\tau)\,dt \\
A_1(\tau) &= \int_{-\infty}^{\infty} \left[I_1'(0,t) + I_2'(0,t-\tau)\right] \times \tilde{E}_1'(0,t)\tilde{E}_2'^{*}(0,t-\tau)\,dt \\
&\quad + \int_{0+}^{r} dx \int_{-\infty}^{\infty} \left[I_1'(x,t) + I_2'(x,t-\tau)\right] \times \tilde{E}_1'(x,t)\tilde{E}_2'^{*}(x,t-\tau)\,dt \\
&\quad + \int_{0+}^{r} dx \int_{-\infty}^{\infty} \left[I_1'(x,t) + I_2'(x,t+\tau)\right] \times \tilde{E}_1'(x,t)\tilde{E}_2'^{*}(x,t+\tau)\,dt \\
A_2(\tau) &= \int_{-\infty}^{\infty} \tilde{E}_1'^{2}(0,t)\tilde{E}_2'^{*2}(0,t-\tau)\,dt \\
&\quad + \int_{0+}^{r} dx \int_{-\infty}^{\infty} \tilde{E}_1'^{2}(x,t)\tilde{E}_2'^{*2}(x,t-\tau)\,dt \\
&\quad + \int_{0+}^{r} dx \int_{-\infty}^{\infty} \tilde{E}_1'^{2}(x,t)\tilde{E}_2'^{*2}(x,t+\tau)\,dt
\end{aligned}
\tag{2.21}
$$

For detectors with a third-order response, a similar derivation will yield a dimensionally-reduced expression for $S_3(\tau)$. However, since experimental tests of the split-mirror autocorrelator using a third-order device were not performed, the exact formulation for $S_3(\tau)$ has been omitted. In theory, for multi-octave spectra it may be the case

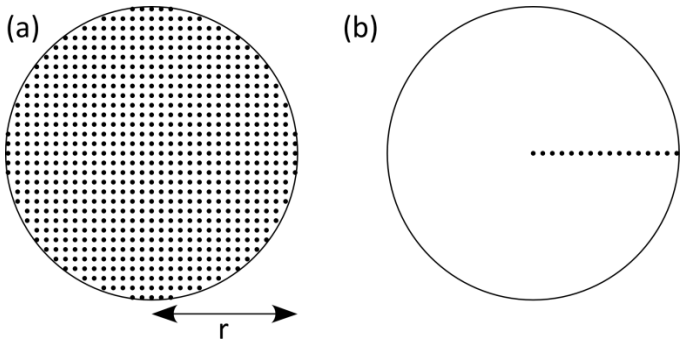

Figure 2.7: Reduction in computation cost for $S_2(\tau)$: (a) Number of points to evaluate $S_2(\tau)$ using Eq. 2.12, and (b) number of points to evaluate $S_2(\tau)$ using Eq. 2.21.

that a chosen detector exhibits a response that is mixed second and third-order. Assuming these responses are linearly independent, it should be possible to perform a pulse reconstruction from autocorrelations taken under such circumstances, given that the relative strengths of the second and third-order responses are known.

As with any approximation, it is important to determine a set of boundary values within which the approximation holds. To test the validity of the approximation, a Gaussian test pulse was created with a carrier wavelength of 745nm and enough bandwidth to support 3.7fs pulses in the transform limit. A mild chirp was added to stretch the pulse to 5.27fs. Fig. 2.8 shows the frequency and time-domain representations of the generated test pulse.

Using Eq. 2.11 and Eq. 2.12, $S_2(\tau)$ was computed through brute force for a variety of initial beam diameters and pinhole sizes, keeping a fixed focal length of $f = 1.016$m. A step size of 10nm was used in both the x and y dimensions to ensure adequate sampling of the second-order response at the highest frequencies contained in the pulse spectrum. Then, using the approximated values for A_0, A_1, and A_2 from Eq. 2.21, $S_{2,trial}(\tau)$ was computed while varying one additional parameter: the sampling density per unit radius.

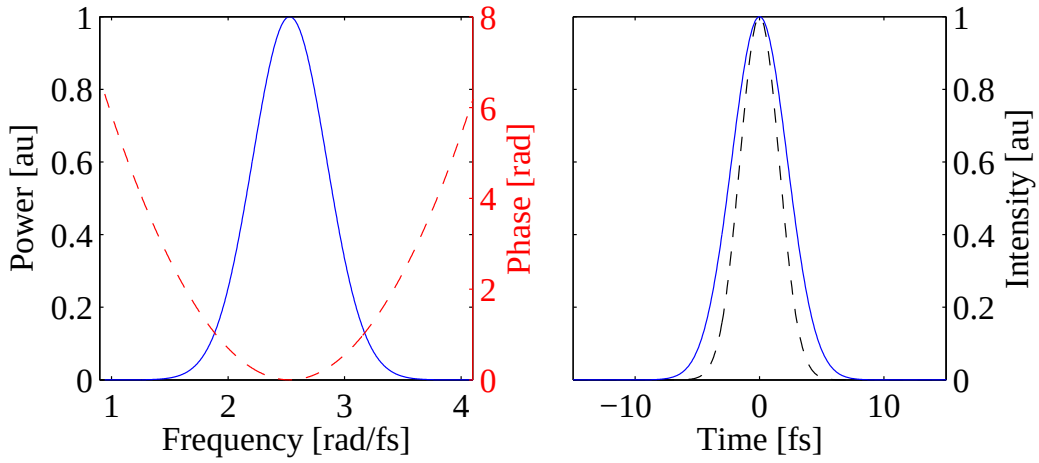

Figure 2.8: Test pulse used to check approximation validity. (a) spectrum (blue, solid) and phase (red, dashed): $\omega_0 = 2.5288$rad/fs (745nm), $\Delta\omega = 0.8981$rad/fs (264.5nm). (b) intensity (blue, solid): $\tau = 5.27$fs, and transform-limited intensity (black, dashed): $\tau = 3.70$fs.

$S_{2,trial}(\tau)$ was compared to $S_2(\tau)$ using the RMS error defined as

$$\Delta = \sqrt{\frac{1}{N}\sum_{i=1}^{N}\left(S_2(\tau_i) - S_{2,trial}(\tau_i)\right)^2} \tag{2.22}$$

Fig. 2.9 shows the simulation results for a selected subset of trials. For whole-beam interferometers, an RMS error between the measured second-order autocorrelation and the autocorrelation computed from the measured spectrum and trial phase of $\Delta \leq 0.003$ is generally accepted to indicate convergence [22] to the correct phase. With this in mind, an upper limit for Δ introduced by the approximated autocorrelation functions was set at $\Delta \leq 0.001$. The simulations reveal that the error introduced by the use of the reduced formulation of the transfer functions is relatively invariant to the density of sample points per unit radius. Of much greater importance is the ratio $r/\mathrm{w}_0(\omega_h)$, which was found to be a strong predictor of the approximation's ability to meet the criteria $\Delta \leq 0.001$. For all cases tested, choosing $r/\mathrm{w}_0(\omega_h) < 0.1$ resulted in $\Delta \leq 0.001$ whenever the sampling density per unit radius was 5 points or greater. The highest frequency in the pulse ω_h is defined to be the largest frequency with a spectral power of at least 1% of the peak power. For these simulations, this

frequency corresponds to a wavelength of 483.3nm.

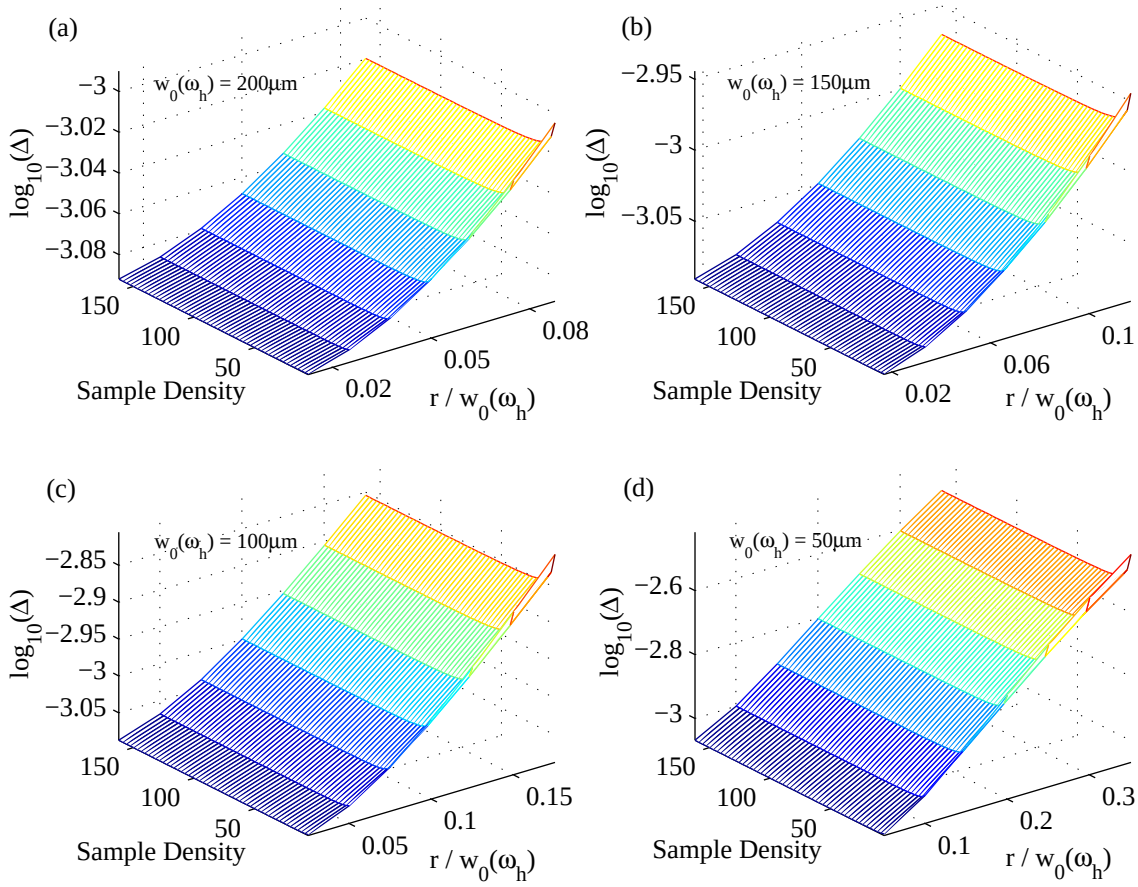

Figure 2.9: RMS Error between $S_2(\tau)$ computed from Eq. 2.12 and $S_{2,trial}(\tau)$ computed from Eq. 2.21 as a function of the ratio of pinhole diameter over the beam waist diameter $\mathrm{w}_0(\omega_h)$ at the highest frequency in the pulse and number of samples chosen per unit radius within the pinhole: (a) $\mathrm{w}_0(\omega_h) = 200\mu$m, (b) $\mathrm{w}_0(\omega_h) = 150\mu$m, (c) $\mathrm{w}_0(\omega_h) = 100\mu$m, and (d) $\mathrm{w}_0(\omega_h) = 50\mu$m.

Thus, for a weak-focusing geometry it is easy to choose a pinhole of appropriate size to satisfy $r/\mathrm{w}_0(\omega_h) < 0.1$, given some good initial guesses about the spectral content and beam diameter of the pulses to be measured. The observed invariance to sampling density has a favorable result, in that during the phase retrieval process it is only necessary to compute $S_2(x,\tau)$ responses at 5 points along the x-axis per calculation of $S_2(\tau)$. While the number of calculations required to test each trial phase is ~ 5 times greater than for a whole-beam interferometer, these simulations

show that with a bit of care the approximated transfer functions can be used without the introduction of significant error. Furthermore, a factor of 5 increase in the number of computations is still well within reason for most laboratory computers.

As is the case with a whole-beam interferometer, a second-order split mirror autocorrelation suffers from the problem of time reversal symmetry. Thus, it is impossible to distinguish between the pulses $\tilde{E}(t)e^{i\omega_0 t}$ and $\tilde{E}^*(-t)e^{-i\omega_0 t}$, since both $\left|\tilde{E}(\omega)\right|e^{i\phi(\omega)}$ and $\left|\tilde{E}(\omega)\right|e^{-i\phi(\omega)}$ yield exactly the same result for $S_2(\tau)$. To determine the direction in which time flows it is necessary to provide additional information by either unbalancing the autocorrelator with a well-characterized piece of dispersive material in one of the two halves of the split beam (difficult, but possible), thus cross-correlating two different pulses and breaking the symmetry, or by collecting a third-order autocorrelation, which does not suffer from time-reversal symmetry.

2.3 Spectral Phase Retrieval via an Adaptive Genetic Algorithm

Phase retrieval using measured spectral power (obtained either from a spectrometer or the Fourier transform of the first-order interferometric autocorrelation) and a second or third-order interferometric autocorrelation is always accomplished using an iterative scheme. The most commonly used method, known as PICASO [22], is quite straightforward. Using the measured spectral power $\left|\tilde{E}(\omega)\right|^2$, a trial spectral phase $\phi_{trial}(\omega)$ is applied to create a trial field $\tilde{E}_{trial}(\omega) = \left|\tilde{E}(\omega)\right|e^{i\phi_{trial}(\omega)}$. The trial field is then inserted into the appropriate expression for the measured autocorrelation (from this point, assume a second-order nonlinearity) to create a trial autocorrelation $S_{2,trial}(\tau)$. The trial autocorrelation is then compared to the measured autocorrela-

tion $S_{2,meas}(\tau)$ using the RMS error as the figure of merit:

$$\Delta = \sqrt{\frac{1}{N}\sum_{i=1}^{N}\left(S_{2,meas}(\tau_i) - S_{2,trial}(\tau_i)\right)^2} \tag{2.23}$$

A functional minimization scheme is applied to refine $\phi_{trial}(\omega)$ and reduce Δ. A variety of functional minimization techniques have been applied to the phase retrieval problem, including the Powell's dog-leg method [76], the Simplex method [22, 77], and genetic algorithms [78]. Fig. 2.10 illustrates the steps required under the PICASO phase retrieval scheme.

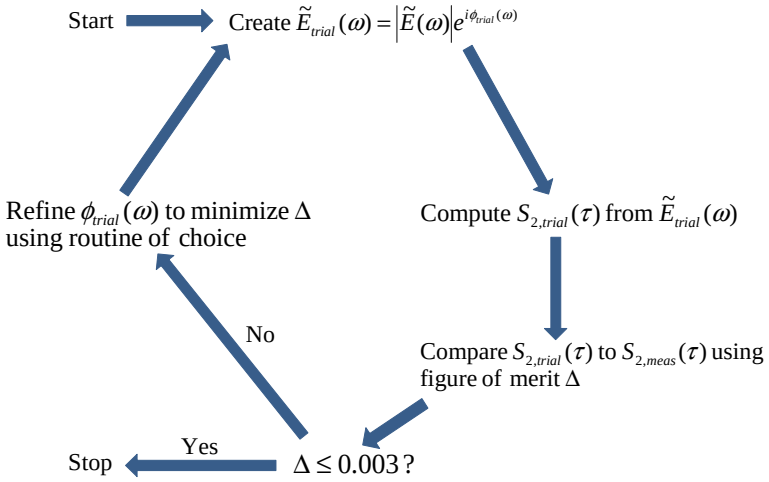

Figure 2.10: Outline of the PICASO algorithm.

For pulse reconstruction from the data collected with the split-mirror autocorrelator, the chosen functional minimization scheme was a modified version of an adaptive genetic algorithm [79].

The basic operation of the adaptive genetic algorithm is as follows: a set (or population, in genetic algorithm nomenclature) of trial spectral phases (each trial phase is known as an individual) is generated as $\Phi(\omega) = \{\phi_k(\omega) : k \text{ an integer} : 1 \leq k \leq N : N \text{ selected by the user}\}$. Typically, $N = 100$ is chosen for the sake of genetic diversity. For each ϕ_k in $\Phi(\omega)$, a trial field is created using the measured spectral power $\left|\tilde{E}(\omega)\right|^2$, creating a set of trial fields $\tilde{\mathbf{E}}(\omega) = \{\tilde{E}_k(\omega) : \tilde{E}_k(\omega) =$

$\left|\tilde{E}(\omega)\right|e^{i\phi_k(\omega)}\}$. The autocorrelation function is then computed for each trial field, creating a set $\mathbf{S}_{2,trial}(\tau)$ as $\tilde{\mathbf{E}}(\omega) \longmapsto \mathbf{S}_{2,trial}(\tau)$. The autocorrelation corresponding to each trial is then compared to the measured autocorrelation, creating the set $\boldsymbol{\Delta}$ as $\{\mathbf{S}_{2,trial}(\tau), S_{2,meas}(\tau)\} \longmapsto \boldsymbol{\Delta}$. $\boldsymbol{\Delta}$ is sorted in descending order, and a linear probability density function for selection as a parent $\mathbf{P}_{sel,k}$ is generated:

$$\mathbf{P}_{sel,k} = 1 + \frac{\langle \boldsymbol{\Delta} \rangle - \boldsymbol{\Delta}_k}{\langle \boldsymbol{\Delta} \rangle - \min(\boldsymbol{\Delta})} \tag{2.24}$$

All values $\mathbf{P}_{sel,k} < 0$ are set equal to zero, thus ensuring that individuals whose values of Δ were a factor of two or larger than $\langle \boldsymbol{\Delta} \rangle$ are excluded from consideration as candidates to parent new individuals.

A new population of N trial phases is generated from the existing generation using genetic operators which modify the information contained in the genes of each parent to create $N - 10$ new individuals, or children. The 10 best individuals in the current generation are preserved and copied to the next generation to ensure that a copy of the best genetic material is maintained across generations. To create a new individual from the existing population, a genetic operator is selected, which dictates the number of parents needed to create the new individual. To select a parent, a random number l is generated in the range $0 < l \leq \sum_k \mathbf{P}_{sel,k}$, and the k^{th} individual is selected using the cumulative distribution function $\mathbf{C}_{sel}$ generated from $\mathbf{P}_{sel}$ by finding the lowest integer k such that

$$\mathbf{C}_{sel,k} = \sum_{j=1}^{k} \mathbf{P}_{sel,j} \geq l \tag{2.25}$$

The genes for each individual depend on the choice for parametrization of the spectral phase. This algorithm provides two options for parametrization of the phase: a polynomial representation, where $\phi_k(\omega) = \sum_{l=2}^{M} \phi_{l,k}(\omega - \omega_0)^l$, $M \geq 2$ a user-selected integer; the genes for individual k are the polynomial coefficients

$\phi_{l,k}$. As an alternate parametrization, the phase for an individual k can be represented directly in phase space using a set of phase values $\phi_{k,phase\ genes} = \{\phi_{k,n}(\omega_n) : n \text{ an integer} : \min(\omega) \leq \omega_{n=1} : \omega_{n=M} \leq \max(\omega) : 1 \leq n \leq M : M \text{ an integer} \leq N : N \text{ is the length of the phase vector } \phi_k(\omega)\}$. Each individual $\phi_k(\omega)$ is then constructed from its genes $\phi_{k,phase\ genes}$ using cubic spline interpolation [80]. For each run of the algorithm, a single gene type is selected and used for all individuals; mixed parametrization schemes are not supported within a single population or across generations.

The creation of new genetic material with which to compose new individuals is accomplished through the use of seven genetic operators: 2-point crossover, mutation, averaging, smoothing, sign flip, creep, and random operators. The operations performed by these operators are detailed in Table 2.1. For many of the operators used by the algorithm and for the parent and operator selection processes, random numbers are required to complete the genetic modification. The random number generator used by this algorithm is a Mersenne Twister pseudorandom number generator [81], seeded at run time with the current computer time given in UTC.

Beyond the basic application of the genetic operators to create a new population from the best existing genetic material, the algorithm is adaptive in the sense that it maintains a record of the operators which have most successfully reduced $\min(\mathbf{\Delta})$ over the past three generations and gives these operators a more favorable probability of selection for use in creating the next generation. This record-keeping and probability assignment is accomplished through a system of credits; a higher credit value associated with an operator results in a higher probability of selection. Each time an individual is created, a record is also created which indicates the operator used to create that individual. Once a population has been evaluated and $\mathbf{\Delta}$ com-

Operator	# Parents Used	# Children Generated	Operation Performed
2-point Crossover	2	2	Selects two points at random $\{m_{low}, m_{high} : m_{low} < m_{high}\} \subset \mathbf{M}$, where $\mathbf{M} = \{1, ..., N :$ N is the total # of genes per individual$\}$. Two parents $\phi_j(\omega)$ and $\phi_k(\omega)$, $j \neq k$, are selected, and all genes indexed by the range $[m_{low}, m_{high}]$ are swapped from $\phi_j(\omega)$ to $\phi_k(\omega)$ and vice versa.
Mutation	1	1	Selects a random set of points $\mathbf{m}_{mut} \subset \mathbf{M}$, where $\mathbf{M} = \{1, ..., N :$ N is the total # of genes per individual$\}$. A single parent $\phi_k(\omega)$ is selected, and the genes indexed by $\mathbf{m}_{mut}$ are multiplied by a random factor in the range $[1 - mutval, 1 + mutval]$, where $mutval$ is a user-selected value in the range [0,1). Each modified gene is multiplied by a different random factor.
Averaging	2	1	Selects two parents $\phi_j(\omega)$ and $\phi_k(\omega)$, $j \neq k$, and averages their genes together.
Smoothing	1	1	Spline parametrization only: Selects a single parent $\phi_k(\omega)$ and applies a moving window average to smooth out fast fluctuations. The window has user-selected width m, where $2 \leq m \leq N/2$, and N is the total # of genes per individual.
Sign Flip	1	1	Polynomial parametrization only: Selects a random set of points $\mathbf{m}_{sf} \subset \mathbf{M}$, where $\mathbf{M} = \{1, ..., N :$ N is the total # of genes per individual$\}$. A single parent $\phi_k(\omega)$ is selected, and the genes indexed by $\mathbf{m}_{sf}$ are multiplied by -1.
Creep	1	1	Selects a random set of points $\mathbf{m}_{cr} \subset \mathbf{M}$, where $\mathbf{M} = \{1, ..., N :$ N is the total # of genes per individual$\}$. A single parent $\phi_k(\omega)$ is selected and a small random number in the range $[-crp, crp]$ is added to the genes indexed by $\mathbf{m}_{cr}$, where crp is user-selected. Each modified gene has a different random number added.
Random	1	1	Selects a random set of points $\mathbf{m}_{rnd} \subset \mathbf{M}$, where $\mathbf{M} = \{1, ..., N :$ N is the total # of genes per individual$\}$. A single parent $\phi_k(\omega)$ is selected and the genes indexed by $\mathbf{m}_{rnd}$ are replaced with randomly generated values in the range $(-\pi, \pi]$ for spline parametrization or, for polynomial parametrization, $[-10^n, 10^n]$, where n is the order of the polynomial coefficient for the gene being replaced. Each gene replaced is replaced by a different random value.

Table 2.1: Genetic operators used in the adaptive genetic algorithm

puted, credit is added to the operators in proportion to the operators' success in creating low-Δ individuals. Additionally, the operators that created the parents and

grandparents of the current population are also credited, at a scaled amount. Credit given for the current generation is full credit, while credit for the parent generation is reduced by half, and credit for the grandparent generation is reduced by four. For example, when considering the k^{th} individual in the population, generated by operator l with parent created by operator m and grandparent created by operator n, the credit assignment to each operators' credit $\mathbf{OC}$ is:

$$\begin{aligned}
\mathbf{OC}_l &= \mathbf{OC}_l + \frac{\left|\min(\boldsymbol{\Delta}_{prev}) - \boldsymbol{\Delta}_k\right|^2}{\min(\boldsymbol{\Delta}_{prev})\big(\min(\boldsymbol{\Delta}_{prev}) - \boldsymbol{\Delta}_k\big)} \\
\mathbf{OC}_m &= \mathbf{OC}_m + \frac{\left|\min(\boldsymbol{\Delta}_{prev}) - \boldsymbol{\Delta}_k\right|^2}{2\min(\boldsymbol{\Delta}_{prev})\big(\min(\boldsymbol{\Delta}_{prev}) - \boldsymbol{\Delta}_k\big)} \\
\mathbf{OC}_n &= \mathbf{OC}_n + \frac{\left|\min(\boldsymbol{\Delta}_{prev}) - \boldsymbol{\Delta}_k\right|^2}{4\min(\boldsymbol{\Delta}_{prev})\big(\min(\boldsymbol{\Delta}_{prev}) - \boldsymbol{\Delta}_k\big)}
\end{aligned} \tag{2.26}$$

where $\boldsymbol{\Delta}_{prev}$ is the entire set $\boldsymbol{\Delta}$ from the previous generation, as opposed to $\boldsymbol{\Delta}_k$, which comes from the current generation.

As can be seen from Eq. 2.26, values of $\boldsymbol{\Delta}_k \ll \min(\boldsymbol{\Delta}_{prev})$ result in a maximal value being credited to an operator. For $\boldsymbol{\Delta}_k \lesssim \min(\boldsymbol{\Delta}_{prev})$, a minimal value is added to the operator's credit. For $\boldsymbol{\Delta}_k \gtrsim \min(\boldsymbol{\Delta}_{prev})$, a small value is subtracted from an operator, while for $\boldsymbol{\Delta}_k \gg \min(\boldsymbol{\Delta}_{prev})$, a large value is subtracted from an operator's credit. For the special case of the 2-point crossover operator, two children are created instead of one (the other six operators only generate one child each). As a result, credit given to the 2-point crossover operator is reduced by a factor of two in all cases in Eq. 2.26 to avoid unduely favoring or punishing this operator. During the first three iterations of the algorithm the crediting mechanism is not fully operational, since there have not been enough previous iterations with which to attribute parent or grandparent credits.

Once all operators have been assigned their credits for the current generation,

OC is sorted in ascending order. **OC** is then scaled as

$$\mathbf{OC} = \frac{\mathbf{OC} - \min(\mathbf{OC})}{\max(\mathbf{OC}) - \min(\mathbf{OC})} \tag{2.27}$$

and taken to describe the probability density function for operator selection. To select an operator, a random number l is generated such that $0 < l \leq \sum_{n=1}^{6} \mathbf{OC}_n$ ($1 \leq n \leq 6$ since only six operators are available for any given choice of phase parametrization) and the p^{th} operator is selected using the cumulative distribution function **OCDF** generated from **OC** by finding the lowest integer p such that

$$\mathbf{OCDF}_p = \sum_{n=1}^{p} \mathbf{OC}_n \geq l \tag{2.28}$$

Figure 2.11 illustrates the steps performed by the adaptive genetic algorithm.

The advent of low-cost multi-core processors for personal computing opens up new doors for scientific computing on office workstations or laboratory PCs. Taking advantage of multiple processors or multiple processor cores, however, requires a conscious and concerted effort on the part of the programmer. Many tasks, such as data collection and simple figure creation, do not require multi-threaded support. Other jobs, specifically data analysis or simulations involving large data sets, can

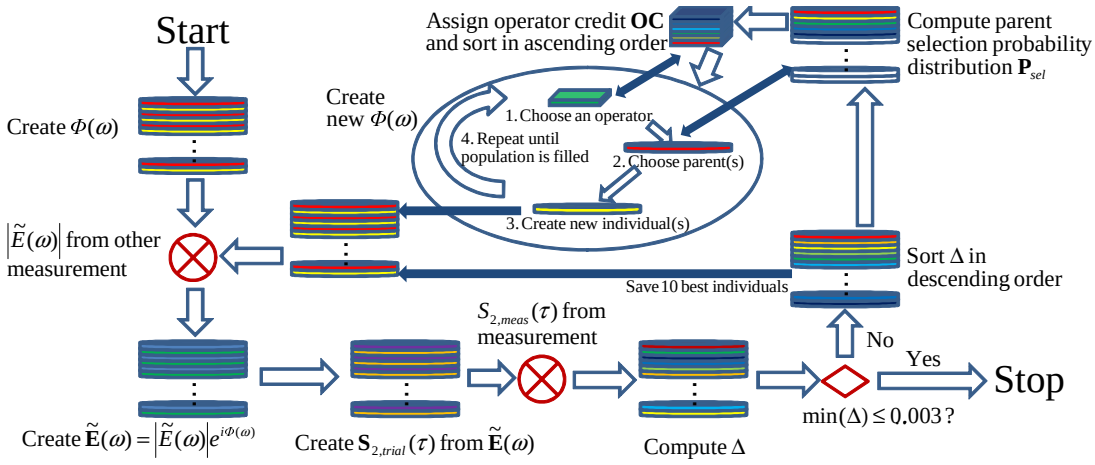

Figure 2.11: Flow diagram for the adaptive genetic algorithm.

greatly benefit from a multi-threaded implementation of the application. Multithreading can be accomplished in many ways; the three most common are multithreading at the function or operator level, as is done in the Intel Math Kernel Library's BLAS, LAPACK, and FFTW implementations [82], multithreading at the loop level, as is possible with technologies such as OpenMP [83], or multithreading at a higher, more abstract level (e.g. the class level) for a more course division of tasks assigned to each thread.

Given the basic nature of the genetic algorithm, a set $\mathbf{\Phi}(\omega)$ of N trial phase parametrizations, the most intuitive choice for the distribution of labor across multiple threads is to break $\mathbf{\Phi}(\omega)$ into M equally-sized subsets, $\{\mathbf{\Phi}^{(1)}(\omega), ..., \mathbf{\Phi}^{(M)}(\omega)\}$. M worker threads are created and each is assigned a subset, with each thread m responsible for completely processing its assigned subset $\mathbf{\Phi}^{(m)}(\omega) \mapsto \mathbf{\Delta}^{(m)}$. To accomplish this, each worker maintains its own local copy of the measured spectral power $\left|\tilde{E}(\omega)\right|^2$ and autocorrelation $S_{2,meas}(\tau)$ to avoid memory access conflicts during processing. Under this scheme, the best choice for choosing a number of workers is to choose $M = \#$ processors. Since this is not commercial code, it is a requirement for this implementation that the total number of trial phases N be an integer multiple of M. In addition to the M worker threads, two additional threads are running: a GUI thread to handle display of the algorithm's progress and accept user input during processing, and a management thread to maintain control over the worker threads. The code is written in C++ and uses the Microsoft Foundation Class (MFC) threading library to initiate and control the various threads.

Fig. 2.12 shows the threading model for the adaptive genetic algorithm. At program start, the user performs all necessary tasks to initialize the algorithm properly: loading of data, selecting a vector size and frequency range, choosing a parametriza-

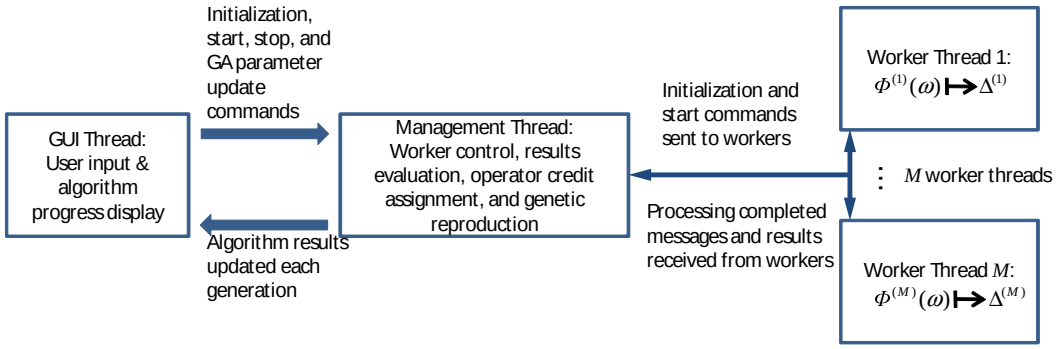

Figure 2.12: Threading model for the adaptive genetic algorithm. The GUI thread handles all user interface functions, while the management thread handles all data processing operations, delegating the process-intensive $\mathbf{\Phi}(\omega) \mapsto \mathbf{\Delta}$ computations to the worker threads.

tion type for the phase genes, choosing a sampling density within the pinhole radius r, and selecting M. Once the user initiates processing, the management thread allocates all necessary resources to comply with the user's choice of settings and spawns the worker threads. The workers then process their respective subsets $\mathbf{\Phi}^{(m)}(\omega)$ and return their results for $\mathbf{\Delta}^{(m)}$ to the management thread, after which the workers idle until they receive another start command. Once all workers have finished their tasks, the management thread combines the results and performs all necessary sorting, credit assignment, and genetic reproduction tasks to create the next generation of trial phases. The worker threads are then issued another start command, and the process repeats until convergence is reached ($\min(\mathbf{\Delta}) \leq 0.003$) or the user terminates the processing. Since the number of genes per trial phase is typically small (about 25 for the spline parametrization and 3-5 for the polynomial parametrization) and the total number of trial phases is also modest (usually 100), it is not necessary to multi-thread the sorting, operator/parent selection, or genetic operator functions. The vast bulk of the processing load is in the evaluation $\mathbf{\Phi}(\omega) \mapsto \mathbf{\Delta}$. As an example, suppose a sampling density of 5 points per unit radius is selected. Then, each evaluation of $S_2(\tau)$ for a single trial phase function requires 80 FFTs and 109 vector

operations. For a population with 100 trial phases it is clear that the evaluation of the fitness of the population must be dominant over simple sorting (performed on a set of 100 numbers) and genetic reproduction functions (performed 90 times on sets of ~ 25 numbers). Multi-threading $\mathbf{\Phi}(\omega) \mapsto \mathbf{\Delta}$ has dramatic results: a single thread processing a 100-individual population with 512-point frequency vector length and a 25-point spline phase parametrization performs at a rate of 1.336 generations/sec on an AMD 2.4GHz dual-core processor. Using the same parameters and splitting the population into two equal 50-individual sub-populations, the processing rate increases to 2.611 generations/sec, a 95.4% improvement in speed.

2.4 Experimental Results

To experimentally test the split-mirror autocorrelator, 3.8mJ pulses at $\lambda_0 =$ 801.1nm with pulse duration $\tau \sim$ 40fs at a repetition rate of 1kHz were spectrally broadened using filamentary propagation [73] in a gas tube filled with argon at $\sim$ 480Torr. The output from the filament had a spectrum supporting 9.58fs pulses with a pulse energy of 1.9mJ at a carrier wavelength of $\lambda_0 = 782.3$nm. After collimation the beam energy was reduced by using two face reflections from fused silica wedges; the beam was then sent into the split mirror autocorrelator at an incidence angle of 20°.

In order to compute the appropriate transfer functions $\tilde{H}_{1,2}(x, \omega)$ needed by the pulse reconstruction algorithm for evaluation of Eq. 2.21, additional information besides the pinhole radius and mirror focal length are required. Specifically, the original beam diameter must be known. Rather than measure this directly, a more accurate measurement can be made during the alignment process by measuring the separation between peaks of the two spatial lobes at a delay $\tau = T/2$ and at a

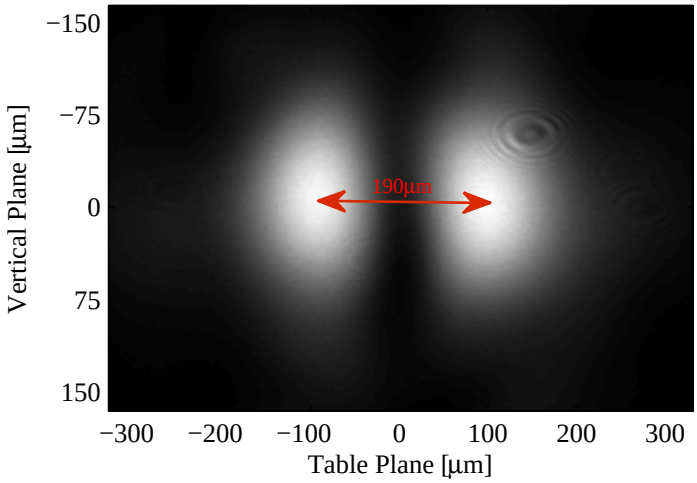

Figure 2.13: Spatial intensity distribution at $\tau = T/2$ and $\lambda = 775$nm used for calibration computation of $\tilde{H}_{1,2}(x, \omega)$. The separation between the peaks of the two lobes was measured to be 190μm.

specific wavelength. The separation between the lobes at a given wavelength is a direct function of the focal length of the parabaloid and the initial beam size. To make this preliminary measurement, an interference filter with a transmission peak at 775nm and FWHM transmission window width specified as 1nm was placed in the beam prior to the split mirror. The measured peak separation, shown in Fig. 2.13, was 190μm, corresponding to an initial beam diameter of $\sim$ 5mm. For the purposes of computing the spectral power $\left|\tilde{E}(\omega)\right|^2$ from a first-order autocorrelation using Eq. 2.10, the full expression for $\tilde{H}_{1,2}(x, y, \omega)$ given by Eq. 2.1 was also computed.

A 15μm diameter pinhole was placed in the focal plane of the parabaloidal mirror and a 1mm^2 silicon photodiode was placed behind the pinhole to collect first-order autocorrelation, shown in Fig. 2.14. The measured interferogram was Fourier transformed to obtain the power spectrum and then corrected according to Eq. 2.10 using a grid size of 10nm in both the x and y dimensions. The uncorrected and corrected power spectra are shown in Fig. 2.15. Examination of the uncorrected and corrected spectra reveal that errors in pulse reconstruction will occur if the effects of the transfer

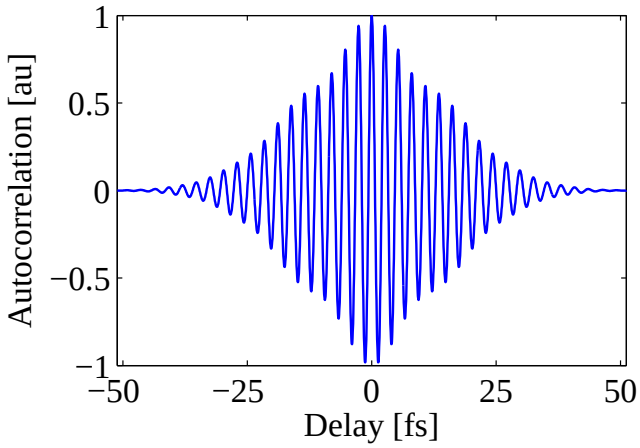

Figure 2.14: Interferogram collected using a 15μm diameter pinhole at focus and a Si photodiode for detection.

functions $\tilde{H}_{1,2}(x, y, \omega)$ are not taken into account: the corrected carrier wavelength is red-shifted by 8.6nm from the value calculated from the Fourier-transformed interferogram, alone, and the relative strength of the blue tail in the spectrum is significantly reduced.

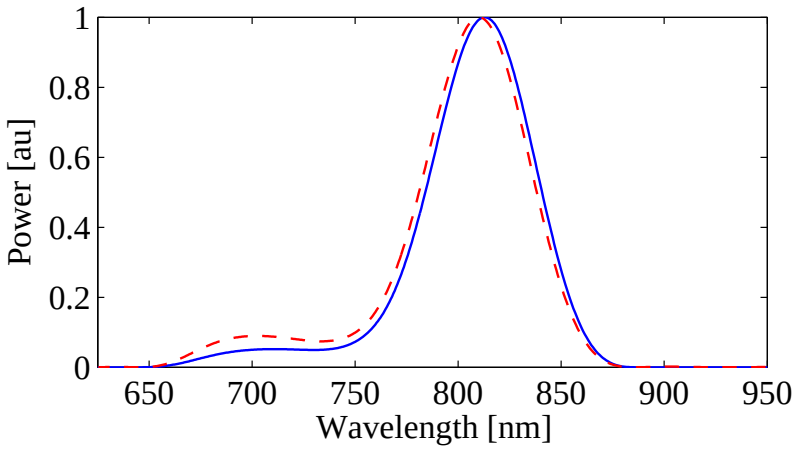

Figure 2.15: Uncorrected (red, dashed) and $\tilde{H}_1(x, y, \omega)$-corrected (blue, solid) power spectra derived from the measured interferogram. Before correction: $\omega_0 = 2.4345$rad/fs (773.7nm), $\Delta\omega = 0.3555$rad/fs (113.0nm). After correction: $\omega_0 = 2.4078$rad/fs (782.3nm), $\Delta\omega = 0.3525$rad/fs (114.5nm).

Following the measurement of the interferogram, the Si photodiode was removed and replaced with a 1mm^2 GaAsP photodiode, which exhibits a second-order re-

sponse over the spectral range contained within the pulse spectrum [34]. The collected second-order interferometric autocorrelation, shown in Fig. 2.16, has a fringe contrast of 7.96:1. After the calculation of $\tilde{H}_{1,2}(x,\omega)$ and the calculation and correc-

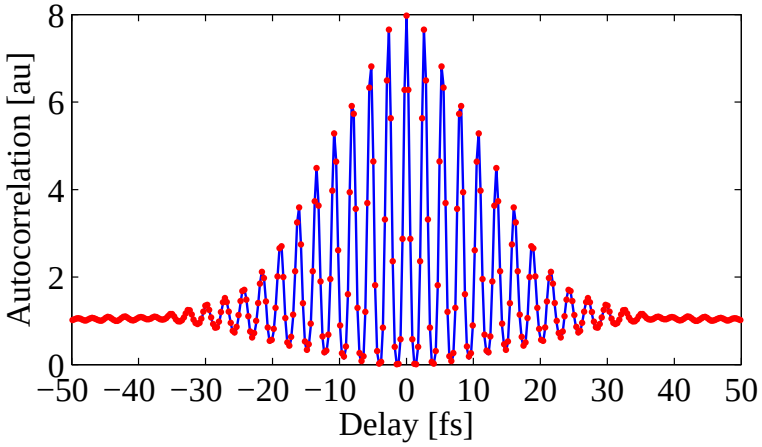

Figure 2.16: Experimental (blue, solid) and retrieved (red, dotted) second-order autocorrelations. The observed fringe contrast was 7.96:1, and the RMS error between the experimental and retrieved autocorrelations was $\Delta = 0.0036$.

tion of $\left|\tilde{E}(\omega)\right|^2$, the measured second-order autocorrelation and pulse spectrum were input into the adaptive genetic algorithm described in Sec. 2.3. The algorithm used a frequency vector length of 512 points with a cubic spline parametrization of the spectral phase containing 31 genes. Fig. 2.17 shows the algorithm's performance.

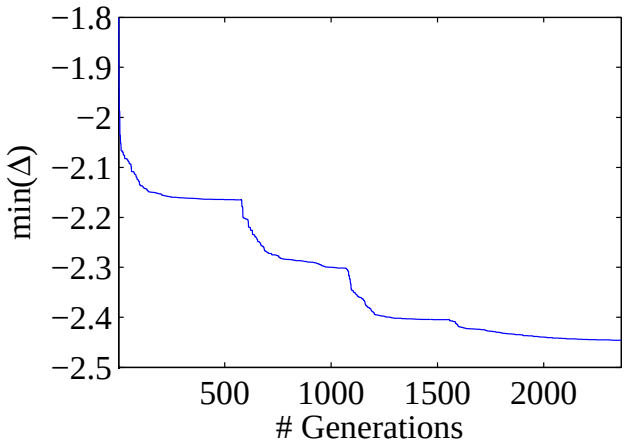

Figure 2.17: Performance of the adaptive genetic algorithm. Plotted is min($\boldsymbol{\Delta}$) (log scale) for each generation.

After nearly 2500 generations, the algorithm reached $\min(\boldsymbol{\Delta}) = 0.0036$, quite close to the value $\Delta \leq 0.003$ desired for phase retrievals from whole-beam interferometric autocorrelations. Fig. 2.18 shows the measured spectral power along with the

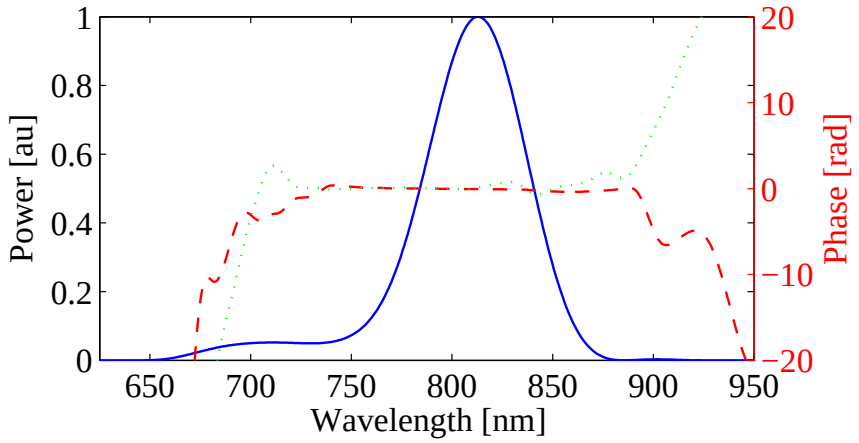

Figure 2.18: Measured spectral power (blue solid), autocorrelation-retrieved spectral phase (red, dashed), and SPIDER-retrieved spectral phase (green, dotted). $\omega_0 = 2.4078$rad/fs (782.3nm), $\Delta\omega = 0.3525$rad/fs (114.5nm).

spectral phase retrieved by the genetic algorithm. Also plotted in Fig. 2.18 is the spectral phase retrieved from an independent SPIDER [25] measurement made on pulses generated under substantively identical experimental conditions (not on the same day, however, due to an unfortunate spectrometer malfunction in the SPIDER). Divergence between the SPIDER and autocorrelation retrievals for the spectral phase in the red and blue regions of the spectrum is to be expected; the SPIDER used a 50μm thick β-BBO crystal cut for type-II phase matching at 800nm. Computation of the phase-matching bandwidth for the o-wave in a 50μm β-BBO crystal using SNLO [84] shows that the crystal is too thick to support the entire pulse spectrum: the calculated phase-matching bandwidth for this crystal is 108.3nm, while the measured bandwidth was 114.5nm (2^{nd} moment bandwidth). In order to properly measure these pulses using a SPIDER, a crystal no thicker than 25μm should be used to ensure efficient sum-frequency generation over the entire spectral range. Despite

this failing, the SPIDER measurement agrees relatively well with the autocorrelation result, and indicates that by pure chance the genetic algorithm happened upon the correct sign for the spectral phase.

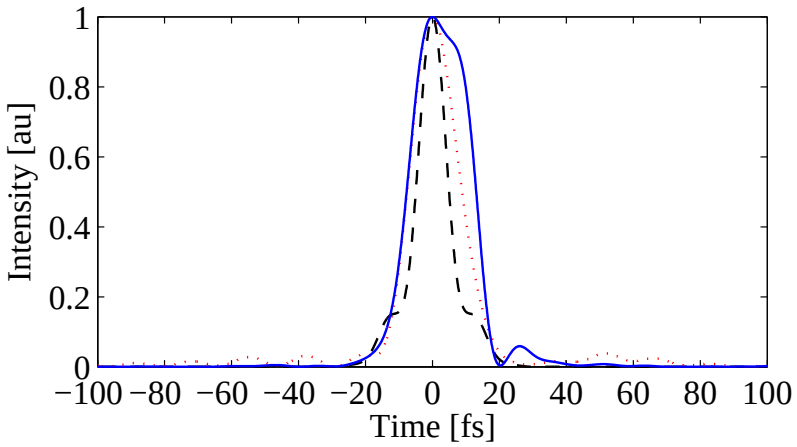

Figure 2.19: Intensity reconstruction using the autocorrelation-retrieved spectral phase (blue, solid), SPIDER-retrieved spectral phase (red, dotted), and the transform limited case (black, dashed). $\tau_{\text{retrieved}} = 20.56\text{fs}$, $\tau_{\text{SPIDER}} = 16.45\text{fs}$, $\tau_{\text{trans. lim.}} = 9.58\text{fs}$.

The reconstructed time-domain intensity profile is shown in Fig. 2.19, along with the SPIDER-retrieved profile and the transform-limited intensity profile. The pulse reconstruction based on the split mirror autocorrelator shows the pulse has a duration $\tau = 20.56\text{fs}$ (FWHM) with a transform limit of 9.58fs. A 5^{th}-order polynomial projection of the spectral phase over the range $[\omega_0 - \Delta\omega/2, \omega_0 + \Delta\omega/2]$, where $\Delta\omega$ is the 2^{nd} moment bandwidth, yields the following values: $\phi_2 = -15\text{fs}^2$, $\phi_3 = 90\text{fs}^3$, $\phi_4 = 93\text{fs}^4$, and $\phi_5 = -954\text{fs}^5$.

CHAPTER III

Spectral Broadening and Self-Compression at 800nm and 2μm via Filamentary Propagation

This chapter details observations of self-compressed pulses at 800nm [73] and 2μm [74]. The 800nm experiments did not, strictly speaking, produce self-compressed pulses. Instead, the pulses exiting the filament were negatively chirped, allowing for the use of a simple slab of glass and a wedge pair to create the necessary positive chirp to compress the pulses. Due to the extreme ease with which these pulses were ultimately compressed, a small license is taken and the pulses are deemed to be self-compressed.

3.1 Self-compression at 800nm

The experimental setup for creating self-compressed pulses at 800nm is shown in Fig. 3.1. A Ti:sapphire laser with $\lambda_0 = 808$nm producing 1.5mJ pulses with $\tau = 41.8$fs and a transform limited duration $\tau = 28.7$fs at 1kHz, as shown in Fig. 3.2, was sent through a 2:1 telescope. A variable hard aperture was used after the telescope to further reduce the beam size, tuning the focal spot size and confocal parameter and attenuating the pulse energy. The appropriate aperture size for a given gas and pressure to observe self-compression was found through trial and error. The beam was then focused with an $f = 1$m spherical mirror into a 1.5m-long gas tube

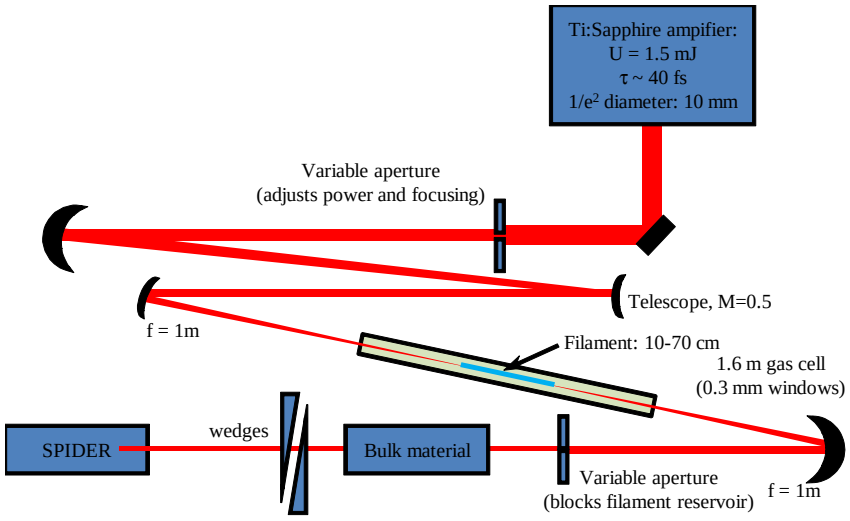

Figure 3.1: Setup.

with 300μm-thick fused silica windows, and re-collimated using an identical spherical mirror at the output side. All reflective optics for this experiment were coated with protected silver. After re-collimation, the outer portion of the beam was filtered with an iris to remove the background white light from the filament reservoir. For dispersion compensation, a 5mm-thick piece of fused silica was inserted into the beam to add 180fs^2 group delay dispersion (GDD), followed by a fused silica wedge pair used to create a variable amount of additional GDD, ranging from 0.5mm added

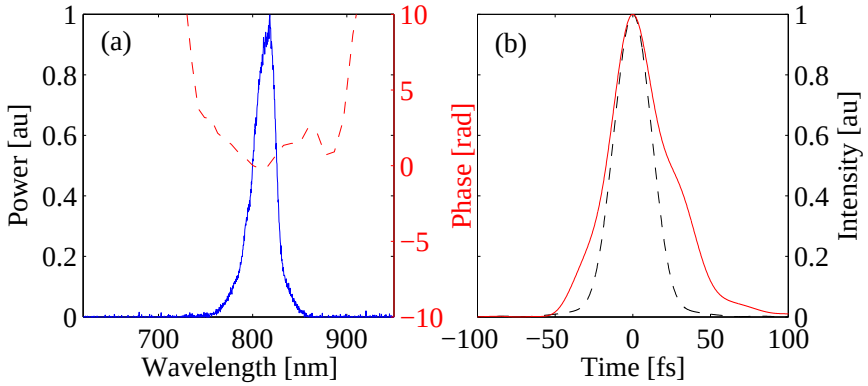

Figure 3.2: Input pulse, measured by inserting a pick-off mirror immediately before the focusing mirror prior to the gas tube and diverting the beam to the SPIDER. (a) Spectral power (blue, solid) and phase (red, dashed): $\lambda_0 = 808.26$nm, $\Delta\lambda = 39.85$nm. (b) Measured intensity (red, solid) $\tau = 41.83$fs and transform limit (black, dashed) $\tau = 28.71$fs.

material ($18fs^2$) to 3mm ($108fs^2$). After compensating the GDD, the pulse was sent to a SPIDER [25] with a 50μm thick type-II BBO crystal cut for phase matching at 800nm.

In all cases where the spectral phase was observed to have near-zero or negative chirp, multiple focusing cycles were observed within the gas tube. Fig. 3.3 shows an example of this behavior. Simulations [85] reveal complex dynamics governing

Figure 3.3: (a) Sequential filament structure in Ar at 870mbar as observed from plasma fluorescence. (b) Spatial mode after re-collimation.

the formation of multiple nonlinear foci and the role played by these sequential filaments in re-shaping the spectral and temporal properties of the pulse. The presence of multiple nonlinear focusing cycles is attributed to the strong spatial dependence to the spectral/temporal pulse distribution near the exit of the first filament; this dependence is shown to be conducive to the formation of another focusing cycle. While these simulations show that multiple nonlinear foci typically correspond to a nearly self-compressed pulse after all filamentary propagation is completed, they fail to demonstrate the net negative group delay dispersion (GDD) observed in experiment; thus, further theoretical work is needed to make sense of the negative GDD observed in the 800nm self-compressed pulses.

3.1.1 Experimental Results

Self-compression for 800nm pulses was observed in four separate gases: Ar, Kr, Xe, and N_2. A summary of SPIDER results for all test cases is shown in Table 3.1. Nonlinear indices for all four gases were deduced from the hyperpolarizability value

$< \gamma >$ from [86], an identical calculation as was performed in [41], adding N_2 to the list of materials for which n_2 was calculated. For argon, the most commonly used gas in hollow-core fiber and filamentary propagation pulse compression schemes, several varying pressures were tried: 470mbar, 870mbar, and 1000mbar. Due to the asymmetric shape of the SPM-broadened spectra observed after filamentary propagation, the standard FWHM computation for bandwidth loses much of its usefulness. As a more reliable method for computing the spectral width, all bandwidths reported were calculated using the 2^{nd} moment about the mean,

$$\Delta\lambda = 2 \times \sqrt{\int_{-\infty}^{\infty} \frac{|S(\lambda)|^{1/2} (\lambda - \lambda_0)^2}{|S(\lambda)|^{1/2}} \mathrm{d}\lambda} \tag{3.1}$$

where $|S(\lambda)|$ is the measured spectral power and λ_0 is the carrier wavelength as computed by the first moment calculation

$$\lambda_0 = \int_{-\infty}^{\infty} \frac{|S(\lambda)|^{1/2} \lambda}{|S(\lambda)|^{1/2}} \mathrm{d}\lambda \tag{3.2}$$

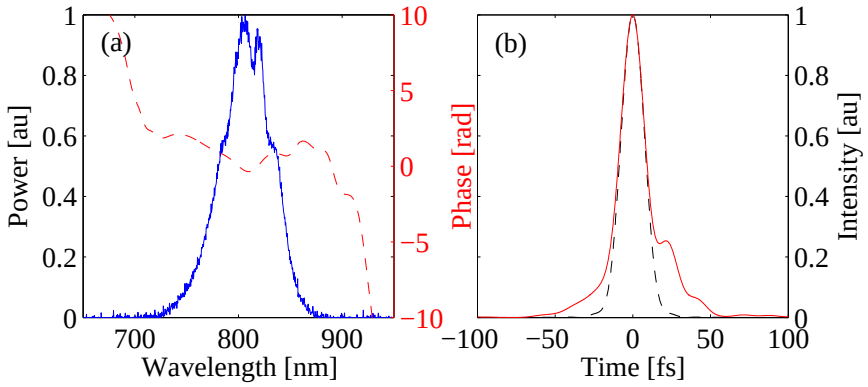

Figure 3.4: Ar, 470mbar, linear polarization: (a) Spectral power (blue, solid) and phase (red, dashed), and (b) Measured intensity (red, solid) and transform limit (black, dashed).

Fig. 3.4 shows the SPIDER reconstruction of a pulse after filamentary propagation of 850μJ, 41.8fs, linearly polarized pulses through Ar at 470mbar. 200fs^2 of GDD was added to the beam path after re-collimation to achieve the flattest possible spectral

phase profile. SPM in Ar increased the spectral width by $\sim$ 25%, decreasing the pulse duration from 41.8fs to 18.8fs while reducing the pulse energy from 850μJ to 650μJ. Using the simple estimation for peak power $P = U/\tau$, the power increased from 20.3GW before filamentary propagation to 34.6GW.

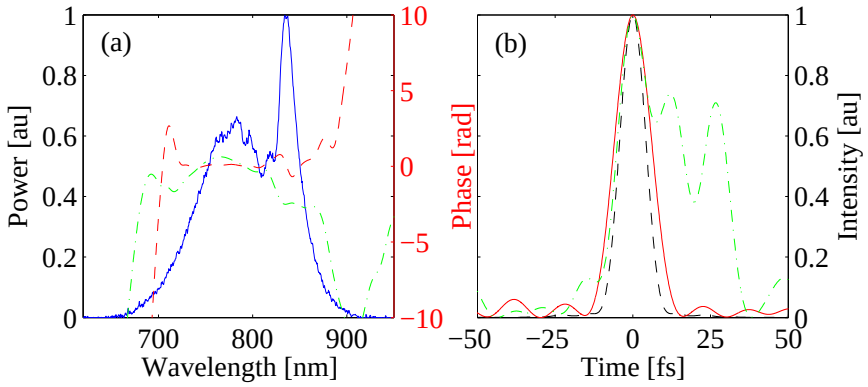

Figure 3.5: Ar, 870mbar, linear polarization: (a) Spectral power (blue, solid), phase with no dispersion compensation (green, dash-dot), and phase with +200fs^2 added (red, dashed), and (b) Measured intensity with no dispersion compensation (green, dash-dot), intensity with +200fs^2 added (red, solid), and transform limit (black, dashed).

Increasing the Ar pressure to 870mbar with no other changes to the setup, the bandwidth was observed to increase to 90nm while the pulse duration decreased to 13.5fs with the same energy throughput as the 470mbar case. The peak power for these pulses is calculated to be 48.1GW. Fig. 3.5 shows the SPIDER reconstructed pulse for these experimental conditions. Also shown is the SPIDER reconstruction of the pulse in the absence of post-filament dispersion compensation. The negative net GDD imparted by propagation through the filament is clearly visible.

After re-inserting the dispersion compensation, a $\lambda/4$ waveplate was placed in the beam immediately prior to focusing into the gas tube. All other parameters were held constant, and the observed filament again showed two nonlinear focusing cycles. Fig. 3.6 shows the reconstructed pulse after filamentary propagation of a circularly polarized pulse through an 870mbar Ar environment. For this case, the bandwidth

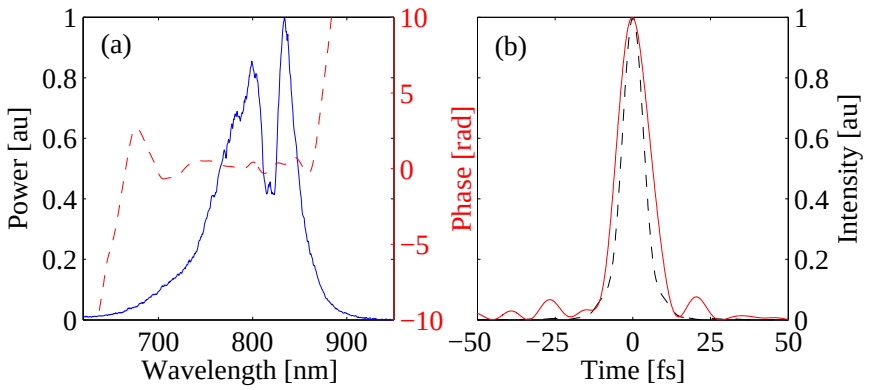

Figure 3.6: Ar, 870mbar, circular polarization: (a) Spectral power (blue, solid) and phase (red, dashed), and (b) Measured intensity (red, solid) and transform limit (black, dashed).

increased to 91.1nm and the pulse duration decreased to 12.2fs. The overall energy throughput remained constant at $\sim 76.5\%$. The differences in spectral content and phase between the linear and circularly polarized cases are attributed to the change in physical response of the Ar to the two polarization states. For linear polarization, n_2 should be four times greater than for circular polarization [87], however this model has recently been proved incorrect [88], and the actual value for n_2 for circular polarization is much closer to that of linear polarization [89]. Furthermore, the constant modulus of the electric field in the circularly polarized case leads to a higher ionization rate, a greater electron plasma density, and therefore a larger plasma defocusing effect.

Combined, the lower n_2 and larger ionization rate for circularly polarized light significantly alter the net SPM and self-compression effects from filamentary propagation; it is somewhat surprising, then, that such similarity exists in the compressed pulses between the linear and circularly polarized cases. One major difference does exist, however: the divergence rate of the circularly polarized beam was observed to be twice the divergence of the linearly polarized case. This is not unexpected, since the lower n_2 for circular polarization means that the laser must have higher intensity

in order maintain a balance between self-focusing, diffraction, and plasma defocusing to achieve filamentary propagation. Higher intensity necessitates a smaller beam diameter within the filament, and therefore a larger divergence angle upon exiting the filament.

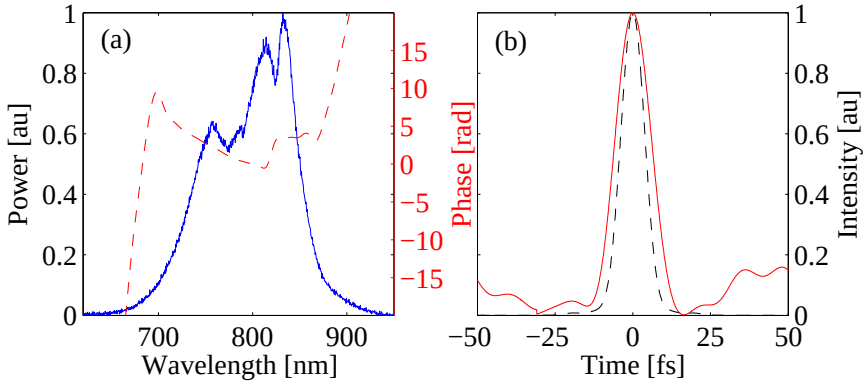

Figure 3.7: Ar, 1000mbar, linear polarization: (a) Spectral power (blue, solid) and phase (red, dashed), and (b) Measured intensity (red, solid) and transform limit (black, dashed).

A final test was made in Ar at 1000mbar using linearly polarized light; SPIDER results are shown in Fig. 3.7. Although the 91nm bandwidth was the largest observed in Ar for the linearly polarized cases, the pulse compression was only minimally improved. In large part, the small improvement in pulse compression is most likely due to instrumentation limitations. The BBO crystal used in the SPIDER was 50μm thick. Simulations with the widely used SNLO nonlinear optics package [84] indicate that a type-II 50μm-thick BBO crystal cut for 800nm has a phase-matching bandwidth of 108.3nm. However, this value corresponds to $-\pi \leq \Delta kL \leq \pi$, and therefore the bandwidth over which efficient sum-frequency generation is expected is somewhat less than this value. Examination of Figs. 3.4 - 3.7 shows that, indeed, the spectral phase profile retrieved by the SPIDER does not cover the entire range spanned by the measured spectral power. The phase becomes ill-defined where significant spectral power still exists–this is a direct consequence of the BBO crystal's

inability to phase-match the entire pulse spectrum. Visible evidence of this behavior was evident when running the SPIDER: tilting the BBO crystal to alter the phase matching angle shifted the pattern of spectral fringes from blue to red (depending on which way the crystal was moved), showing that even before attempting phase reconstruction the spectral range covered by the SPIDER signal was insufficient to provide meaningful phase information over the entire spectrum. As such, the SPIDER measurements may be inaccurate and the observed self-compressed pulses may be much closer to transform-limited than is indicated.

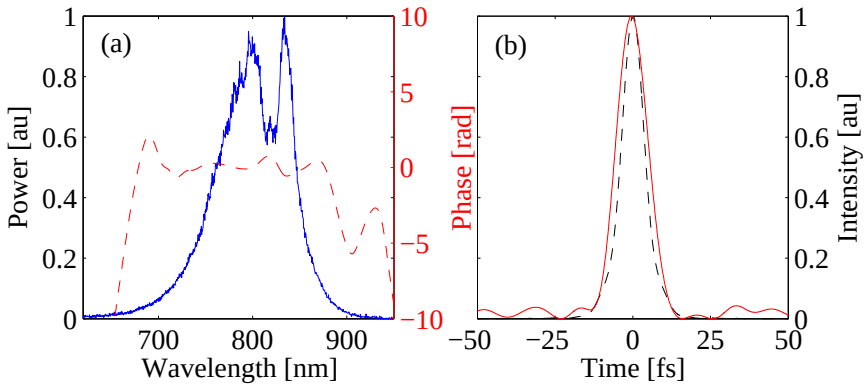

Figure 3.8: Kr, 440mbar, linear polarization: (a) Spectral power (blue, solid) and phase (red, dashed), and (b) Measured intensity (red, solid) and transform limit (black, dashed).

As a check that the observed self-compression behavior was not specific to Ar, other gases were used in an attempt to see if similar behavior could be observed. Fig. 3.8 shows the reconstruction of linearly polarized pulses after undergoing filamentary propagation in a 440mbar Kr atmosphere. Since the nonlinear susceptibility of Kr is larger than Ar (see Table 3.1), the critical power for self-focusing given by Eq. 1.2 is reduced. Consequently, to maintain the proper balance between self-focusing and plasma defocusing it was necessary to reduce the input pulse power. This was accomplished by decreasing the diameter of the hard aperture, clipping the beam prior to focusing into the gas tube. For the Kr trial, the hard aperture

diameter that led to the best observed self-compression was 5.5mm, and the resulting input pulse energy was 650μJ. The output pulse energy was 500μJ, for an overall energy throughput of $> 76\%$, quite similar to the Ar trials. 440mbar Kr produced a spectral width of 85nm, and the measured pulse duration was the shortest of all test cases: 11.9fs. For these experimental conditions, the peak power increased from 15.6GW to 42GW.

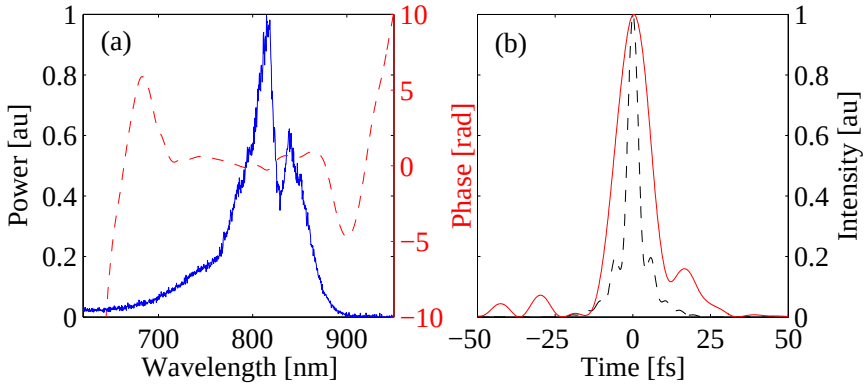

Figure 3.9: Xe, 638mbar, linear polarization: (a) Spectral power (blue, solid) and phase (red, dashed), and (b) Measured intensity (red, solid) and transform limit (black, dashed).

The final noble gas used was Xe, with the highest n_2 of all gases used. To compensate for the resulting decrease in critical power, the input beam was strongly attenuated using a 3.5mm diameter hard aperture. The input pulse energy was then 300μJ, and the output energy was 200μJ. The strong SPM induced in the highly susceptible Xe medium produced the broadest recorded spectrum, 152.7nm, which supports a transform limited pulse duration of 4.1fs. The inability of the BBO crystal in the SPIDER to phase match the entire spectrum, however, led to a reconstructed pulse duration similar to the Ar and Xe cases: 12.8fs. In all three noble gases, the fundamentals of the observed behavior were the same: two nonlinear focusing cycles were observed, and the output pulses were negatively chirped.

Aside from noble gases, self-compression was also observed in N_2. In this case,

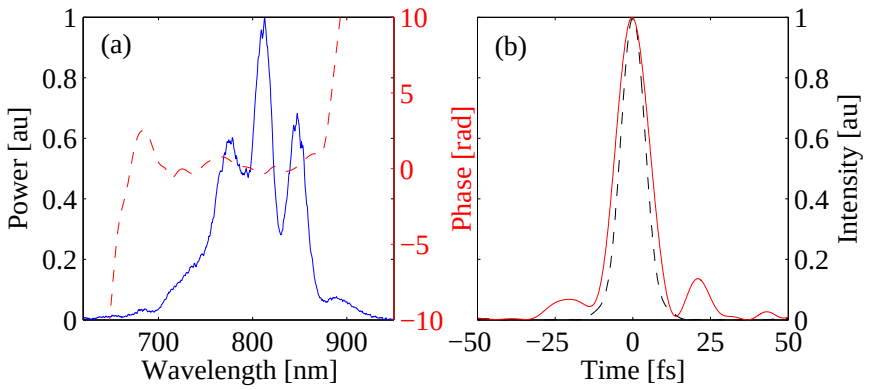

Figure 3.10: N_2, 1285mbar, linear polarization: (a) Spectral power (blue, solid) and phase (red, dashed), and (b) Measured intensity (red, solid) and transform limit (black, dashed).

however, the SPM-broadened spectrum shows significantly more structure than for Ar, Kr, or Xe, as can be seen in Fig. 3.10. Unlike the filaments in noble gases, the filament in N_2 had 5 observable nonlinear focusing cycles, with a total filament structure length of $\sim$ 70cm. Theoretical modeling for filamentary propagation in air [90] reveals that a delayed Kerr response in molecular nitrogen significantly alters the dynamical balance of the filament by transferring the induced nonlinear index from the front part of the pulse to trailing parts, leading to a balance between self-focusing and plasma defocusing at the rear of the pulse and creating stable filaments over much longer distances. Also, although the input energy was high, 1.25mJ, the throughput was much lower than in noble gases, and the extracted pulse energy was

Gas	Ar	Ar	Ar	Ar	Ar	Kr	Xe	N_2
n_2 (10^{-19}cm^2/W)	0.74	1.37	1.37	0.91	1.58	1.60	6.43	1.58
Pressure (mbar)	470	870	870	870	1000	440	638	1285
Polarization	lin	lin	lin	circ	lin	lin	lin	lin
Hard Aperture Dia. (mm)	7	7	7	7	7	5.5	3.5	10
Added GDD (fs^2)	200	0	200	200	200	200	260	200
Measured τ (fs)	18.78	35.90	13.52	12.22	13.29	11.88	12.77	12.40
Transform Limit τ (fs)	17.57	9.61	9.61	8.11	9.00	8.53	4.14	9.19
λ_0 (nm)	799.06	778.27	778.27	766.75	775.93	770.44	717.36	783.04
$\Delta\lambda$ (nm)	49.58	89.97	89.97	92.94	91.06	84.99	152.71	86.35
Input Energy μJ	850	850	850	783	850	650	300	1250
Output Energy μJ	650	650	650	598	650	500	200	500
P_{in}/P_{crit}	1.56	2.89	2.89	1.77	3.32	2.58	4.78	4.90

Table 3.1: Summary of results for self-compression at 800nm. P_{crit} calculated using Eq. 1.2 with $\alpha = 1.8962$.

only 500μJ.

For all gases and gas pressures used, it was found that the ratio of input power to critical power for self-focusing $P_{in}/P_{crit} > 1.5$ is a requirement for the observation of stable filamentary propagation resulting in net negative GDD.

3.2 Self-compression at 2μm

The experimental setup for generating compressed pulses via filamentary propagation at 2μm was quite similar to the 800nm setup shown in Fig. 3.1. No telescope was used to down-collimate the input beam, however, and no added GDD was used following re-collimation after filamentation. The spherical mirror focusing the beam into the gas tube had a focal length $f = 0.5$m, and the gas tube was 1m long, filled with a Xe atmosphere. Fig. 3.11 shows the observed plasma fluorescence using a Xe pressure of 2.15bar. Similar to the observed 800nm self-compressed pulses, two nonlinear focusing cycles were observed.

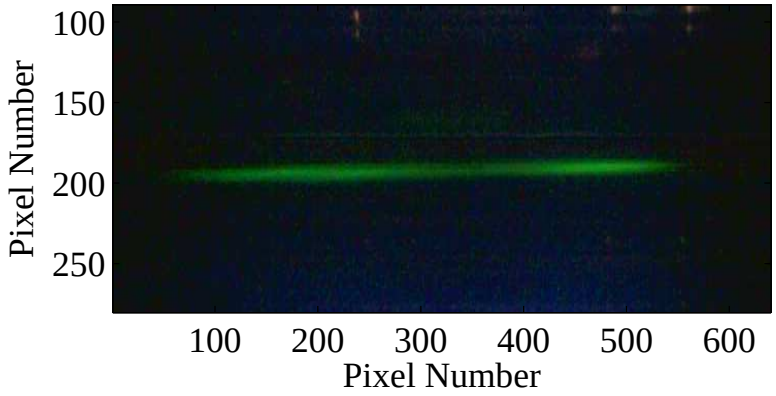

Figure 3.11: Sequential filament structure in Xe at 2.15bar as observed from plasma fluorescence. The total length of the observed fluorescence was $\sim$ 10cm.

The 2μm source for this experiment was a train of $\lambda_0 = 1.96\mu$m, 500μJ, $\sim$ 65fs pulses produced at a 1kHz repetition rate from a modified Ti:sapphire pumped traveling-wave optical parametric amplifier (OPA). Fig. 3.12 shows the measured

OPA spectrum. Clipping the spectrum was unavoidable; the grating in the spectrometer (147/mm groove density) was too dispersive to allow the entire spectrum to fit on a single readout from the InGaAs array detector. Nonetheless, the vast majority of the spectral power is represented in Fig. 3.12, therefore the computed transform limited intensity profile will not change greatly if the missing spectral components are included. The OPA is pumped with 4mJ, 65fs, $\lambda_0 = 810$nm pulses.

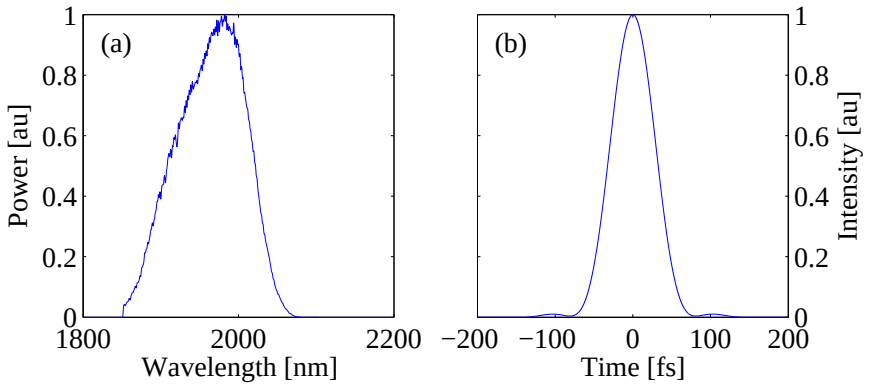

Figure 3.12: 2μm OPA output. (a) measured spectrum: $\lambda_0 = 1957.2$nm, $\Delta\lambda = 101.3$nm. (b) transform limited intensity profile: $\tau = 65.2$fs.

A small portion of the 800nm pump is used to generate a superflourescence spectrum in a BBO crystal, from which the 1.3μm signal beam is extracted. This first BBO crystal also amplifies the 1.3μm prior to the power amplifier, a 2mm-long BBO crystal used in a non-collinear geometry to provide difference-frequency generation (DFG) between the bulk of the 800nm pump and the 1.3μm signal, amplifying the 2μm idler to $\sim 500\mu$J. Since the signal is coherently generated from the pump, the DFG-generated idler maintains a constant carrier-envelope phase (CEP) offset [91, 92, 93, 94, 95, 96, 97], even though the 800nm pump is not CEP-stabilized. Access to few-cycle, CEP-stabilized sources is highly desirable for the generation of isolated attosecond pulses and pulse trains [98]; the production of CEP-stabilized pulses without external measurement and feedback is a significant advantage for

DFG OPA designs.

3.2.1 Experimental Results

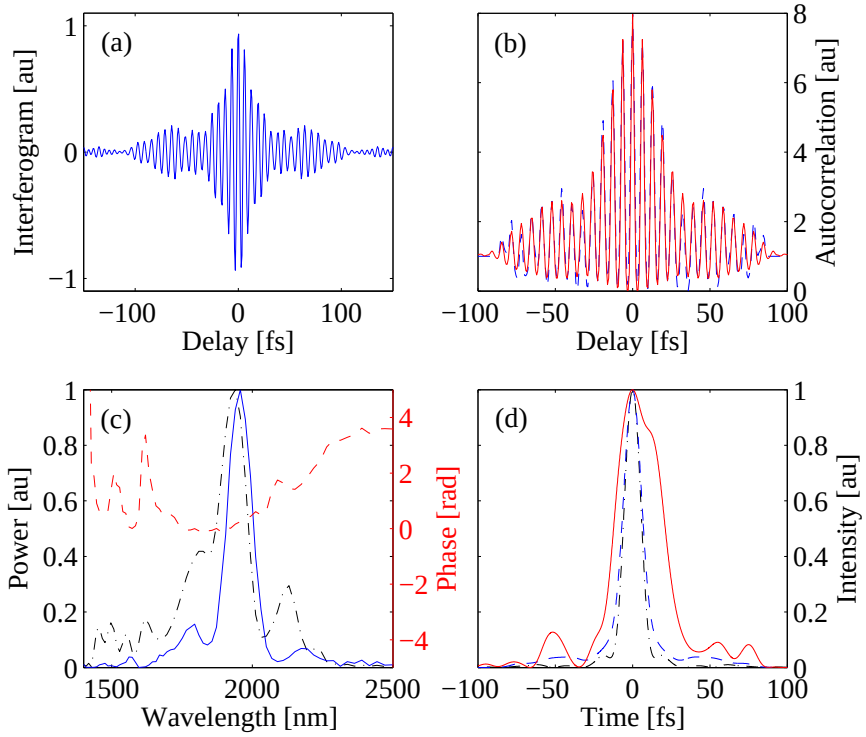

Figure 3.13: 1.6 bars Xe. (a) Filtered interferogram. (b) Filtered 2$^{\text{nd}}$-order autocorrelation (blue, dashed), and retrieved (red, solid). $\Delta = 0.1132$. (c) Spectral power and phase: measured power (black, dash-dot), best fit power (blue, solid), and best fit phase (red, dashed). (d) Intensity profiles: transform limit with measured power spectrum (black, dash-dot), transform limit with best-fit power spectrum (blue, dashed), and recovered (red, solid).

Unfortunately, a more sophisticated pulse measurement system such as a SPIDER [25] or FROG [24] was not available during this experiment. Instead, the filament-compressed pulses were sent into a Michelson interferometer and interferometric autocorrelation (IAC) data was collected. The interferometer used a 2μm-thick pellicle broadband-coated for 50/50 beam splitting at 2μm. The end mirror in one of the two arms of the interferometer was actuated by a closed-loop piezo-electric stack with 30μm total displacement, resulting in a total scan range of $\pm$100fs. Four

separate Xe pressures were tried: 1.6bar, 1.87bar, 2.15bar, and 2.44bar. The output pulse energy at all four pressures was roughly constant at $\sim 270\mu$J. At each pressure, a linear autocorrelation was collected using an InGaAs photodiode, and after filtering for noise the power spectrum $|E(\omega)|^2$ was computed from the Fourier transform of the unit-normalized 1$^{\text{st}}$-order autocorrelation $S_1(\tau)$ as

$$|E(\omega)|^2 = \mathfrak{F}(S_1(\tau) - 1) \tag{3.3}$$

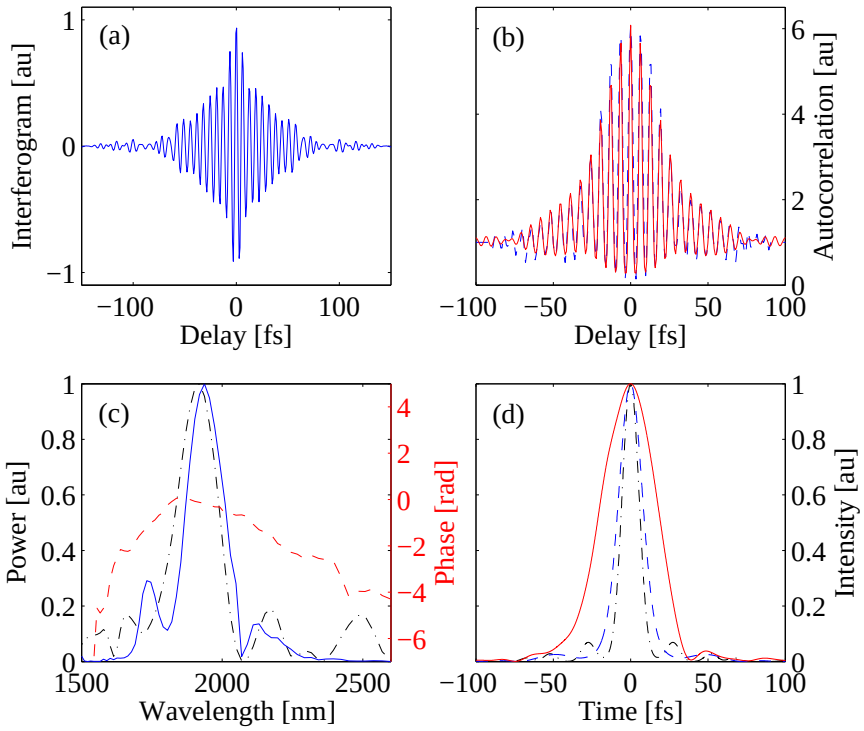

Figure 3.14: 1.87 bars Xe. (a) Filtered interferogram. (b) Filtered 2$^{\text{nd}}$-order autocorrelation (blue, dashed), and retrieved (red, solid). $\Delta = 0.1158$. (c) Spectral power and phase: measured power (black, dash-dot), best fit power (blue, solid), and best fit phase (red, dashed). (d) Intensity profiles: transform limit with measured power spectrum (black, dash-dot), transform limit with best-fit power spectrum (blue, dashed), and recovered (red, solid).

Due to the extremely broadband light emerging from the filament, it was impossible to collect a power spectrum using the existing 2μm spectrometer; the installed grating was simply too dispersive. While the use of a linear interferogram to derive the spectral power is more prone to noise, it was found to be much simpler

than capturing multiple spectra on the spectrometer at different grating angles and attempting to concatenate them into a single spectrum.

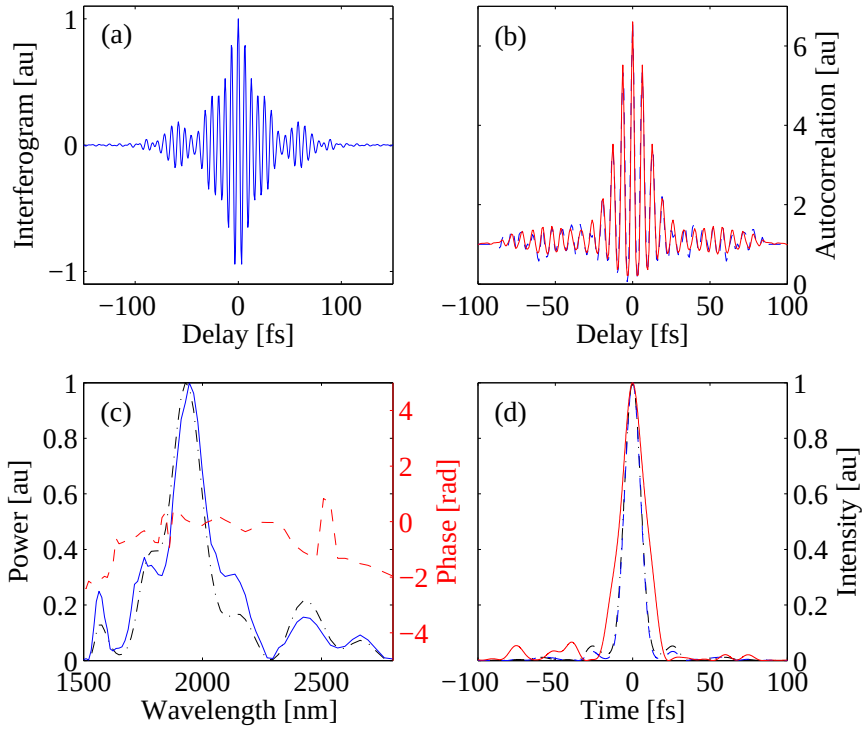

Figure 3.15: 2.15 bars Xe. (a) Filtered interferogram. (b) Filtered 2nd-order autocorrelation (blue, dashed), and retrieved (red, solid). $\Delta = 0.0619$. (c) Spectral power and phase: measured power (black, dash-dot), best fit power (blue, solid), and best fit phase (red, dashed). (d) Intensity profiles: transform limit with measured power spectrum (black, dash-dot), transform limit with best-fit power spectrum (blue, dashed), and recovered (red, solid).

A 2nd-order IAC was also collected at each pressure using a two-photon induced photocurrent from a saturated InGaAs photodiode. The measured power spectrum and 2nd-order IAC were then used to retrieve the spectral phase using a modified whole-beam version of the adaptive genetic algorithm designed to process data from the split mirror autocorrelator described in chapter II of this thesis. Since the OPA output pulse energy contains unavoidable fluctuations ($\sim 5\%$ RMS), it is to be expected that these energy fluctuations will be reflected in the spectra of the SPM-broadened pulses emerging from the filament. These fast timescale fluctuations in the

power spectra are then a direct source of noise in the linear and nonlinear IAC traces. Unfortunately, this noise cannot be removed via simple Fourier filtering techniques. Understanding that the power spectrum retrieved may be significantly distorted due to the shot-to-shot fluctuations in power spectra present over the time necessary to collect the linear trace, the spectrum derived using Eq. 3.3 must be viewed as something less than perfectly accurate. In order to obtain a better fit between the measured and retrieved 2^{nd}-order IAC traces, the spectral power was parameterized in addition to the spectral phase. While the search space for the spectral phase was unbounded, the genetic algorithm searched for the best spectral power using a more reserved approach, limiting the possible values allowed for any spectral power gene to $+80\%$ of the maximum value and -80% of the minimum value of the interferogram-derived spectral power within a window $\pm$50nm around the wavelength at which a given gene represents the power.

Figs. 3.13 - 3.16 show the results for the four Xe pressures tried, in order from 1.6bar to 2.44bar. Table 3.2 summarizes the results for the four Xe trials. Due to the high level of noise present when collecting the data, none of the acquired 2^{nd}-order IAC traces show the theoretical 8:1 fringe contrast ratio. Since the analytic formula for the 2^{nd}-order IAC $S_2(\tau)$ [22] always produces an IAC with 8:1 contrast, a scaling parameter was added to the retrieval algorithm to match the peak values of the measured and retrieved traces. The RMS figure of merit Δ for a retrieved 2^{nd}-order IAC should be less than 0.003 for the most accurate retrieval from low-noise data. Clearly, none of the retrieved IACs approached this target, and therefore the results should be viewed only as good estimates for the pulses emerging from the filament. The estimated pulse durations are reasonable, however, given the observed temporal width of the 2^{nd}-order autocorrelation traces. It is interesting to note

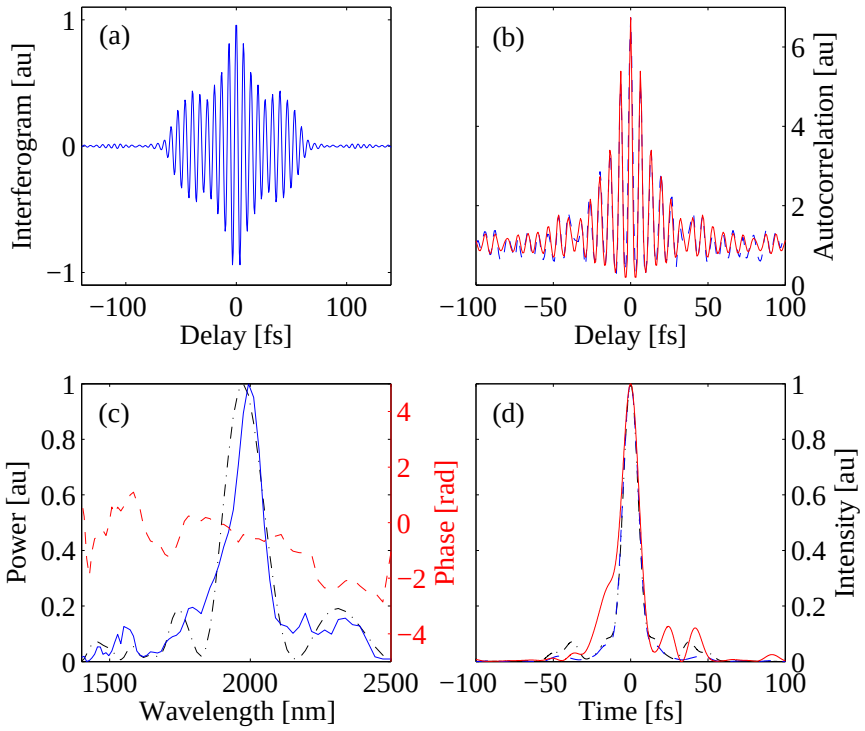

Figure 3.16: 2.44 bars Xe. (a) Filtered interferogram. (b) Filtered 2$^{\text{nd}}$-order autocorrelation (blue, dashed), and retrieved (red, solid). $\Delta = 0.0780$. (c) Spectral power and phase: measured power (black, dash-dot), best fit power (blue, solid), and best fit phase (red, dashed). (d) Intensity profiles: transform limit with measured power spectrum (black, dash-dot), transform limit with best-fit power spectrum (blue, dashed), and recovered (red, solid).

that the net negative GDD calculated for 2μm light through the 1.5mm-thick CaF_2 output window on the gas tube almost exactly cancels the calculated positive GDD incurred through the 2m air propagation to the detector in the Michelson. Thus, the reconstructions presented represent reconstructions at the interior face of the gas tube output window, and indicate that for the 2.15bar and 2.44bar cases the pulses were self-compressed to nearly the transform limit at the exit of the filament. Since the autocorrelator used was a balanced 2$^{\text{nd}}$-order autocorrelator, the problem of time-reversal symmetry exists in the retrieved results, and the sign of the retrieved spectral phase is ambiguous. It is therefore impossible to determine if the multiple nonlinear focusing cycles observed during filamentary propagation produced a net

negative GDD, as was the case for the 800nm self-compressed pulses.

Pressure (bar)	1.6	1.87	2.15	2.44
Δ (IAC fitting F.O.M.)	0.1132	0.1158	0.0619	0.0780
Measured τ (fs)	33.14	41.19	17.91	13.65
Transform Limit τ (fs) (measured spectrum)	12.28	12.88	12.52	11.42
Transform Limit τ (fs) (best-fit spectrum)	14.32	18.23	12.18	11.79
λ_0 (nm) (measured spectrum)	1800	1883	1928	1879
$\Delta\lambda$ (nm) (measured spectrum)	457	480	528	541
λ_0 (nm) (best-fit spectrum)	1880	1912	1936	1874
$\Delta\lambda$ (nm) (best-fit spectrum)	438	357	533	520

Table 3.2: Summary of results for self-compression at 2μm.

After performing the pressure scan and acquiring autocorrelator data, the pressure was fixed at 2.15bar and the self-compressed pulses were sent into an f-to-2f interferometer [99]. The white light spectrum emerging from the filament was sufficiently broad that is was not necessary to use additional frequency generation techniques to obtain the required octave-spanning spectrum. A 500μm-thick BBO crystal was used to frequency double the central portion of the pulse spectrum, which then produced a spectral interferogram with the blue tail of the white light background at $\lambda \sim 900$nm.

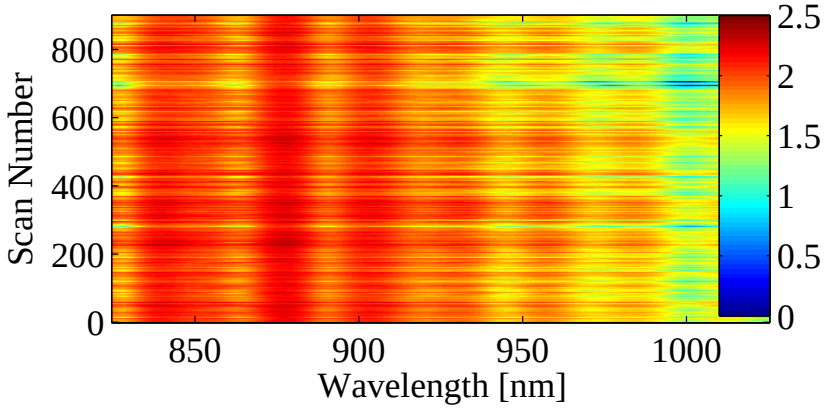

Figure 3.17: f-to-2f interferogram time series acquired for over 8,800 laser shots. Each scan represents the integration of 10 laser shots.

Fig. 3.17 shows a time series of the measured f-to-2f interferogram spanning a range of nearly 9 seconds. From this data, the residual CEP drift was measured to

be $<$ 0.1rad (RMS). Fig. 3.18 shows the f-to-2f interferogram integrated over 120 seconds. The excellent fringe contrast is a clear indicator of long-term CEP stability. Similar measurements were made using the 1.3μm signal beam instead of the 2μm idler, and the CEP offset was observed to be random. This observation, combined with the short and long-timescale f-to-2f measurements for the SPM-broadened 2μm pulses leads to the conclusion that the CEP offset is preserved through filamentary propagation, but the filament itself does not stabilize the CEP offset.

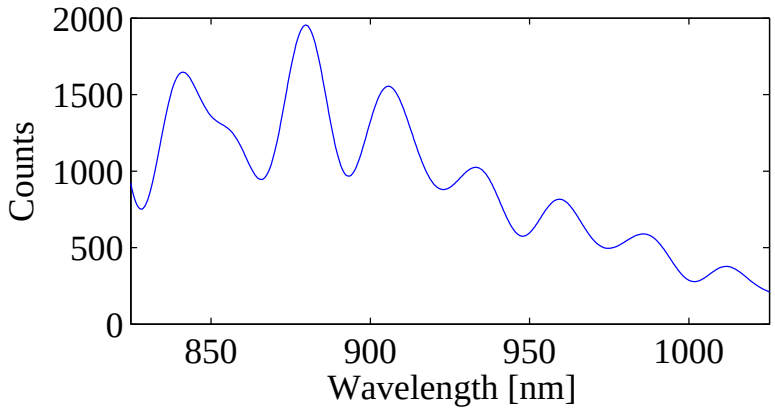

Figure 3.18: Integration of the f-to-2f interferogram over 120s.

CHAPTER IV

Temporal Characterization of Scaled System Harmonics using Cross-Correlation Frequency Resolved Optical Gating

This chapter describes a cross-correlation frequency-resolved optical gating (XFROG) experiment designed to temporally characterize harmonic orders 5 - 15 from a 3.6μm laser focused on a Cs target. In addition to characterizing each individual harmonic order's power and phase, previously reported using an XFROG geometry in the XUV [100], this experiment is also sensitive to the relative delay between harmonic orders, giving us some degree of access to the attochirp for the 3.6μm/Cs scaled system. The intensity-dependent phase is inaccessible, since the FROG design uses an intensity gating scheme and is thus only sensitive to the pulse-averaged spectral phase of a given harmonic order. This XFROG measures the combined effects of the attochirp and intensity-dependent phase, averaged over the total number of cycles in the harmonic pulse. All harmonic orders considered lay in a spectral region where solid-state nonlinearities exist and are efficient, greatly simplifying the complexity of the setup required to make the desired measurement.

4.1 XFROG Design

Fig. 4.1 shows a generic FROG layout. The gate beam is delayed using a motorized delay line and mixed with the probe beam in a chosen nonlinear medium. The result,

a cross-correlation between the gate and probe, is spectrally resolved. Spectra are collected over a range of delays τ to build the FROG spectrogram $I_{\mathrm{FROG}}(\omega, \tau)$. For the most common FROG geometries, the gate and probe are copies of the same pulse; therefore the analytic expression for the spectrogram most often resembles a frequency-resolved autocorrelation.

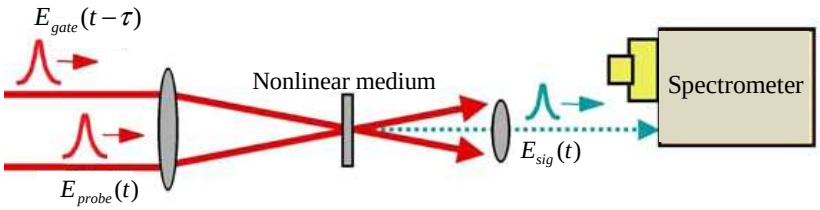

Figure 4.1: Generic FROG setup.

Using a solid-state nonlinearity in a FROG setup opens many avenues for the experimental geometry and type of gate/pulse mixing used. The most fundamental limitation faced by this experiment is the transmissivity of materials in both the harmonics beam path (probe) and the FROG beam path (signal). The range of wavelengths to be accommodated by the FROG apparatus spans from the near-IR through the UV, as can be seen in Table 4.1 and Fig 4.2.

Harmonic Order	1	3	5	7	9	11	13	15	17	19
Wavelength (μm)	3.6	1.2	0.72	0.514	0.4	0.327	0.277	0.24	0.212	0.19
Frequency (rad/fs)	0.523	1.57	2.616	3.663	4.709	5.756	6.802	7.848	8.895	9.942
Energy (eV)	0.344	1.033	1.722	2.411	3.1	3.788	4.477	5.166	5.855	6.544

Table 4.1: Wavelengths, frequencies, and energies for the low-order harmonics generated with a 3.6μm driver.

Characterizing such a broad spectral range with traditional broadband FROG geometries is untenable for many reasons. Self-diffraction FROG (SD-FROG) [101, 102] is a non-phase-matched process; hence, the material thickness must be very thin $\lesssim 200\mu$m to minimize phase mis-match, and the resulting signal level is weak. Polarization-gate FROG (PG-FROG) [103, 104, 105, 106, 107, 108], a popular and

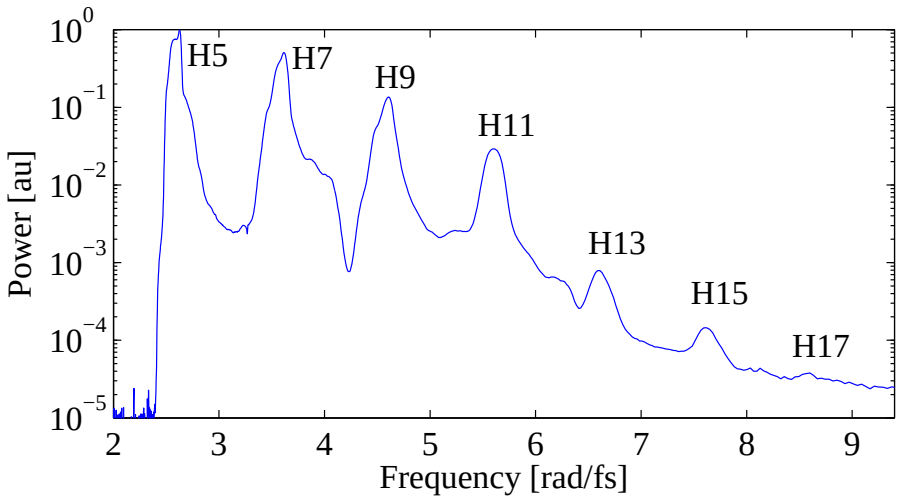

Figure 4.2: Power spectrum for harmonics from Cs with a 3.6μm driver: P $\sim$ 60 Torr, pulse energy = 85μJ, $\tau \sim$ 120fs.

versatile scheme, requires the use of a polarizer and waveplate prior to mixing the pulse and gate beams, which adds an unacceptable amount of dispersion. Transient-grating FROG (TG-FROG) [109, 110] is a three beam geometry and thus too complex for consideration. SD-FROG, PG-FROG, TG-FROG, and third harmonic generation FROG (THG-FROG) [111] are all $\chi^{(3)}$ processes, and therefore require $\sim$ nJ pulse energies to produce a useful signal beam. Unfortunately, the energies in the mid-IR driven harmonics from the Cs heat pipe, shown in Table 4.2, are much too low to make use of any $\chi^{(3)}$-based FROG. In contrast, second harmonic generation FROG (SHG-

Harmonic Order	Energy per Pulse (pJ)
5	187
7	133
9	28.7
11	12.4

Table 4.2: Calibrated energy measurement for harmonic orders 5 - 11.

FROG) [24] uses a $\chi^{(2)}$ nonlinearity, and is thus capable of efficiently producing a FROG signal beam with pulse energies as weak as 1pJ. However, SHG-FROG, along with all the aforementioned $\chi^{(3)}$-based FROG geometries, all require the use of at least one beam splitter to create a pulse replica. The ultra-broadband nature of the

harmonics emitted from the Cs source makes the selection of a single beam splitter that can provide a 50/50 splitting ratio over the entire spectrum impossible. Different beam splitters might be chosen for use with each harmonic order, however this would require replacing an optic and re-aligning the spatial and temporal overlap each time we wish to collect a FROG scan for a different order harmonic. Additionally, $\chi^{(2)}$-based SHG-FROG is limited to fundamental wavelengths longer than 410nm, since the best available $\chi^{(2)}$ material for UV applications, beta-BaB_2O_4 (β-BBO) will not phase match the SHG process for shorter wavelengths. Also, BBO does not transmit wavelengths shorter than 190nm due to oxygen absorption. Thus, an SHG-FROG setup would only be capable of producing results for harmonic orders 3, 5, and 7.

Given the limitations of the traditional FROG geometries, which measure an unknown pulse by gating it with a copy of itself, a more exotic design is required. Cross-correlation FROG (XFROG) [112, 113], where the unknown pulse is mixed with a separate (ideally well-characterized) reference pulse, is therefore an attractive alternative. An XFROG setup generally takes two forms, sum-frequency generation XFROG (SFG XFROG) or difference-frequency generation XFROG (DFG XFROG), both of which are $\chi^{(2)}$-based designs. In either form, the only requirement on the FROG design is that the chosen nonlinear medium be capable of phase-matching the desired SFG or DFG process. No limitation other than this is placed on the pulse duration, frequency content, or center frequency of the two pulses. For an SFG XFROG, the measured spectrogram is given by

$$\mathbf{I}^{\mathrm{SFG}}_{\mathrm{XFROG}}(\omega,\tau) = \left| \int_{-\infty}^{\infty} \mathbf{E}_{\mathrm{probe}}(t)\mathbf{E}_{\mathrm{gate}}(t-\tau)e^{-i\omega t}dt \right|^2 \tag{4.1}$$

A DFG XFROG spectrogram takes the form

$$\mathbf{I}^{\mathrm{DFG}}_{\mathrm{XFROG}}(\omega,\tau) = \left| \int_{-\infty}^{\infty} \mathbf{E}_{\mathrm{probe}}(t)\mathbf{E}^{*}_{\mathrm{gate}}(t-\tau)e^{-i\omega t}dt \right|^2 \tag{4.2}$$

For the mid-IR harmonics FROG, adopting an XFROG geometry offers several key advantages over other more widely used FROG variants. In the XFROG geometry it is not necessary to split the harmonics beam into two equal replicas; the full energy from each harmonic order is available for use when mixing against the gate beam. Also, using a long-wavelength gate allows us to phase match many more harmonic orders than is possible with an SHG-FROG. With a long-wavelength gate the resulting XFROG signal beam is very close in wavelength to the harmonic order being mixed, thus enabling us to obtain FROG traces for harmonic orders that lie quite close to the VUV cutoff. Finally, the XFROG signal strength scales with the amplitude of the gate field, allowing us to measure extremely weak probe beams by simply providing a very strong gate.

Since SFG processes are generally far stronger than DFG processes in the absence of seeding the difference frequency, the selected XFROG variant for characterizing the 3.6μm harmonics is an SFG XFROG using BBO as the nonlinear medium. Since we desire passive synchronization between the gate and probe beams in order to obtain attosecond timescale measurement precision, the gate must be generated from the same 3.6μm pulse that is used to generate the harmonics. BBO will not phase match wavelengths longer than 3.5μm, thus it is not possible to use a small piece of the original 3.6μm pulse as a gate. Instead, we frequency double a small portion of the 3.6μm pulse using a 1mm-thick piece of $AgGaSe_2$ (AGSE) cut for type-I SHG at 3.6μm. The resulting 1.8μm pulse is then used as a gate pulse in the XFROG. Simulations with the widely used nonlinear optics package SNLO [84] predict that SFG phase matching between 1.8μm and the harmonics is possible for harmonics 3 through 17. However, the H2 + H17 process produces H19, which lies right at the VUV cutoff. Since two thick α-BBO polarizers are used to isolate the FROG signal

from the harmonics beam, and since the FROG signal beam undergoes significant propagation in air, it is highly unlikely that the SFG signal from the H2 + H17 mixing process will reach the spectrometer due to oxygen absorption. Also, although it is quite easy to mix H2 + H3, a spectrometer capable of measuring the spectral power of H3 (1.2μm) directly was not available at the time this experiment was run. Thus, the third harmonic is excluded from examination in this experiment.

4.1.1 β-BBO crystal selection

For broadband SFG in β-BBO, type-II (e,o,e) phase matching (where the harmonics beam is the o-ray) is preferred due to the larger acceptance bandwidth afforded to the o-ray. Conveniently, the 1.8μm beam is naturally cross-polarized with the harmonics, since the 1.8μm is generated using a type-I (o,o,e) SHG process in the AGSE crystal, and the harmonics are co-polarized with the 3.6μm beam. However, even with type-II phase matching SNLO calculations reveal that it is not possible to select a reasonable thickness for the BBO crystal and phase match all harmonic orders with the H2 gate. Consequently, it is not possible to collect a single FROG trace where all harmonic orders are phase matched. Multiple BBO crystals must be employed, with each crystal optimized for thickness and phase-matching angle to phase match a narrower range of wavelengths.

In order to obtain useful information about the relative delay between harmonic orders, it is necessary to obtain phase matching between the H2 gate and at least two harmonic orders with a single crystal. This way, a single scan can obtain, for example, the H2+H5 and H2+H7 SFG XFROG traces. The relative delay between these two orders is then embedded directly into the scan, and we are not forced to calculate the delay between orders using the reported delay line stage position.

Instead, the FROG retrieval algorithm naturally produces the two harmonics pulses delayed by the proper amount without any external calculation.

Detailed simulations were performed using SNLO and Matlab to find values for θ and appropriate crystal thicknesses to allow H2 + H5/7, H2 + H7/9, etc. For these simulations, θ was varied through a range of values separated by 0.1°. At each value for θ, the refractive index, group index, group velocity dispersion, and walkoff angle was computed for H2, both harmonics orders under consideration, and both SFG results expected. To design a crystal to mix a desired pair of harmonic orders i, j with the H2 gate, the optimum angle θ was found by attempting to minimize the function

$$f(\theta) = \Big| \big|\Delta k_i(\theta)\big| - \big|\Delta k_j(\theta)\big| \Big| \tag{4.3}$$

where $\Delta k(\theta)$ is the wave vector mismatch for a given SFG interaction between H2 and harmonic order q, defined as

$$\Delta k_q = 2\pi \left(\frac{n_{SFG}}{\lambda_{SFG}} - \frac{n_{1.8\mu m}}{1.8\mu m} - \frac{n_q}{\lambda_q} \right) \tag{4.4}$$

where the subscript SFG denotes the sum-frequency values for n and λ. Minimizing $f(\theta)$ in Eq. 4.3 effectively maximizes the phase matching length L within the BBO for both harmonic orders i, j under the constraint that the crystal should be no thicker than the smaller of the two phase matching lengths L_i, L_j. Since we desire the highest possible SFG conversion efficiency for both harmonic orders, a crystal thicker than the smaller of the two phase matching lengths could potentially couple energy from the SFG signal beam back into the harmonics beam. After minimizing $f(\theta)$, the crystal thickness z was chosen as

$$z = \min\big(L_i, L_j\big) \tag{4.5}$$

where the phase matching length is computed as

$$L \leq \frac{\pi}{\Delta k} \tag{4.6}$$

After finding the maximal value for z for a particular pair of harmonics, z was rounded down to the nearest easily manufacturable integer value. In all cases the maximum crystal length was found to be $z \leq 52\mu m$, thus walk-off effects can be neglected, since the crystal thickness is much shorter than the length over which walk-off becomes appreciable. The mixing term d_{eff} was also computed for both SFG interactions considered using Miller's Rule [114]. All calculated values were input to SNLO's 2D short-pulse mixing simulator along with reasonable estimates for input pulse energies and durations. For the simulation inputs, the $1.8\mu m$ pulse was assumed to have an energy of $1\mu J$, a pulse duration of 100fs, and a spot size of $\sim 40\mu m$ at the BBO crystal. The harmonic pulse energies were taken from Table 4.2 for harmonic orders 5 - 11, and scaled according to observed relative spectral powers for harmonic orders 13 and 15. For harmonic order q, the pulse duration was assumed to follow the scaling $\tau_q = \frac{\tau_{3.6\mu m}}{\sqrt{q}}$, where $\tau_{3.6\mu m} = 120$fs (FWHM) was assumed from previous measurements [115]. Spot sizes for the harmonics were estimated assuming a collimated beam with a fixed 25mm initial beam diameter and an $f = 500$mm focusing optic.

A summary of the simulation results is shown in Table 4.3. In practice, it was found that due to the large difference in energy between adjacent harmonic orders, it was necessary to tune the phase-matching angle slightly (generally by 1° or less) to favor the SFG process for the weaker of the two harmonic orders. This de-tuning from the designed phase-matching angle was required to place an approximately equal amount of energy in each harmonic order's XFROG signal beam so that the gain and integration time on the intensified CCD attached to the spectrometer could

θ (deg)	z (μm)	Interaction	d_{eff} (pm/V)	U_{harmonic} (pJ)	U_{SFG} (pJ)	Efficiency (%)
27.5	50	H5 + H2	1.633	100	36.4	36.4
		H7 + H2	1.692	71.1	41.5	58.4
30	50	H7 + H2	1.639	71.1	31.2	43.9
		H9 + H2	1.706	15.35	9.27	60.4
33	30	H9 + H2	1.637	15.35	3.99	26
		H11 + H2	1.719	6.63	2.29	34.5
36.3	20	H11 + H2	1.638	6.63	1.19	17.9
		H13 + H2	1.736	0.221	0.048	21.7
40.2	10	H13 + H2	1.624	0.221	0.0137	6.2
		H15 + H2	1.754	0.0663	0.0051	7.7

Table 4.3: SFG simulation summary for the five designed β-BBO crystals: phase matching angle θ, crystal thickness z, designed interactions, mixing strength d_{eff}, input harmonic energy, output SFG energy, and conversion efficiency. For all simulations, the 1.8μm gate pulse had 1μJ pulse energy and $\tau = 100$fs (FWHM) duration.

be optimized to maximize signal-to-noise. Use of a BBO crystal at its designed phase-matching angle usually results in one of the two XFROG traces containing a peak value decreased in magnitude by one order or more compared to the stronger XFROG trace.

4.1.2 Layout

The layout for the mid-IR harmonics XFROG is shown in Fig. 4.3. A train of 3.6μm pulses with $U \sim 130\mu$J and $\tau \sim 120$fs at 1kHz repetition rate is produced by difference frequency generation between $\lambda_0 = 815$nm, $\tau \sim 100$fs, ~ 3mJ pulses from a CPA Ti:sapphire laser and $\lambda_0 = 1053$nm, $\tau \sim 16$ps, $U \sim 700\mu$J pulses from a direct amplification Nd:YLF laser in a 5mm thick $KTiOAsO_4$ (KTA) crystal; this laser is the femtosecond successor to the picosecond mid-IR source used for prior time-domain Cs harmonics studies [58]. The mid-IR beam is collimated at a diameter of ~ 25mm and sent via beam tube into the target room; after passage through the target room entrance window the pulse energy is $\sim 100\mu$J.

The beam entering the target room is p-polarized (polarization parallel to the table plane). Immediately following the entrance window, a periscope is used to rotate the beam to s-polarization. A small portion of the beam ($\sim 7\%$) is split

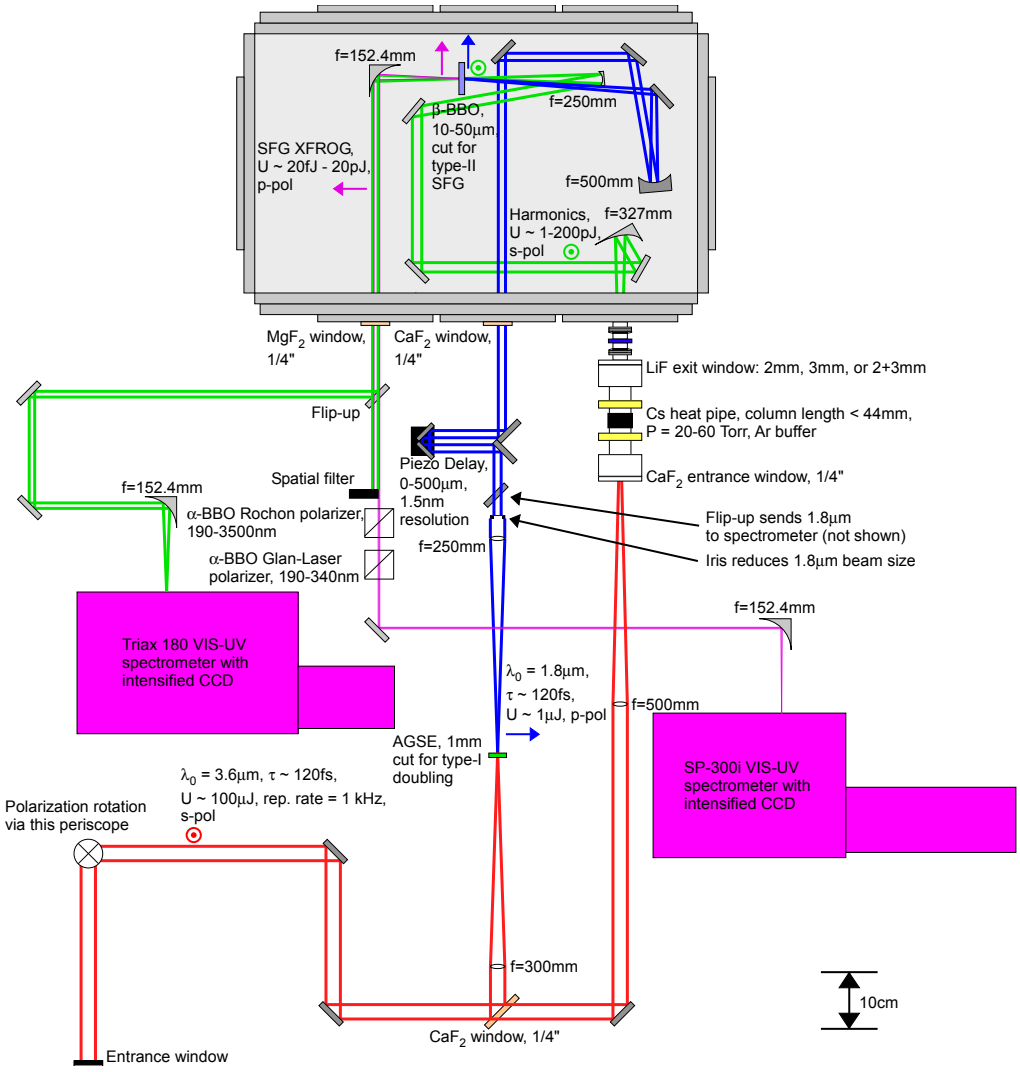

Figure 4.3: Optical layout for the mid-IR harmonics XFROG.

from the beam using the first Fresnel reflection from a CaF_2 window. This weak pulse replica is then focused into an AGSE crystal to generate the required 1.8μm gate pulse. If the polarization is not first rotated, the Fresnel reflection coefficient for p-polarized 3.6μm light at 45° on a CaF_2 window is only $\sim$ 0.5%; this would result in a 1.8μm pulse with too little energy for use in the SFG mixing process. Rotation to s-polarization also adds benefit in the remaining transport optics; since s-polarized reflections are almost always more efficient than p-polarized reflections, a higher energy throughput is maintained for the harmonics beam line up to the BBO

crystal.

The 1.8μm beam is collimated and sent through a variable delay line consisting of a hollow retro-reflector with a gold coating mounted on a closed-loop piezo with 500μm range and 1.5nm resolution. Following the delay line, the 1.8μm beam is sent into a vacuum chamber through a CaF_2 window and focused on the BBO crystal using a mirror with focal length $f = 500$mm. A second 1.8μm pulse originating from the reflection off of the back face of the CaF_2 beam splitter is also present, however this extra pulse is more than 70ps delayed from the pulse generated from the front surface reflection and almost entirely misses apertures downstream from the beam splitter; the combination of energy loss and beam profile distortion due to clipping and temporal lag behind the desired 1.8μm pulse make it quite easy to distinguish an XFROG signal that is generated using the 1.8μm pulse due to the front surface reflection from an XFROG signal resulting from mixing with the 1.8μm from the back surface reflection. Any SFG mixing with the back surface 1.8μm pulse is very weak, if possible to find at all. If an SFG XFROG from the 1.8μm pulse originating from the beam splitter's back surface reflection is found, it is a trivial matter to move the manual delay stage underneath the piezo delay line to correct the timing and overlap the harmonics with the correct 1.8μm pulse. The delay between the two 1.8μm pulses is almost two orders of magnitude larger than the total extent of delays scanned when acquiring an XFROG trace; thus, the presence of a second 1.8μm pulse has no impact on the SFG process.

The majority of the 3.6μm light is transmitted through the beam splitter and focused into a Cs heat pipe using an $f = 250$mm CaF_2 lens. The heat pipe consists of a stainless steel tube with water-chilled copper cooling blocks mounted 22mm on either side of the pipe center. A 25mm-long heater coil surrounds the center of the

pipe, as shown in Fig. 4.3. The interior wall of the pipe is lined with a stainless steel mesh, which acts as a wick for Cs to flow from the cooled regions near the cooling block back towards the heated center region. Window holders are mounted at either end of the pipe using compression fittings, and both window holders are attached to an Ar buffer gas delivery manifold via vacuum rated flexible plastic tubing.

The Ar delivery manifold consists of a low-pressure regulator capable of regulating down to $\sim$ 10Torr, a leak valve connected to a roughing pump, and appropriate gauges and bypass connections. The manifold delivers a constant Ar pressure to the heat pipe; the Ar acts as a buffer between the Cs and the windows, for the most part preventing the Cs from escaping the confines of the cooling blocks. Under ideal operation, the heater power is adjusted until it applies exactly the right amount of thermal load to maintain a Cs vapor pressure which is equal to the pressure of the Ar buffer gas. A twisted wire thermocouple attached to the exterior of the heater provides useful information about when this condition has been achieved. If the applied power is too high or too low, the heat pipe does not reach equilibrium operation and the temperature read from the thermocouple is unstable.

At the heat pipe entrance window, the 3.6μm pulse energy is $\sim 80\mu$J. The 3.6μm beam is focused to an intensity $I = 2.65 \times 10^{12}\text{W/cm}^2$ at a point very close to the exit window side of the Cs column. At this intensity, $U_p = 3.20$, and $\gamma = 0.78$. The 3.6μm beam and the generated harmonics exit the heat pipe through a LiF output window directly into the vacuum chamber. To allow for adjustment of the focal position within the Cs column, the heat pipe exit window holder is coupled to the vacuum chamber using a flexible bellows, and the entire heat pipe assembly rests on a translation stage. An $f = 327$mm off-axis parabaloidal mirror collimates the generated harmonics, which are then focused on the BBO using an $f = 250$mm

spherical mirror. All optics in the harmonics beam line after the heat pipe are coated with UV-enhanced aluminum to ensure the best possible energy throughput of the higher harmonic orders.

The harmonics beam and the 1.8μm beam intersect at the BBO crystal at an angle of $\sim 3^{\circ}$. After the mixing crystal, the harmonics beam and SFG XFROG signal beam are collimated using an $f = 152.4$mm off-axis parabaloid and exit the vacuum chamber through an MgF_2 window. After filtering the SFG signal from the harmonics signal, the XFROG beam is focused on the slit of an $f/4$ imaging monochrometer with an intensified CCD head and UV-blazed gratings using another $f = 152.4$mm off-axis parabaloid.

Since we use a type-II (e,o,e) process to generate the XFROG signal, it would seem natural that the primary means for isolating the XFROG signal from the residual harmonics beam would be through the use of polarizers. Two polarizers are employed in this setup: the first is an α-BBO Rochon polarizer, used to deviate unwanted harmonics of all orders away from the beam path leading to the spectrometer. At higher frequencies, where the XFROG signal is much weaker, a second polarizer is added for improved extinction of the background harmonics. This is an α-BBO Glan-Laser polarizer, cut for wavelengths $\lambda < 300$nm. For wavelengths > 330nm, this polarizer does not work and the introduction of its four interfaces into the beam only serves to increase scattering and reduce signal-to-noise. Even using these two polarizers, however, it was found that additional filtering must be employed to remove unwanted harmonics background from the XFROG signal.

The non-collinear geometry employed in the mixing of the 1.8μm and harmonics beams provides a solution to the signal-to-noise problem. Conservation of momentum during the SFG process dictates that $\overrightarrow{\mathbf{k}}_{\mathrm{SFG}} = \overrightarrow{\mathbf{k}}_{1.8\mu\mathrm{m}} + \overrightarrow{\mathbf{k}}_{q}$ when mixing harmonic

order q with the 1.8μm beam. As a consequence, the SFG XFROG signal exits the BBO crystal at a slightly different angle than the harmonics beam. After collimation, both the SFG and harmonics beams travel along the same angle, since they both originated from the same source, however the angular separation between the two beams is translated into a small spatial separation of the beams. For a 3° mixing angle, only the XFROG signal from the H5 + H2 process is entirely spatially separable from the harmonics background after re-collimation. As the harmonic order q mixed with the 1.8μm beam increases, the angle between the SFG XFROG signal and the harmonics beams decreases, and the area of spatial overlap between the beams increases accordingly. It was found, however, that the use of a knife edge as a spatial filter following the MgF_2 exit window to block the majority of the harmonics beam while still allowing some fraction of the XFROG signal beam to pass was a sufficient additional filtering technique to allow for collection of nearly background-free XFROG traces.

Employing the spatial filter in conjunction with a Rochon polarizer reduces the background harmonics level to $< 0.3\%$ vs. the peak of the XFROG signal for H5/7/9 + H2 processes. For the H11/13 + H2 processes, the spatial filter must be less aggressive, since the spatial overlap between the XFROG signal and the harmonics background is so extensive that any attempt to completely remove the harmonics beam via the spatial filter also removes enough of the XFROG signal to make it nearly undetectable. However, the addition of the Glan-Laser polarizer when performing SFG processes H11/13 + H2 effectively removes the remainder of the unwanted harmonics background, and the observed background signal level for these traces was $< 0.1\%$. Increasing the angle between the 1.8μm beam and the harmonics beam is another possible method for obtaining better spatial separation between the har-

monics and XFROG beams, however the mixing conversion efficiency was observed to drop dramatically for angles $> 4°$, making the higher order FROG traces much more difficult to detect. The inability of the Rochon polarizer to better isolate the XFROG signal from the harmonics beam is attributed primarily to scattering: The BBO crystals are so thin that they require a 1mm-thick UV fused silica substrate for support. This added glued interface, combined with the glued interface between the two crystals in the Rochon polarizer and the poor surface quality of the collimating off-axis parabaloid (diamond-turned) results in a level of scattering of the background harmonics sufficient to defeat the Rochon polarizer when it is employed as the only filter in the system.

In addition to the optics necessary for the XFROG setup, flip-up mirrors were installed to allow the harmonics beam and the 1.8μm beam to be sent to separate spectrometers. The spectrometer for the 1.8μm beam consists of an imaging monochrometer with a 147 lines/mm groove density grating and an InGaAs linear array for detection. The spectrometer used for capturing harmonics spectra is similar to that used for collecting XFROG scans. The spectrometer used for the XFROG scans is highly UV-biased: all gratings on the turret are blazed for 130nm, and the MCP intensifier is unresponsive to IR illumination, making it impossible to examine the 5^{th} harmonic directly using this spectrometer. Shown in Fig. 4.3 is another imaging monochrometer with ICCD detector; this spectrometer, however, has gratings and MCP designed such that the 5^{th} harmonic can be observed.

4.1.3 Dispersion Management

In the absence of a windowless heat pipe, some technique is required to account for the dispersion due to the heat pipe exit window if any meaningful reconstruction

of the relative phase of the harmonics is to be achieved. During the first experimental runs, the heat pipe exit window was a 1/4"-thick UV fused silica window. It was quickly determined, however, that the relative difference in group delay between harmonic orders due to the dispersion of the exit window far exceeded any tolerable value: the observed delay between the H5 + H2 and H7 + H2 XFROG traces was nearly 1ps. Taking small ($\sim$ 1fs) steps to make sure all temporal features are captured on each trace, it took well in excess of one hour to complete a single scan using the thick SiO_2 window. Moving to higher orders only exacerbates the problem, since the dispersion characteristics of fused silica become less desirable at shorter wavelengths. Lithium fluoride (LiF) was chosen as the best of the available materials to replace the original output window since it has the lowest index of all UV-transparent glasses.

Unfortunately, knowledge of the window thickness and material is not precise enough to allow for accurate removal of the incurred dispersion. Simulations using index data for the purest grade of the Lithosil product line from Schott Glass, a synthetic fused silica that is one of the most accurately characterized materials commercially available, revealed that a 1/4"-thick Lithosil output window would mandate error bars ranging from 87as to 6.4fs in the group delay calculated from each harmonic order, as shown in Fig. 4.4. These error bars would be due solely to the uncertainty in the tabulated refractive index data for the material, presuming that the window thickness is known exactly. For a more poorly characterized material such as LiF, it is clear that reliance on published models for the index of the material is insufficient for accurate removal of the LiF dispersion, especially when the existing models [116, 117, 118, 119] do not cover the entire spectral range spanned by the XFROG. Building a separate refractometer or equivalent device to measure the index of the output window over the spectral range required is also not

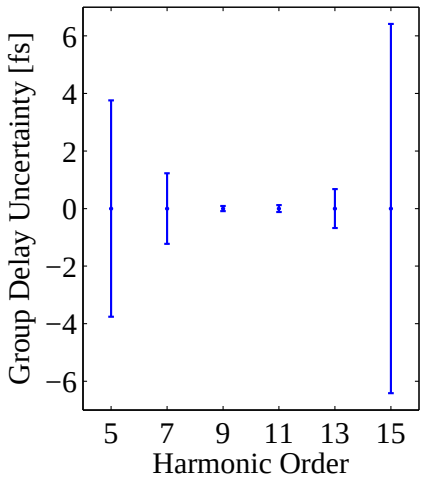

Figure 4.4: Group delay error bars for Lithosil grade H5, 1/4" thickness.

an option, since the measurement uncertainty would again be far larger than any reasonable limit for pulse reconstruction. Instead, the XFROG itself was used as the LiF characterization device.

The scheme for characterizing the LiF contribution to the observed delay between harmonic orders is as follows: two LiF output windows are used during the collection of the XFROG data, one window has a thickness of 2mm, while the other is 3mm thick. A full set of overlapping XFROG traces is collected using first the 2mm LiF window: H5/7 + H2, H7/9 + H2, etc. The output window is then replaced with the 3mm window, and all scans are collected a second time. Finally, the 2mm window is stacked with the 3mm window to effectively produce a single 5mm LiF output window, and all XFROG scans are collected a third time. In the absence of a vacuum chamber, let the observed delay between adjacent harmonic orders i, j through window x, be expressed as $\tau^{(x)}\big|_i^j = \tau_{\text{gen}}\big|_i^j + \tau_{\text{Cs}}\big|_i^j + \tau_{\text{Ar}}\big|_i^j + \tau_{\text{LiF x}}\big|_i^j + \tau_{\text{Air}}\big|_i^j$, where $\tau_{\text{gen}}\big|_i^j$ is the attochirp + intensity-dependent chirp between orders i, j, $\tau_{\text{Cs}}\big|_i^j$ is due to propagation through the remainder of the Cs column, $\tau_{\text{Ar}}\big|_i^j$ is due to propagation through the Ar buffer gas, $\tau_{\text{LiF x}}\big|_i^j$ is due to propagation through window x, and $\tau_{\text{Air}}\big|_i^j$

is due to propagation in the air column between the heat pipe and the SFG mixing crystal. The three previously described XFROG data sets are then

$$\begin{aligned}
\tau^{(2\text{mm})}\big|_i^j &= \tau_{\text{gen}}\big|_i^j + \tau_{\text{Cs}}\big|_i^j + \tau_{\text{Ar}}\big|_i^j + \tau_{\text{LiF 2mm}}\big|_i^j + \tau_{\text{Air}}\big|_i^j \\
\tau^{(3\text{mm})}\big|_i^j &= \tau_{\text{gen}}\big|_i^j + \tau_{\text{Cs}}\big|_i^j + \tau_{\text{Ar}}\big|_i^j + \tau_{\text{LiF 3mm}}\big|_i^j + \tau_{\text{Air}}\big|_i^j \\
\tau^{(5\text{mm})}\big|_i^j &= \tau_{\text{gen}}\big|_i^j + \tau_{\text{Cs}}\big|_i^j + \tau_{\text{Ar}}\big|_i^j + \tau_{\text{LiF 5mm}}\big|_i^j + \tau_{\text{Air}}\big|_i^j
\end{aligned} \tag{4.7}$$

Re-arranging,

$$\tau_{\text{gen}}\big|_i^j + \tau_{\text{Cs}}\big|_i^j + \tau_{\text{Ar}}\big|_i^j + \tau_{\text{Air}}\big|_i^j = \tau^{(2\text{mm})}\big|_i^j + \tau^{(3\text{mm})}\big|_i^j - \tau^{(5\text{mm})}\big|_i^j \tag{4.8}$$

Thus, through the collection of three complete XFROG data sets using two output windows, the relative delay due to the output window material is completely removed, even though the precise thickness and refractive indices of the windows is not known. It is easy to show that this simple subtraction technique can also be used to completely remove the LiF contribution to the spectral phase for an individual harmonic order q retrieved by the FROG retrieval algorithm. This may be inadvisable, however, since the spectral phase where the retrieved power is low is less reliable, and therefore the difference between three phase functions would be highly questionable in regions with low spectral power. Instead, a technique using the observed delays $\tau^{(x)}\big|_i^j$ is adopted as follows: the delay due to the 2mm LiF window can be calculated using Eq. 4.7 as

$$\tau_{\text{LiF 2mm}}\big|_i^j = \tau^{(5\text{mm})}\big|_i^j - \tau^{(3\text{mm})}\big|_i^j \tag{4.9}$$

The total group delay response for the 2mm window is then obtained through con-

catenation of Eq. 4.9, where the delay at harmonic order 5 is arbitrarily set to 0:

$$
\begin{aligned}
\tau_{\text{LiF 2mm}}\big|_5 &= 0 \\
\tau_{\text{LiF 2mm}}\big|_7 &= \tau_{\text{LiF 2mm}}\big|_5^7 \\
\tau_{\text{LiF 2mm}}\big|_9 &= \tau_{\text{LiF 2mm}}\big|_7^9 + \tau_{\text{LiF 2mm}}\big|_7 \\
\tau_{\text{LiF 2mm}}\big|_{11} &= \tau_{\text{LiF 2mm}}\big|_9^{11} + \tau_{\text{LiF 2mm}}\big|_9 \\
\tau_{\text{LiF 2mm}}\big|_{13} &= \tau_{\text{LiF 2mm}}\big|_{11}^{13} + \tau_{\text{LiF 2mm}}\big|_{11} \\
\tau_{\text{LiF 2mm}}\big|_{15} &= \tau_{\text{LiF 2mm}}\big|_{13}^{15} + \tau_{\text{LiF 2mm}}\big|_{13}
\end{aligned}
\tag{4.10}
$$

The function $\tau_{\text{LiF 2mm}}(\omega)$ is directly related to the group index of the 2mm LiF window $n_g(\omega)$ via

$$\tau_{\text{LiF 2mm}}(\omega) = \frac{z n_g(\omega)}{c} \tag{4.11}$$

where z is the window thickness. Noting that

$$n_g(\omega) = n(\omega) + \omega \frac{\mathrm{d}n(\omega)}{\mathrm{d}\omega} \tag{4.12}$$

and the spectral phase $\phi(\omega)$ is given by

$$\phi(\omega) = n(\omega)\frac{z\omega}{c} \tag{4.13}$$

the derivative $\mathrm{d}\phi(\omega)/\mathrm{d}\omega$ is given by

$$\frac{\mathrm{d}\phi(\omega)}{\mathrm{d}\omega} = \frac{z}{c}\left(n(\omega) + \omega\frac{\mathrm{d}n(\omega)}{\mathrm{d}\omega}\right) = \frac{z n_g(\omega)}{c} \tag{4.14}$$

Thus, Eq. 4.10 represents an evaluation of $\mathrm{d}\phi(\omega)/\mathrm{d}\omega$ at a discrete set of frequencies, plus a constant. Let $F(\omega)$ represent this evaluation:

$$F(\omega) = \frac{\mathrm{d}\phi(\omega)}{\mathrm{d}\omega} - \left.\frac{\mathrm{d}\phi(\omega)}{\mathrm{d}\omega}\right|_{\omega_5} \tag{4.15}$$

Integrating one time,

$$G(\omega) = \int_{-\infty}^{\infty} F(\omega)\mathrm{d}\omega = \phi(\omega) - \omega\left.\frac{\mathrm{d}\phi(\omega)}{\mathrm{d}\omega}\right|_{\omega_5} + C \tag{4.16}$$

Adopting a polynomial expansion for the spectral phase about a carrier frequency ω_0,

$$\phi(\omega - \omega_0) = \sum_{i=0}^{\infty} \phi_i \times (\omega - \omega_0)^i \tag{4.17}$$

we neglect the $i = 0$ and $i = 1$ terms, since these represent the carrier-envelope phase and temporal delay, respectively. Thus, the last two terms of Eq. 4.16 can be neglected, and we can obtain the appropriate spectral phase for the 2mm LiF window at a given harmonic order q by simply interpolating Eq. 4.10 to a more densely spaced vector in ω-space, integrating one time, performing a polynomial projection to sufficiently high order about the carrier frequency $\omega_{0,q}$, and throwing out the DC and linear terms. An identical application of this technique can be applied to obtain the spectral phase contribution from the 3mm LiF window, if desired.

Through the use of two windows and three complete XFROG data sets it is therefore possible to completely characterize and remove the effects of both the refractive index $n(\omega)$ and the group index $n_g(\omega)$ without any prior knowledge of the windows' dispersion characteristics or thicknesses. As a byproduct of this technique, the dispersion properties of both output windows are quite well characterized; an accurate measurement of the thicknesses of both windows should allow for the construction of an index model for both windows. This modeling along with appropriate error analysis is left for future work, since it is outside the scope of the current effort to characterize the windows beyond the ability to remove their dispersion effects from the data.

Examination of Eq. 4.8 reveals another potential dispersion-related problem, however. Initial iterations of this experiment did not include a vacuum chamber because it was not fully recognized in advance how serious a problem it would be to propagate the harmonics in air. After generation, the harmonics exited the heat pipe into

air and propagated for $\sim$ 3m before mixing with the 1.8μm beam. Analysis of the data from these early experimental runs revealed that dispersion in air presented a significant hurdle to any meaningful analysis of the data.

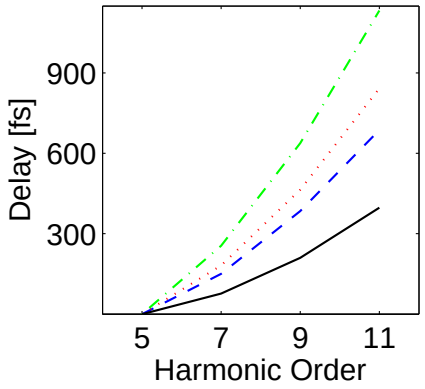

Figure 4.5: Dispersion in air; retrieved delay vs. harmonic order for 2mm LiF (blue, dashed), 3mm LiF (red, dotted), 5mm LiF (green, dash-dot), and after removing the LiF contribution using Eq. 4.8 (black, solid).

Fig. 4.5 shows the results from attempting to apply Eq. 4.8 to an XFROG data set spanning harmonics 5-11 with $\sim$ 3m air propagation between the heat pipe output window and the BBO SFG crystal. A quick examination of the data shows that the dispersion due to air is of the same order as that created by the output windows, themselves. Attempts were made to subtract the residual air dispersion using a Nelder-Mead Simplex constrained optimization routine [120] to find the values for air temperature, pressure, relative humidity, and CO_2 concentration that minimized the range of the dispersion curve, however the uncertainty in the dispersion models for air [121, 122, 123, 124] and the sensitivity of the result to mm-scale changes in the best-fit air column length and $1/10^{\text{th}}$-degree changes in best-fit temperature cast serious doubts on the obtained results.

One simple solution to the problem presented by the air is to box the entire experiment and back-fill with a slight over-pressure of helium. Index models for

He [125, 126, 127, 128, 129] indicate that replacing the 3m air column with a slightly over-pressurized He environment, 800Torr at 30°C, will reduce the delay between the 11^{th} harmonic relative to the 5^{th} harmonic from $\sim$ 408fs to $\sim$ 19fs. While this is certainly a significant improvement, the effort required to retrofit a He delivery/containment environment around the existing experimental setup that could be safely operated without risk of asphyxiation is similar to and possibly more difficult than simply placing the entire harmonics arm of the XFROG between the heat pipe exit window and the SFG crystal in a vacuum environment. Eschewing the He back-fill option, the experiment was instead re-designed to operate under vacuum, as previously described in Sec. 4.1.2. The path length between the heat pipe output window and the SFG crystal was reduced from 3m to 1.5m, and the number of mirrors between the output window and SFG crystal was reduced from 8 to 5. The Edlén air model [121] and Muijlwijk update to the model [122] were used to estimate the vacuum level required for dispersion-free operation; these simulation results are shown in Fig. 4.6. The group delay vs. pressure simulations show that at a pressure

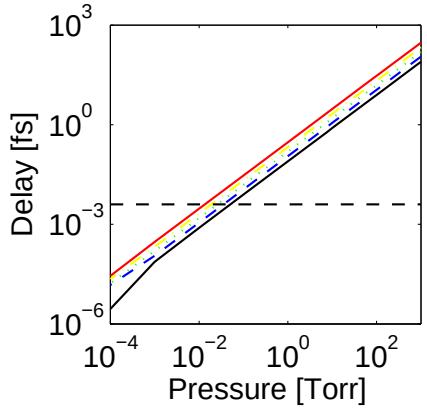

Figure 4.6: Group delay due to air for H7-15 relative to H5 vs. pressure for 1.5m propagation: H7 (black, solid), H9 (blue, dashed), H11 (green, dotted), H13 (yellow, dash-dot), and H15 (red, solid). The horizontal dashed line represents 4as delay.

of 100mTorr, the 15^{th} harmonic will be delayed relative to the 5^{th} harmonic by less

than 4as. Anticipating that the attochirp will be on a time scale of the same order of magnitude as 1/4-cycle of the 3.6μm driving pulse ($\sim$ 3fs), a 4as contribution from residual gas content in the vacuum chamber was deemed acceptable. Furthermore, a pressure of 100mTorr or less is easily attainable with a roughing pump only; a turbo-molecular pump is not required to achieve or maintain the required vacuum level, which allows operation without the annoyance of vibrations due to a running turbo pump. Long segments of flexible PVC vacuum hose were installed between the roughing pump and the vacuum chamber to minimize any transmission of mechanical vibration from the pump to the optics. Removing air from the system has dramatic results: Fig. 4.7 shows the H9/11 + H2 XFROG trace taken in the presence of 3m of air propagation, while Fig. 4.8 shows the same XFROG trace taken under vacuum ($P_{vac} \sim$ 85mTorr).

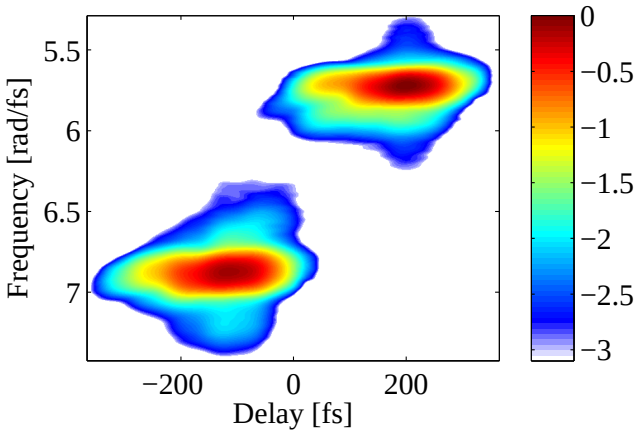

Figure 4.7: H9 + H2 and H11 + H2 XFROG with 2mm LiF window: 3m air propagation, Cs pressure = 60Torr.

Temporal/spectral differences between the individual XFROG traces embedded in each scan are attributed primarily to different operating conditions: the scan taken with the air column present used a Cs vapor column at a pressure of 60Torr, while the scan taken under vacuum used a 20Torr Cs source and a lower peak intensity at

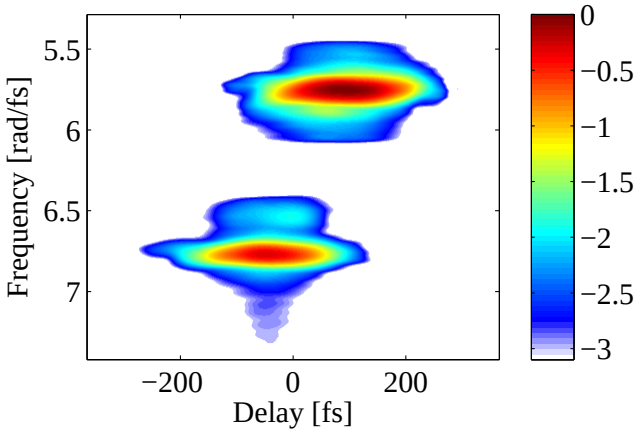

Figure 4.8: H9 + H2 and H11 + H2 XFROG with 2mm LiF window: propagation in vacuum, Cs pressure = 20Torr.

focus. In the absence of air, Eq. 4.7 must be modified to exclude $\tau_{\mathrm{Air}}\big|_i^j$ terms:

$$\begin{aligned}
\tau^{(2\mathrm{mm})}\big|_i^j &= \tau_{\mathrm{gen}}\big|_i^j + \tau_{\mathrm{Cs}}\big|_i^j + \tau_{\mathrm{Ar}}\big|_i^j + \tau_{\mathrm{LiF\ 2mm}}\big|_i^j \\
\tau^{(3\mathrm{mm})}\big|_i^j &= \tau_{\mathrm{gen}}\big|_i^j + \tau_{\mathrm{Cs}}\big|_i^j + \tau_{\mathrm{Ar}}\big|_i^j + \tau_{\mathrm{LiF\ 3mm}}\big|_i^j \\
\tau^{(5\mathrm{mm})}\big|_i^j &= \tau_{\mathrm{gen}}\big|_i^j + \tau_{\mathrm{Cs}}\big|_i^j + \tau_{\mathrm{Ar}}\big|_i^j + \tau_{\mathrm{LiF\ 5mm}}\big|_i^j
\end{aligned} \tag{4.18}$$

and Eq. 4.8 becomes

$$\tau_{\mathrm{gen}}\big|_i^j + \tau_{\mathrm{Cs}}\big|_i^j + \tau_{\mathrm{Ar}}\big|_i^j = \tau^{(2\mathrm{mm})}\big|_i^j + \tau^{(3\mathrm{mm})}\big|_i^j - \tau^{(5\mathrm{mm})}\big|_i^j \tag{4.19}$$

The only remaining un-compensated dispersion, then, is the dispersion due to the $\sim$ 75mm Ar column and the propagation of the harmonics through Cs. Unfortunately, it is not possible to remove these contributions through any means similar to that used to compensate the LiF contribution; other measurements and modeling are needed to attempt to account for these two terms.

4.1.4 Alignment Procedure

Alignment of the XFROG begins by aligning the 3.6μm beam entering the target room through a pair of well-separated irises placed immediately following the polarization-rotating periscope. A thermal imaging camera is used to accomplish all

mid-IR alignment prior to the vacuum chamber. Irises are placed after each mirror in the system, allowing for fine tuning of each mirror to get the 3.6μm beam on the correct beam path for both the 1.8μm and harmonics beam lines.

Spatial alignment in the vacuum chamber is done at atmospheric pressure. Once the 3.6μm beam is verified to travel properly along the harmonics beam line, the Cs heat pipe is introduced. The energy in the generated harmonics is sufficiently high that all post-heat pipe optics can be aligned to the in-chamber irises by eye using the two visible harmonic orders (7 and 9). A 10μm-diameter pinhole is installed in the BBO crystal mount and an 1mm^2 InGaAs photodiode with linear response from 1.2μm $-$ 1.8μm is placed immediately behind the pinhole. The 1.8μm beam is blocked and the crystal mount is then translated in both the x and y-dimensions until the 3$^{\text{rd}}$ harmonic passes through the pinhole and a signal from the photodiode is visible on an oscilloscope. Further translation in x, y, and z-dimensions of the crystal mount are made to optimize the pinhole position to the center of the beam and center of the Rayleigh range.

Once the pinhole is positioned properly, the harmonics beam is blocked and the 1.8μm beam is un-blocked. Using a small piece of thermochromatic paper to locate the 1.8μm beam near focus, the tip/tilt axes on the $f = 500$mm focusing mirror are adjusted until it appears the 1.8μm beam is hitting the pinhole. A blind search of the tip/tilt axes follows until the 1.8μm beam registers on the InGaAs photodiode. To maximize the 1.8μm signal on the photodiode, the z position of the collimating lens immediately following the AGSE crystal is scanned in conjunction with tip/tilt adjustments on the $f = 500$mm mirror. Adjusting the position of the collimating lens corrects the wavefront of the 1.8μm beam so that any error in the placement of the $f = 500$mm mirror with respect to the pinhole z position is canceled out, and

the 1.8μm beam focuses in the same plane as the harmonics.

Once the spatial overlap of both beams is achieved, the pinhole is removed and the 1.8μm beam is blocked. The harmonics beam is used to align all post-SFG optics along the path to the spectrometer. Back reflections from the polarizers are used to verify that the collimated beam hits them at normal incidence, and the polarizers are then adjusted to minimize the observed harmonics spectrum on the spectrometer, thus maximizing the transmission for the FROG signal. The knife-edge spatial filter is then slid into place until the residual background harmonics level is observed to drop by ~ 1 order of magnitude. The BBO crystal cut for optimized phase matching of the H5+H2 and H7+H2 SFG processes is installed in the crystal mount and the goniometric angle control on the mount is adjusted so that the back reflection from the SFG crystal travels exactly back along the original beam path. The piezo is commanded to move half of its total available displacement. Both beams are then allowed through, and the manual stage beneath the piezo is adjusted until either the H5+H2 or H7+H2 XFROG signal is visible on the spectrometer. To achieve temporal overlap for the first time after constructing the XFROG, the crystal mount is removed and a Newport D-30 high-speed photodiode with 30ps rise time and a linear response from 950-1650nm is installed at focus. The 3$^{\text{rd}}$ harmonic easily fits within the spectral range of this diode, and a signal from the 1.8μm beam is also visible, even though the diode is not specified to respond at 1.8μm. The fast photodiode is connected to an analog oscilloscope and the manual delay control is adjusted until no delay between the harmonics and 1.8μm beams is evident. Using the fast photodiode only gets the temporal overlap to within $\pm$100ps. Upon completion of this step, it is necessary to use the XFROG signal itself as previously described as the final verification that temporal overlap has been achieved.

Once spatial and temporal overlap are obtained, the vacuum chamber is closed and evacuated. Since the removal of air necessarily changes the timing overlap between the 1.8μm and harmonics beams, a small adjustment of the manual delay stage between air and vacuum settings is required. For example, the H7 + H2 XFROG signal required a $\sim 220\mu$m shorter beam path for the 1.8μm beam with the chamber evacuated in order to maintain temporal overlap. Since the chamber floor is not isolated, the spatial overlap between the beams is also disturbed when pumping as the chamber is deformed. The final air-side mirror in the 1.8μm beam line is mounted on a mirror mount with micrometers instead of the usual thumb screws to control mirror tip/tilt. For first-time evacuation after constructing the XFROG, the pumping process is completed in many small steps: pump until the XFROG signal diminishes in intensity by a factor of 3 or 4, then stop pumping and re-optimize the spatial overlap with the last air-side 1.8μm mirror mount while also adjusting the temporal overlap to achieve the strongest possible XFROG signal. This process is repeated many times until the pressure in the chamber is near 1Torr. At this point, further pumping to lower pressures has little impact and the chamber is evacuated as quickly as possible: the chamber is fully deformed, therefore the spatial overlap will not change with further pressure decrease, and the changes to the timing overlap are smaller than can be adjusted using the manual delay stage. The recorded difference in the micrometer settings for the last 1.8μm mirror and the manual delay stage are used on subsequent transitions from air to vacuum alignment. Once the difference in these micrometer settings is known, it is possible to evacuate the chamber at full speed without bothering to maintain spatial or temporal overlap between the beams. The deformation of the chamber is repeatable enough that the XFROG signal can be recovered after pulling vacuum by simply applying the measured adjustments to

the micrometers after completion of the evacuation process.

When it is necessary to change BBO crystals or alter the output window configuration on the heat pipe, the spatial and temporal overlap are not re-adjusted to their air settings when the vacuum is broken. Instead, with the chamber still under vacuum the piezo is positioned for maximum signal strength for one of its two designed SFG interactions. Both beams are then blocked and the vacuum is broken. After completing the crystal swap or window swap, the vacuum is restored and the beams are allowed through. If necessary, small adjustments are made to compensate any spatial or temporal overlap drift that may have occurred when cycling the vacuum system.

Prior to acquiring XFROG data, an attempt is made to optimize the signal strengths for both XFROG signals to be acquired by adjusting the phase-matching angle θ of the BBO crystal, altering the position of the knife-edge filter, rotating and tilting the polarizers, adjusting the spatial overlap of the two beams, and adjusting the beam pointing into the spectrometer. All these elements are adjusted until both XFROG signals have a peak intensities that are as close to equal as possible and both signals have the maximum obtainable signal-to-noise ratio. Unfortunately, there is no specific procedure for this optimization; the number of free variables to optimize is simply too large. The only technique that works well is to continue adjusting various knobs until the desired results are achieved.

4.1.5 Pulse Retrieval via Double-Constraint PCGPA

After collecting the data from the XFROG experiment, some care must be taken to ensure the accuracy of the pulses retrieved from the FROG traces. As with most FROG geometries, the pulse retrieval algorithm of choice for the mid-IR harmonics

XFROG is the principal components generalized projection algorithm (PCGPA) [130, 131]. PCGPA offers advantages in both speed of convergence and simplicity of implementation versus the "vanilla" FROG algorithm [132, 133], which still requires the use of a user-selected functional minimization routine. The PCGPA algorithm is not, strictly speaking, a functional minimization routine, in that it does not explicitly seek to minimize some figure of merit comparing the experimental data to the retrieved result. Instead, the PCGPA algorithm takes advantage of the one-to-one mapping between the outer product of two complex-valued vectors representing the time-domain electric field for each pulse and the FROG spectrogram. On each iteration the algorithm simply applies the constraint that the magnitude of the trial spectrogram and measured spectrogram must be equal. In its simplest form, the PCGPA algorithm is "blind," in that it does not require any information other than the FROG spectrogram to retrieve both pulses used to create the spectrogram, even if both pulses are unknown. The operation of the blind PCGPA algorithm is as follows: Create two complex-valued trial fields $E_{\mathrm{Probe}}(t)$ and $E_{\mathrm{Gate}}(t)$ with discrete time step Δt.

$$E_{\mathrm{Probe}} = \left[E_1, E_2, E_3, ..., E_N\right] \qquad E_{\mathrm{Gate}} = \left[G_1, G_2, G_3, ..., G_N\right] \tag{4.20}$$

Create the outer product O of $E_{\mathrm{Probe}}(t)$ and $E_{\mathrm{Gate}}(t)$,

$$O = \begin{bmatrix} E_1G_1 & E_1G_2 & E_1G_3 & \cdots & E_1G_N \\ E_2G_1 & E_2G_2 & E_2G_3 & \cdots & E_2G_N \\ E_3G_1 & E_3G_2 & E_3G_3 & \cdots & E_3G_N \\ \vdots & \vdots & \vdots & \cdots & \vdots \\ E_NG_1 & E_NG_2 & E_NG_3 & \cdots & E_NG_N \end{bmatrix} \tag{4.21}$$

Perform a circular shift to the left on each row j by $j-1$ elements,

$$O_{shifted} = \begin{bmatrix} E_1G_1 & E_1G_2 & E_1G_3 & \cdots & E_1G_{N-2} & E_1G_{N-1} & E_1G_N \\ E_2G_2 & E_2G_3 & E_2G_4 & \cdots & E_2G_{N-1} & E_2G_N & E_2G_1 \\ E_3G_3 & E_3G_4 & E_3G_5 & \cdots & E_3G_N & E_3G_1 & E_3G_2 \\ \vdots & \vdots & \vdots & \cdots & \vdots & \vdots & \vdots \\ E_NG_N & E_NG_1 & E_NG_2 & \cdots & E_NG_{N-3} & E_NG_{N-2} & E_NG_{N-1} \\ \tau=0 & \tau=-\Delta t & \tau=-2\Delta t & \cdots & \tau=3\Delta t & \tau=2\Delta t & \tau=\Delta t \end{bmatrix} \tag{4.22}$$

Reverse the order of elements of $O_{shifted}$ column-wise, and the result is the time-domain version of the spectrogram $\tilde{E}_{\mathrm{FROG}}(t,\tau)$,

$$\tilde{E}_{\mathrm{FROG}}(t,\tau) = \begin{bmatrix} \cdots & E_1G_3 & E_1G_2 & E_1G_1 & E_1G_N & E_1G_{N-1} & E_1G_{N-2} & \cdots \\ \cdots & E_2G_4 & E_2G_3 & E_2G_2 & E_2G_1 & E_2G_N & E_2G_{N-1} & \cdots \\ \cdots & E_3G_5 & E_3G_4 & E_3G_3 & E_3G_2 & E_3G_1 & E_3G_N & \cdots \\ \cdots & \vdots & \vdots & \vdots & \vdots & \vdots & \vdots & \cdots \\ \cdots & E_NG_2 & E_NG_1 & E_NG_N & E_NG_{N-1} & E_NG_{N-2} & E_NG_{N-3} & \cdots \\ \cdots & \tau=-2\Delta t & \tau=-\Delta t & \tau=0 & \tau=\Delta t & \tau=2\Delta t & \tau=3\Delta t & \cdots \end{bmatrix} \tag{4.23}$$

where time is read going down the columns and delay τ is read across. A simple Fourier transform column-wise yields the FROG spectrogram $\tilde{E}_{\mathrm{FROG}}(\omega,\tau)$. The magnitude of the spectrogram is then replaced with the measured spectrogram $I_{\mathrm{meas}}(\omega,\tau)$,

$$\tilde{E}_{\mathrm{FROG}}(\omega,\tau) = \tilde{E}_{\mathrm{FROG}}(\omega,\tau)\frac{\sqrt{I_{\mathrm{meas}}(\omega,\tau)}}{\left|\tilde{E}_{\mathrm{FROG}}(\omega,\tau)\right|} \tag{4.24}$$

In the blind PCGPA implementation, replacing $\left|\tilde{E}_{\mathrm{FROG}}(\omega,\tau)\right|$ with $\sqrt{I_{\mathrm{meas}}(\omega,\tau)}$ is the only constraint used. Following application of the data constraint, the inverse Fourier transform is computed column-wise, and the column-swapping and

row-shifting described in Eqs. 4.22 and 4.23 are reversed, yielding a new outer product matrix O. The simplest method to extract the next guess for $E_{\mathrm{Probe}}(t)$ and $E_{\mathrm{Gate}}(t)$ is to perform a singular value decomposition on O and then choose the most strongly weighted vector pair from the resulting orthogonal basis set as the next guess. However, this is computationally intensive. As an alternative, the Power method [134] is used. The Power method requires more iterations to reach the same convergence level as an SVD-based PCGPA implementation, however due to the compute-intensive nature of performing an SVD, the Power method turns out to be significantly faster. To use the Power method to form the $k+1^{\mathrm{th}}$ guess for the gate and probe fields from the matrix O computed on the k^{th} iteration requires simple matrix multiplication:

$$E_{\mathrm{Probe}}^{k+1} = OO^T E_{\mathrm{Probe}}^{k}$$
$$E_{\mathrm{Gate}}^{k+1} = O^T O E_{\mathrm{Gate}}^{k} \tag{4.25}$$

After forming E_{Probe}^{k+1} and E_{Gate}^{k+1}, the outer product is computed and the steps previously described are repeated.

Unfortunately, a blind PCGPA implementation almost never converges to the correct solution. While the FROG trace is over-complete, the search space is NxN, and the blind algorithm often gets stuck in local minima and cannot recover without iterating for an inordinately long period of time. Additional information must be supplied during each iteration to help guide the algorithm along a faster trajectory towards the correct solution. In the case of SHG FROG, this constraint takes the form of recognizing that the probe and gate fields are equal and accordingly modifying the computation of the outer product to reflect this equality. For other geometries where a known mathematical relationship exists between the probe and gate, an appropriate modification can usually be made to incorporate this relationship into the

algorithm as an added constraint. In the case of the XFROG geometry such a relationship does not exist, and other constraints must be sought. The best option for providing an additional constraint for the XFROG PCGPA routine is to independently measure one of the two unknown pulses. Then, each iteration of the algorithm only updates a guess for the one unknown field, while the externally measured field is held constant. However, this requires taking the time and expense to implement an entirely separate pulse measurement device, and is not generally necessary. An alternative constraint is to measure one or both of the unknown pulses' spectra. After forming the next guess for the probe and gate, if a spectrum is available for either pulse it is used to replace the spectrum of the trial pulse while keeping the trial spectral phase intact. This spectral constraint is the first additional constraint used in the processing of the 3.6μm harmonics XFROG data: the spectral power of the 1.8μm beam is measured and used as a constraint in the PCGPA algorithm.

Due to the somewhat unconventional nature of the 3.6μm harmonics XFROG, where a long pulse is used to gate a shorter pulse [135, 136], it turns out that the addition of the 1.8μm spectral power constraint is not sufficient to ensure the consistency of the PCGPA results across multiple FROG traces. Small changes in the spectral phase of the 1.8μm gate result in varying solutions for the harmonics probe; a single harmonic's spectral width was observed to vary by as much as 10% and the spectral phase was observed to vary on the order of 1-2 radians when comparing results from an XFROG trace measuring orders i, j with a trace measuring orders j, k. Choosing one of the two 1.8μm gate pulses and applying it to the probe pulse from the other XFROG trace does not drastically reduce the likelihood that the second trace will reach the defined convergence criterion. Also, the recovered harmonics probe after making this replacement is quite consistent with the probe retrieved from

the first FROG trace. These observations led to the development of a new type of constraint which guarantees self-consistency of the entire data set. All XFROG traces in the data set are processed in parallel, and after each iteration the 1.8μm spectral constraint is applied. The new constraint takes the form of averaging the next guess for the 1.8μm spectral phase from all XFROG traces, forming a single new guess for the gate which is then used to form the outer product with the independently formed probe fields in each trace. The end result is that there are no inconsistencies in the recovered 1.8μm gate, since all traces use a shared gate pulse. The only major drawback in the application of this constraint is that processing many large XFROG traces in parallel can take significant amounts of computation time.

4.2 Experimental Results

Using the XFROG apparatus described in Sec. 4.1, data was acquired for harmonics 5-13 using a 2mm, 3mm, and 2mm+3mm LiF output window on the heat pipe. The 3.6μm focus was measured to be approximately at the location of the output side of the heat pipe cooling block. The Ar backing pressure was 20Torr, and the laser power immediately before the heat pipe input window was measured to be 77mW. For each pair of harmonics i, j measured with a given output window x, 5 scans were acquired with 2 second integrations at each position of the delay stage. Each scan spanned a delay range sufficient to observe only background light on the spectrometer at both ends of the scan. This background light was then averaged in the τ-dimension on a per-scan basis and subtracted from its parent scan. A given set of 5 scans were then averaged to create a single scan, which was then filtered using a weak low-pass Fourier filter. Finally, the filtered scan was interpolated from wavelength to frequency space, with appropriate scaling of the spectral power, to

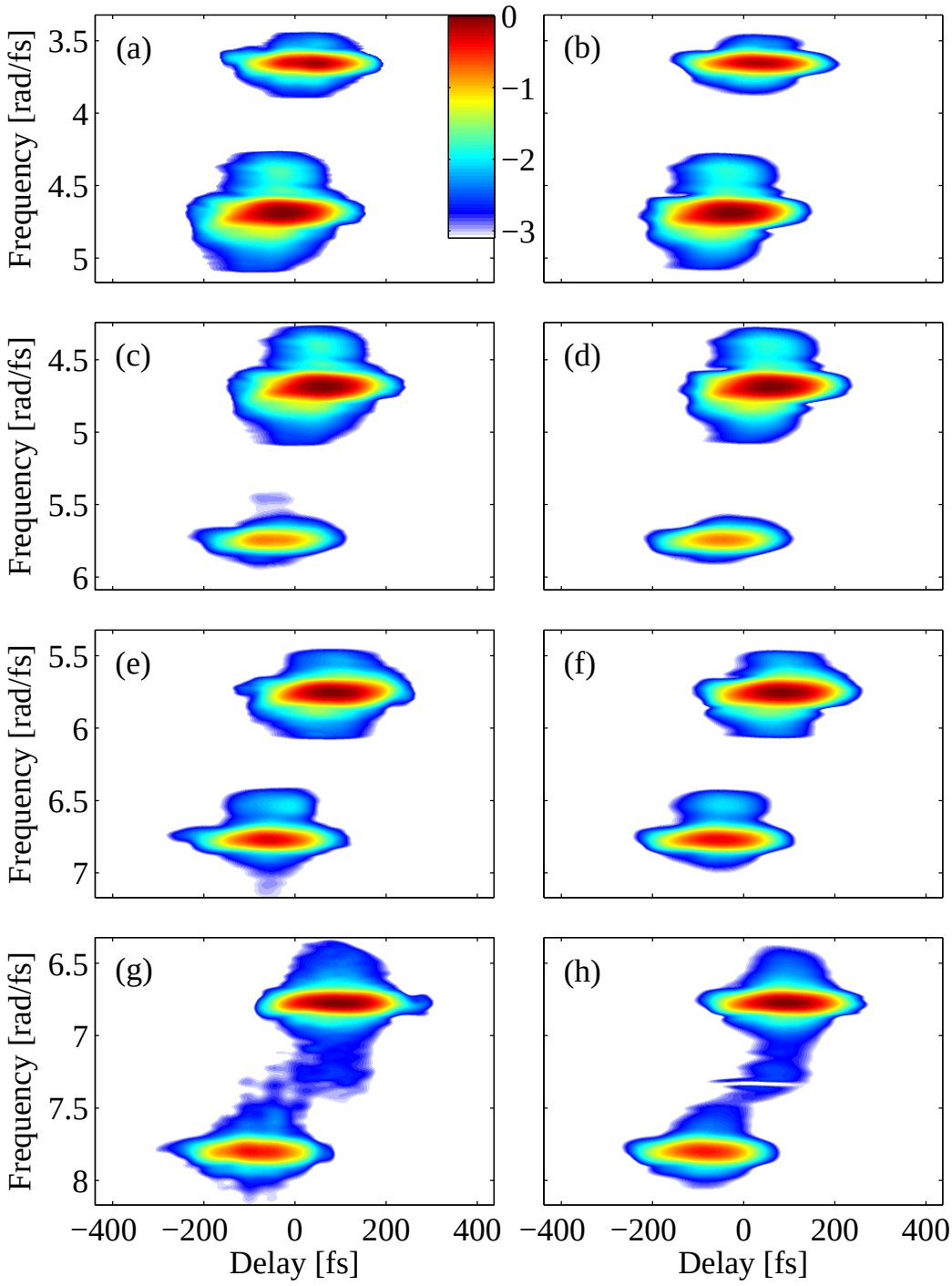

Figure 4.9: XFROG Data with 2mm LiF output window: H5/7 + H2 (a) experimental and (b) retrieved, H7/9 + H2 (c) experimental and (d) retrieved, H9/11 + H2 (e) experimental and (f) retrieved, H11/13 + H2 (g) experimental and (h) retrieved.

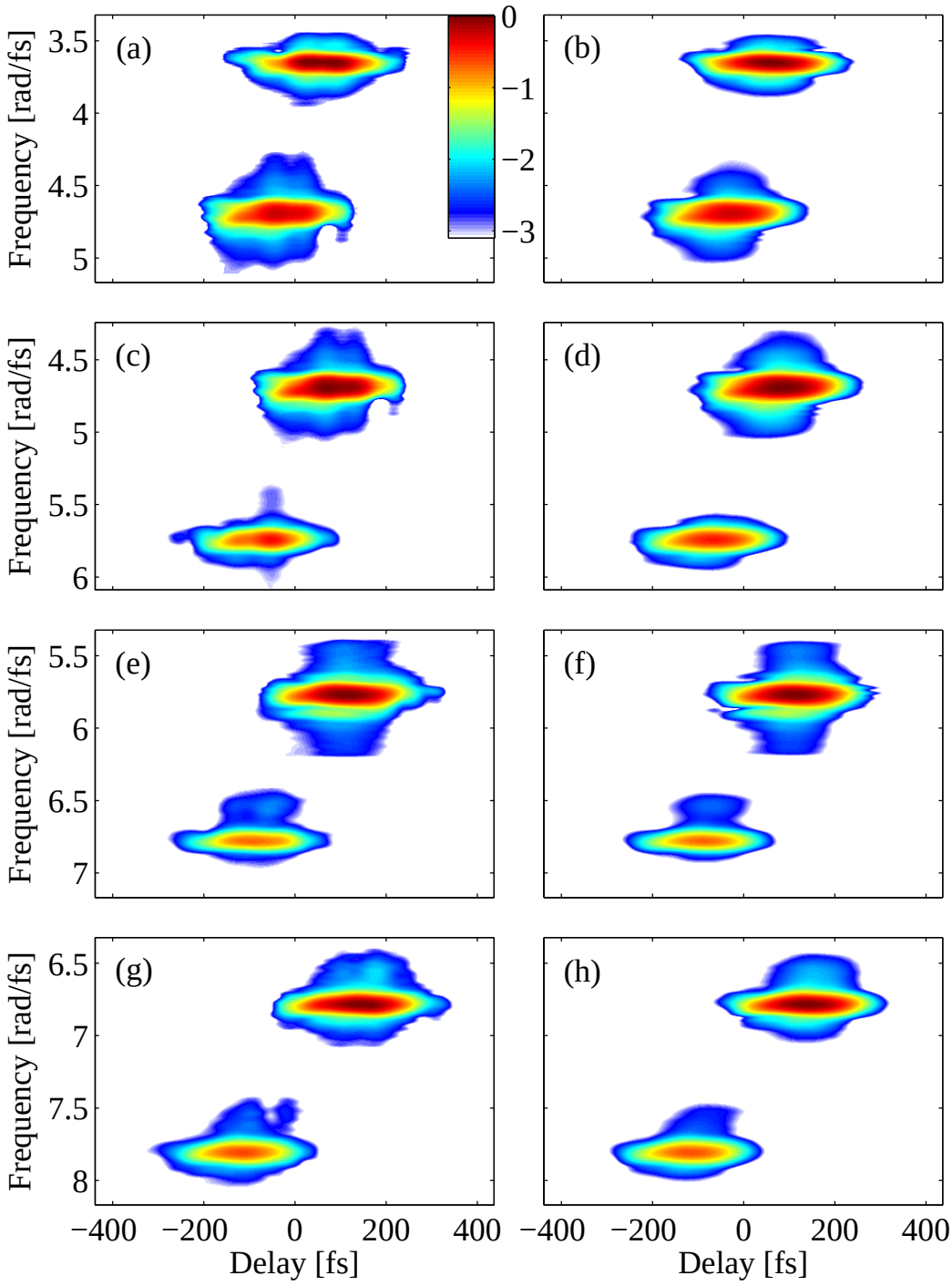

Figure 4.10: XFROG Data with 3mm LiF output window: H5/7 + H2 (a) experimental and (b) retrieved, H7/9 + H2 (c) experimental and (d) retrieved, H9/11 + H2 (e) experimental and (f) retrieved, H11/13 + H2 (g) experimental and (h) retrieved.

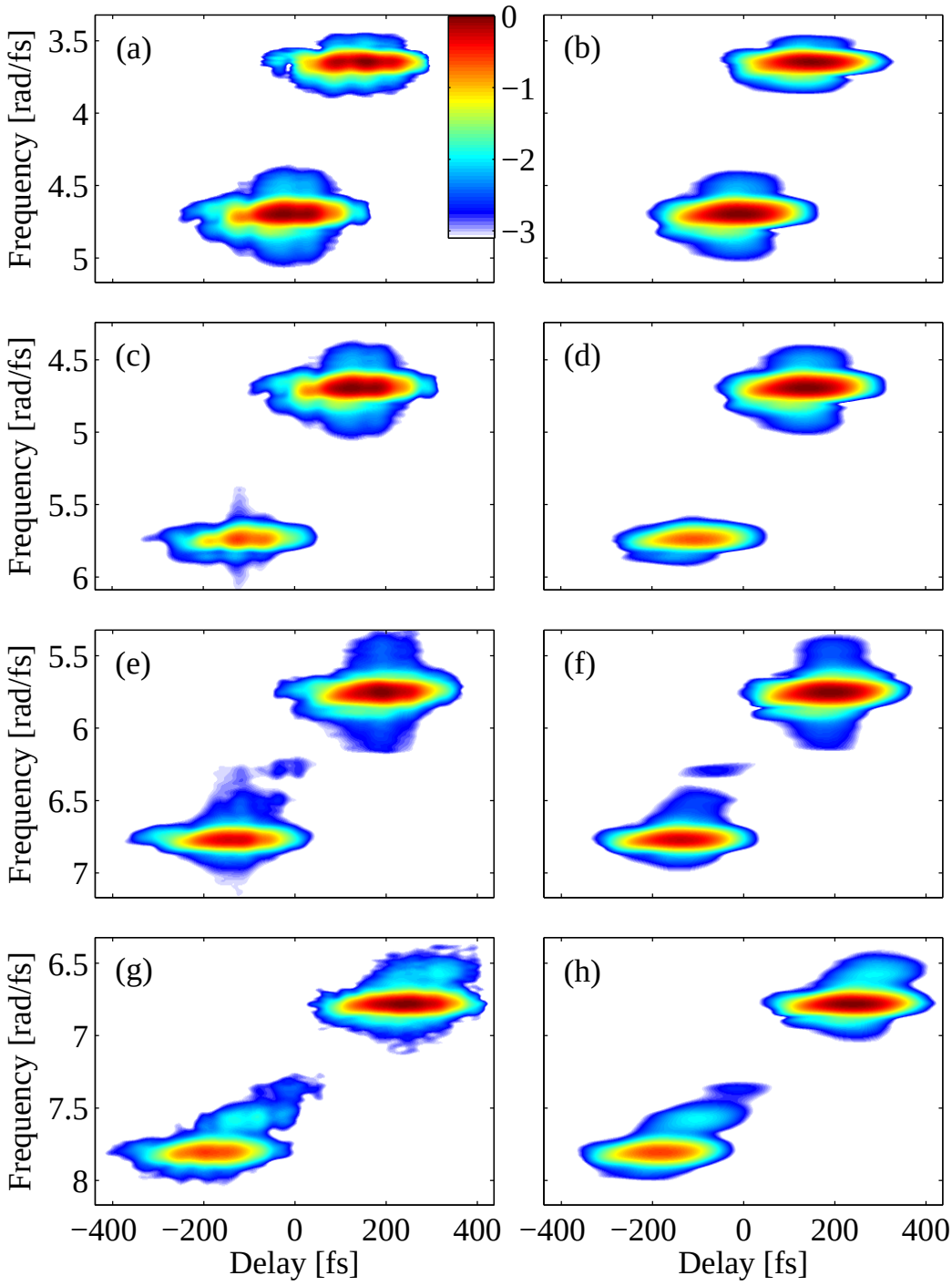

Figure 4.11: XFROG Data with 5mm LiF output window: H5/7 + H2 (a) experimental and (b) retrieved, H7/9 + H2 (c) experimental and (d) retrieved, H9/11 + H2 (e) experimental and (f) retrieved, H11/13 + H2 (g) experimental and (h) retrieved.

create the scan used in PCGPA retrieval.

After preparing all FROG traces in the data set, the double-constraint PCGPA algorithm described in Sec. 4.1.5 was used to retrieve the harmonics and 1.8μm gate pulse. Fig. 4.9 shows the measured and retrieved XFROG traces using the 2mm LiF output window, Fig. 4.10 shows the measured and retrieved traces using the 3mm LiF window, and Fig. 4.11 shows the measured and retrieved traces using the combined 2mm+3mm LiF window. Each trace has a grid size of 1024x1024, and parallel processing of all 12 traces was run for 5000 iterations, requiring 1.5 days to complete.

In order to quantify the accuracy of the retrieved FROG traces, the FROG error G is defined as [104, 137]

$$G = \left[\frac{1}{N^2}\sum_{i=1}^{N}\sum_{j=1}^{N}\left(I_{meas}(\omega_i,\tau_j) - \mu I_{ret}(\omega_i,\tau_j)\right)^2\right]^{\frac{1}{2}} \tag{4.26}$$

where $I_{meas}(\omega,\tau)$ and $I_{ret}(\omega,\tau)$ are the measured and retrieved FROG traces, respectively, and μ is a scalar value that minimizes G. The FROG error is a slight modification to the standard RMS error; the scalar factor μ is included to account for the presence of noise in the experimental data. Since both traces are normalized to a peak value of 1 before computing the FROG error, any noise present in the experimental trace may alter the peak value of the experimental trace when compared with its peak value if no noise were present. Consequently, the measured and retrieved FROG traces may require some other scaling in order to best compare the two traces. μ is computed using a linear search routine after PCGPA processing is completed, and typically takes values within 1-2% of unity. For a 128 x 128 grid size, a FROG error 0.005 or less is widely accepted as indicative of an accurate retrieval of a low-noise trace. The FROG error scales as $N^{-1/2}$, thus for the 1024 x 1024 grid size used in this experiment, the target FROG error is 0.001768. Table 4.4 lists the

LiF window thickness	H5/7 + H2	H7/9 + H2	H9/11 + H2	H11/13 + H2
2mm	1.310E-3	8.53E-4	7.83E-4	1.146E-3
3mm	2.009E-3	1.653E-3	7.41E-4	1.207E-3
5mm	2.727E-3	1.784E-3	1.328E-3	8.65E-4

Table 4.4: FROG Error G for each FROG trace

FROG errors for each of the 12 retrieved XFROG traces.

Of the 12 traces processed, only three failed to meet the target FROG error, and of these three the H7/9 trace with 5mm output window has an error that is only minimally higher than the target threshold and is close enough to declare a converged result. The two FROG traces with larger FROG errors are still within a factor of two of the target, however in a conservative approach these traces must be excluded from further analysis. Conveniently, both problem traces are H5/7 + H2 traces, which means that only the computed pulse parameters for the 5^{th} harmonic are suspect, and the computed delays between harmonics 7-13 remain valid. Examination of Fig. 4.10(a) and Fig. 4.11(a) clearly show that the experimental XFROG traces for the 5^{th} harmonic are corrupted by noise on the 10fs time scale. The most likely source for this noise is variation in the Cs conditions at the column boundary; the 5^{th} harmonic experiences anomalous dispersion in Cs due to the pressure-broadened D_2 line [138]. Additionally, Cs dimers exhibit strong absorption resonances quite close to the 5^{th} harmonic wavelength [139]; even a small concentration of dimers in the vapor column can cause non-negligible changes to the observed group index, spectral content, and temporal pulse envelope. Consequently, the observed 5^{th} harmonic group delay is highly sensitive to small fluctuations in either Cs column length or density. Since the environment near the Cs column boundary is highly turbulent, it comes as little surprise that difficulties are encountered when attempting to collect an XFROG scan for the 5^{th} harmonic over a time scale of 10s of minutes.

4.2.1 Error Analysis

For any reconstructed pulse parameters, it is important to find a reasonable method for computing error bars on the results. As with all other FROG schemes, placing error bars on the recovered pulses is non-intuitive. Attempts can always be made to think through every possible source of error, calculate the expected error from these sources, and then perform a root-sum-square calculation to arrive at a final value. This method is highly subjective, however, and always leaves open the possibility of excluding a significant source of error by simple oversight. Fortunately, we can take advantage of the over-complete nature of the FROG spectrogram to more conclusively place bounds on the retrieved pulses. Since the FROG trace contains more information than is necessary to completely describe both the gate and probe, it is possible to take a random sub-sample of the FROG trace, run the PCGPA algorithm on it, and compare the pulses extracted from the results to the pulses retrieved after running PCGPA on the full FROG trace. Repeat the random sub-sampling hundreds of times and treat the resulting data set statistically, and error bars can be computed and placed on the retrieved pulses without any subjective decision-making or estimation.

This method, called the bootstrap technique [140, 141], is performed as follows: for an NxN FROG trace, create a vector r of length N^2 and fill it with random values in the range $[1, N^2]$. Create a new FROG trace $I_{bootstrap}(\omega, \tau)$ filled with zeros. Using linear indexing into the array, populate $I_{bootstrap}$ from the measured FROG trace $I_{meas}(\omega, \tau)$ as $I_{bootstrap}[r] = I_{meas}[r]$. Since each value in r may be identical to one or more other values in r, the resulting sub-sampled FROG trace contains $\sim 67\%$ of the non-zero data points. The PCGPA algorithm is then run on $I_{bootstrap}(\omega, \tau)$, and the resulting gate and probe fields are saved. 100 or more sub-sampled FROG traces are

created, and after PCGPA processing statistics on all desired pulse characteristics can be computed using the resulting set of solutions for the probe and gate fields. Fig. 4.12 shows an example of an XFROG trace before and after sub-sampling.

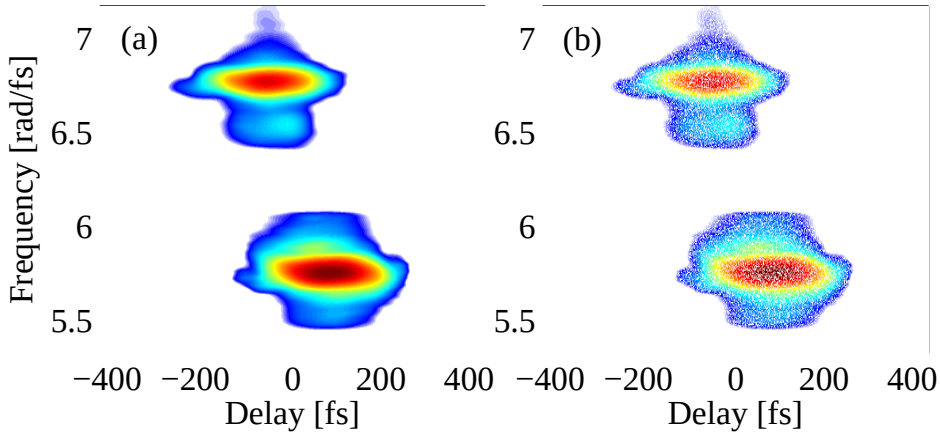

Figure 4.12: Bootstrap example: (a) H9/11 + H2 XFROG taken from Fig. 4.9(e) and (b) sub-sampled trace ready for PCGPA processing.

Since we are uninterested, for the most part, in the spectral or temporal properties of the 1.8μm gate, a modification was added to the bootstrap technique. Rather than process the sub-sampled traces using the constraint introduced to ensure self-consistency of the data across XFROG traces, the gate was held constant using the gate retrieved from the PCGPA processing of the full data set. Holding the gate constant across PCGPA iterations allows for the de-coupling of the XFROG traces; it no longer remains necessary to process the traces in parallel. Accordingly, each XFROG trace was sub-sampled 500 times, and the 6000 resulting traces along with the constant gate were submitted to the University of Michigan Center for Advanced Computing grid for processing. In order to compute error bars for the 1.8μm pulse, the reverse was done: the retrieved probes from all 12 XFROG traces were held constant, and parallel processing with gate averaging was performed on 500 sets of sub-sampled XFROG traces, where each set contained randomly sub-sampled

versions of the original 12 XFROG traces. Fig. 4.13 shows the retrieved 1.8μm gate. The total time taken to complete the processing necessary for bootstrap procedure

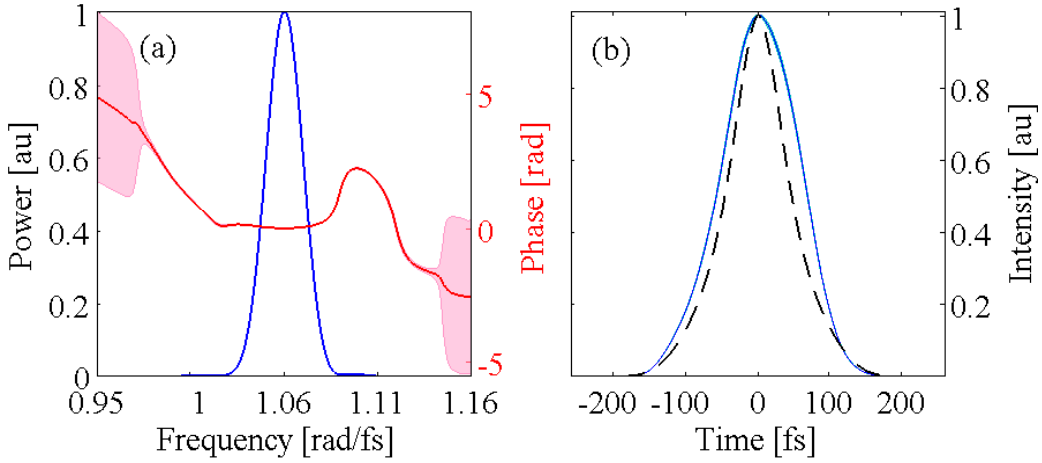

Figure 4.13: Retrieved Second Harmonic. (a) Spectral Power and Phase: $\omega_0 = 1.0558 \pm .0001$rad/fs, $\Delta\omega = 0.0248 \pm 0.0001$rad/fs. (b) Time-domain Intensity Profile: recovered (blue, solid), transform limit (black, dashed). $\tau = 125.84 \pm 0.92$fs. Transform limit $\tau = 92.22$fs. Error bars are represented by the shaded regions.

calculations of pulse statistics was 2 weeks, however if run on a single computer the total processing time would be in excess of 2 years.

4.2.2 Results Analysis

After completing all computations required by the bootstrap method, the relative delay between two adjacent harmonic orders i, j measured through output window x is computed as follows: Fourier transform the retrieved time-domain probe field, extract and unwrap the spectral phase $\phi(\omega)$, and compute the delay between pulse i and pulse j as

$$\tau^{(x)}\Big|_i^j = \frac{\mathrm{d}\phi(\omega)}{\mathrm{d}\omega}\bigg|_{\omega_j} - \frac{\mathrm{d}\phi(\omega)}{\mathrm{d}\omega}\bigg|_{\omega_i} \tag{4.27}$$

The resulting relative delays $\tau^{(x)}\big|_i^j$ are then concatenated according to Eq. 4.10 to create $\mathrm{d}\phi(\omega)/\mathrm{d}\omega$ across the entire measured harmonics spectrum. Fig. 4.14 shows the results of this calculation of $\mathrm{d}\phi(\omega)/\mathrm{d}\omega$ for all three output window configurations,

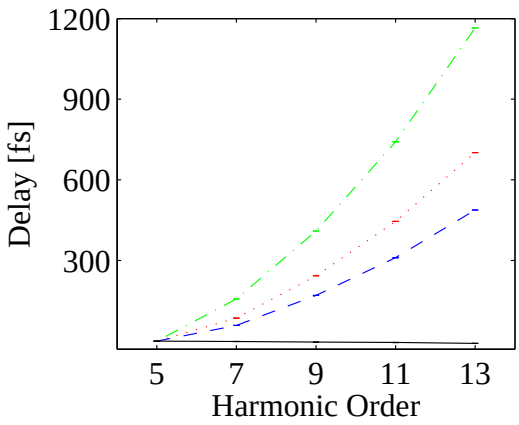

Figure 4.14: $\mathrm{d}\phi(\omega)/\mathrm{d}\omega$ for the 2mm LiF window (blue, dashed), 3mm window (red, dotted), and 5mm window (green, dash-dot). The extracted $\mathrm{d}\phi(\omega)/\mathrm{d}\omega$ with LiF contributions removed according to Eq. 4.19 is also shown (black, solid). Error bars are present, but difficult to see on this time scale.

along with the window-free delay computed using Eq. 4.19. A quick comparison with Fig. 4.5 shows the dramatic improvement achieved by the addition of the vacuum system to the experiment. To compute the error bars for the value of $\mathrm{d}\phi(\omega)/\mathrm{d}\omega$ at a particular harmonic order q, a root-sum-squares method was used:

$$\Delta\tau_q = \sqrt{\Delta\tau_{2\text{mm LiF},q} + \Delta\tau_{3\text{mm LiF},q} + \Delta\tau_{5\text{mm LiF},q}} \tag{4.28}$$

The recovered $\mathrm{d}\phi(\omega)/\mathrm{d}\omega$ is shown on a more appropriate time scale in Fig. 4.15. Note the negative dispersion, indicative of long trajectory dominance in the picture given by the SFA. The presence of a relative delay between harmonic orders is a strong indicator that the mechanism responsible for the generation of the observed harmonics is non-perturbative. Perturbation theory predicts that all harmonics are emitted in phase, and all attempts to attribute the observed slope to the dispersion of Cs failed using a simple Sellmeier model for Cs at 20Torr and a range of Cs column lengths about a best-guess estimate for the distance between the Cs-Ar boundary and the phase matching region where harmonics are generated.

Examination of Table 4.4 shows that on the whole, the data set acquired with

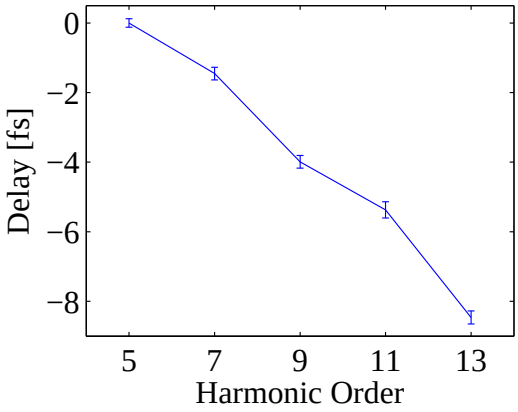

Figure 4.15: Extracted group delay using Eq. 4.19. This represents $\mathrm{d}\phi(\omega)/\mathrm{d}\omega$ after harmonic generation and propagation through the remainder of the Cs column and Ar buffer.

the 2mm LiF output window reached the best convergence in terms of FROG error values. Thus, the recovered harmonics probes from the 2mm LiF data set are the most desirable for use in reconstruction of the total spectrum, phase, and time-domain intensity. The spectral phase contribution of the 2mm LiF window to the total spectral phase of a given harmonic q is calculated by applying Eq. 4.16 to the measured $\mathrm{d}\phi(\omega)/\mathrm{d}\omega$ and performing a polynomial projection about the carrier frequency ω_q, discarding the linear and DC terms. Fig. 4.16 shows the retrieved spectral power and phase from the 2mm LiF window data set for each harmonic order; also shown is the LiF contribution to the spectral phase, the calculated actual spectral phases in the absence of the LiF window, and the time-domain intensity profiles. Table 4.5 lists relevant parameters for the individual harmonic orders.

Harmonic Order	5	7	9	11	13
ω_0 [rad/fs]	2.6036 ± 0.0013	3.6334 ± 0.0056	4.703 ± 0.0036	5.7208 ± 0.0032	6.744 ± 0.0034
$\Delta\omega$ [rad/fs]	0.0638 ± 0.0006	0.0908 ± 0.0007	0.0829 ± 0.0007	0.0702 ± 0.0006	0.0806 ± 0.0006
$\Delta\omega/\omega_0$	0.0245 ± 0.0002	0.025 ± 0.0002	0.0176 ± 0.0001	0.0123 ± 0.0001	0.012 ± 0.0001
τ [fs]	51.46 ± 0.44	41.75 ± 0.67	40.33 ± 0.37	48.13 ± 0.37	45.97 ± 0.36
$\tau_{\text{trans. lim.}}$ [fs]	50.46 ± 0.42	32.09 ± 0.29	37.17 ± 0.3	45.01 ± 0.36	38.43 ± 0.3
TBP	0.5228 ± 0.0184	0.6035 ± 0.0288	0.532 ± 0.0182	0.5378 ± 0.0179	0.5899 ± 0.0186
$\text{TBP}_{\text{trans. lim.}}$	0.5127 ± 0.0178	0.4639 ± 0.0156	0.4903 ± 0.0157	0.503 ± 0.0171	0.4931 ± 0.0157

Table 4.5: Reconstructed harmonics statistics. TBP = Time-bandwidth product.

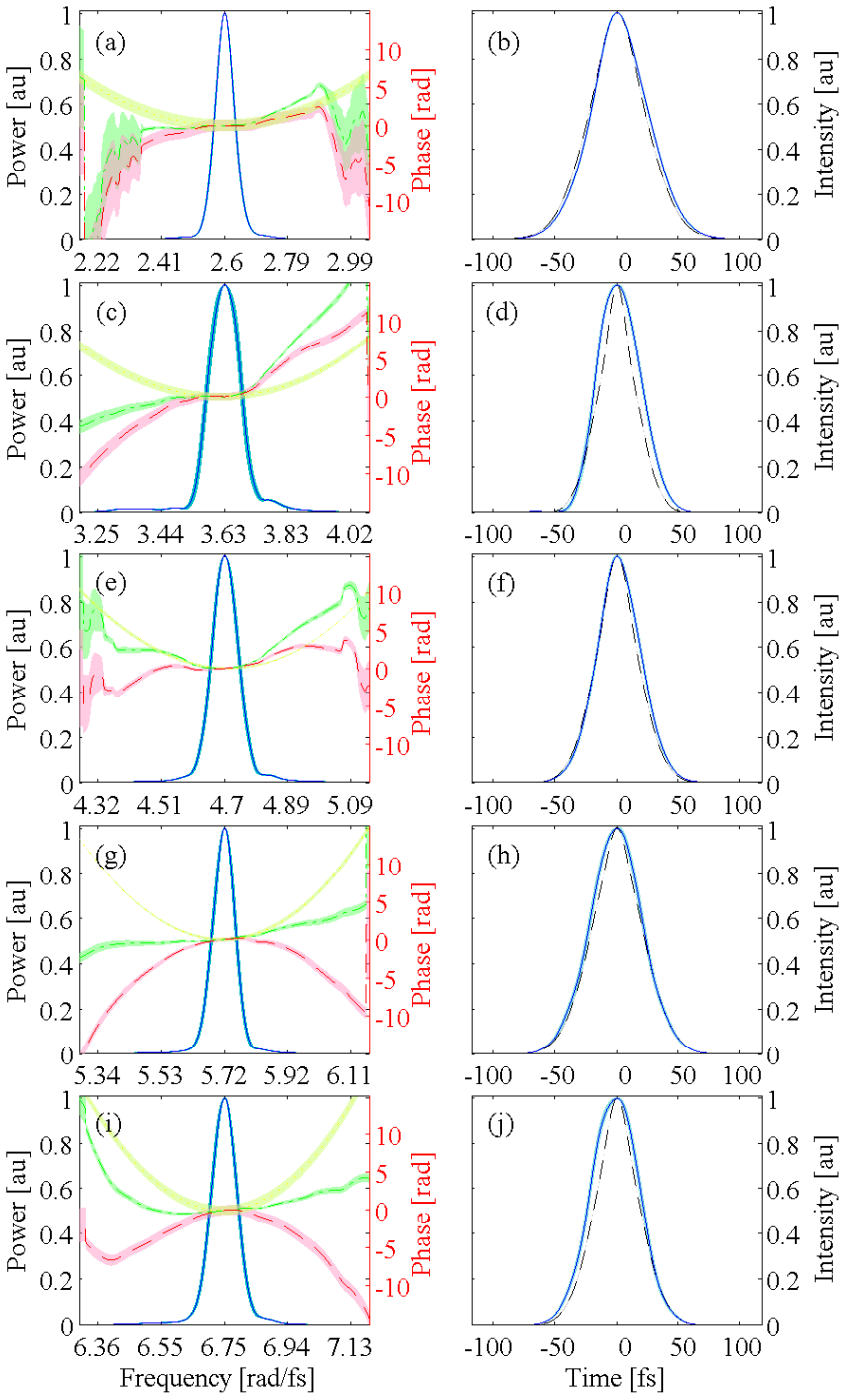

Figure 4.16: Reconstructed Harmonics. Left column–spectral power (blue, solid), phase (green, dash-dot), recovered 2mm LiF phase contribution (yellow, dotted), and phase with LiF contribution removed (red, dashed). Right column–time-domain intensity profile (blue, solid) and transform-limited profile (black, dashed). Error bars are represented by the shaded regions. (a) & (b): 5^{th} harmonic. (c) & (d): 7^{th} harmonic. (e) & (f): 9^{th} harmonic. (g) & (h): 11^{th} harmonic. (i) & (j): 13^{th} harmonic.

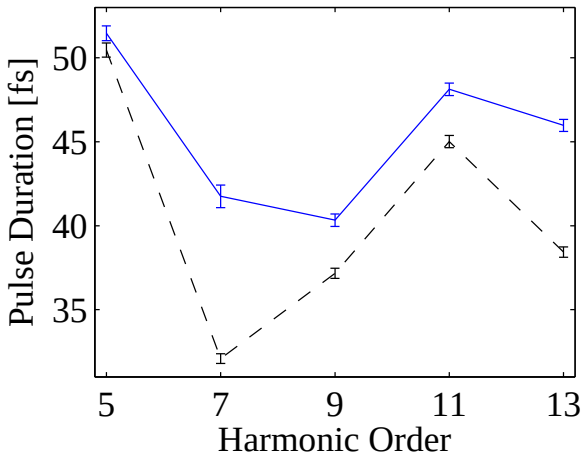

Figure 4.17: Pulse duration vs. harmonic order with LiF spectral phase contribution removed (blue, solid), and transform limited (black, dashed).

Shown in Fig. 4.17 is the pulse duration vs. harmonic order. Clearly, the pulse duration does not follow the perturbative scaling law $\tau_q = \tau_{3.6\mu\mathrm{m}}/\sqrt{q}$, although this in itself is not a conclusive argument against a perturbative source being responsible for the harmonic production. Since the macroscopic dispersion properties of the Cs are un-accounted for in this experiment, there may be some difference in the pulse duration at the location of harmonic generation and the measured duration. Regardless, the transform limited pulse duration also fails to scale as $\tau_q = \tau_{3.6\mu\mathrm{m}}/\sqrt{q}$, which makes it nearly inconceivable that such a scaling applies at the tail end of the phase matching region unless the Cs column is significantly re-shaping the spectrum of all harmonic orders. Such a re-shaping would most likely be caused by absorption; prior published measurements of the Cs I and Cs-Cs dimer absorption resonances indicate that only the 5^{th} harmonic should be subject to strong enough absorption to significantly modify its spectral power.

Fig. 4.18 and Fig. 4.19 show that bandwidth and time-bandwidth product for the recovered harmonics, respectively. The transform-limited values for the time-bandwidth product are quite close to the 0.44 value expected for a Gaussian pulse.

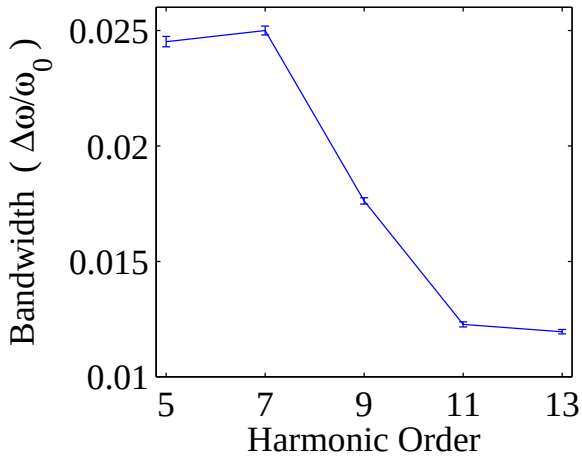

Figure 4.18: Fractional bandwidth vs. harmonic order.

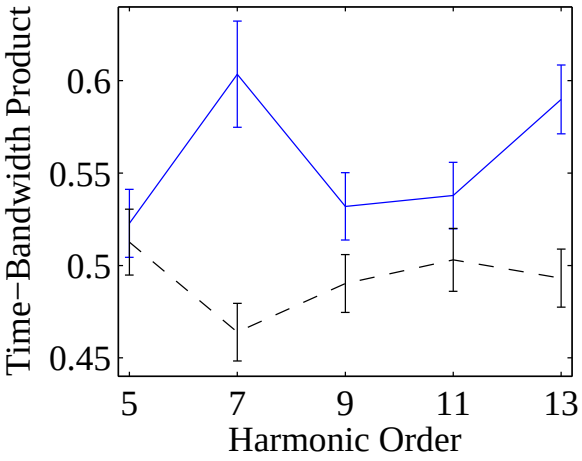

Figure 4.19: Time-bandwidth product vs. harmonic order (blue, solid), and transform-limited time-bandwidth product (black, dashed).

Fig. 4.20 shows the spectral power and phase for all recovered harmonic orders. The relative heights of the harmonics' spectral power were scaled using an independently measured harmonics spectrum and using manufacturer-supplied data to correct for all of the aluminum mirror reflections, spectrometer grating diffraction efficiency, MCP intensifier response, and LiF transmittance. The relative spectral phase between harmonic orders at their carrier frequencies is dictated by the integral of the measured $\mathrm{d}\phi(\omega)/\mathrm{d}\omega$, and a linear slope equal to $\mathrm{d}\phi(\omega)/\mathrm{d}\omega\big|_{\omega_q}$ is assigned to

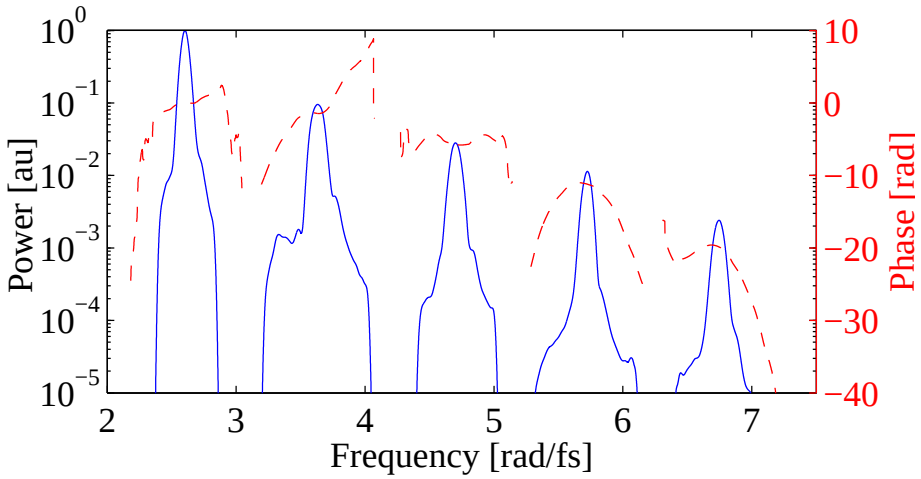

Figure 4.20: Total spectral power and phase for harmonic orders 5-13.

the spectral phase of each harmonic order q. The time-domain reconstruction using all recovered harmonics is shown in Fig. 4.21.

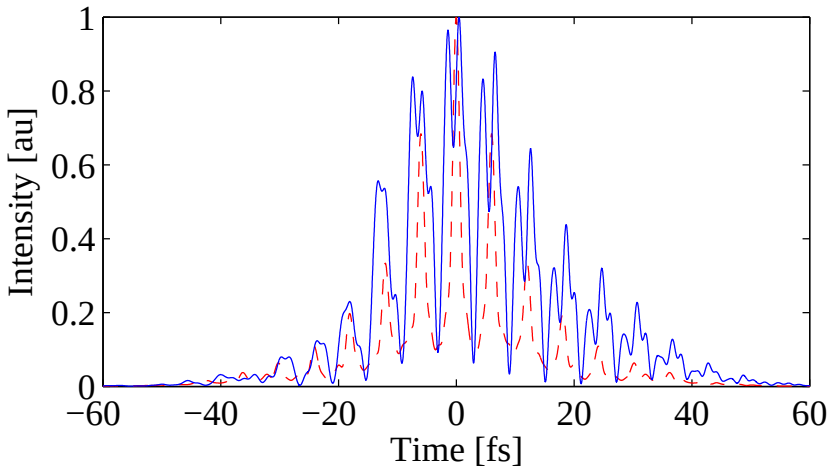

Figure 4.21: Time-domain intensity profile after synthesizing all recovered harmonics (blue, solid) and transform limit(red, dashed). The FWHM duration of the most intense burst is $\tau = 4.39$fs, with a transform limited value of $\tau = 1.52$fs.

Since the recovered 5^{th} harmonic is suspect due to the failure to converge of two of the three XFROG traces involving the 5^{th} harmonic, Fig. 4.21 may not be the most accurate representation. If, due to the high noise level and subsequent poor convergence of the 5^{th} harmonic XFROG traces, the extracted delay between the 5^{th} harmonic and the 7^{th} harmonic is off by even 1fs, the reconstructed intensity

profile changes dramatically. Consequently, it becomes necessary to exclude the 5^{th} harmonic from the time-domain reconstruction. A more meaningful time-domain reconstruction involving only harmonics 7-13 is shown in Fig. 4.22. While the intensity profile of the pulse train synthesized from harmonics 7-13 shows significant structure due to the negatively chirped spectral phase, in theory it should be possible to further compress the spikes in the pulse train by adding an appropriate amount of positively dispersive material such as a higher pressure column of Ar or by extending the length of the existing Ar column serving as the Cs buffer gas.

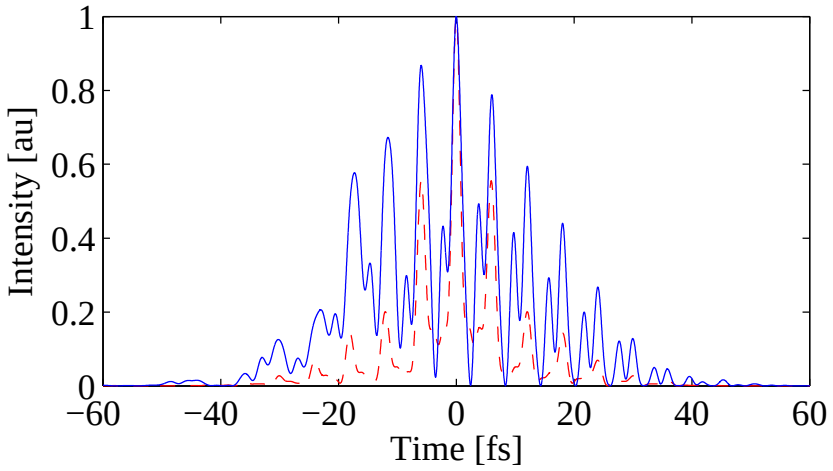

Figure 4.22: Time-domain intensity profile after synthesizing harmonics 7-13 (blue, solid) and transform limit(red, dashed). The FWHM duration of the most intense burst is $\tau = 2.03$fs, with a transform limited value of $\tau = 1.68$fs.

4.2.3 Auxiliary Results

While the presence of a non-zero $\mathrm{d}\phi(\omega)/\mathrm{d}\omega$ and the non-perturbative scaling of harmonic pulse duration with harmonic order are strong indicators that the harmonics are generated via strong-field interactions, this evidence alone is insufficient to prove such an assertion. Additional evidence exists, however, that further strengthens the argument that the harmonics are non-perturbative, and therefore are created through the strong-field HHG process.

Fig. 4.23 shows a measurement of the relative harmonic yield vs. driving intensity. In the perturbative limit, the measured harmonic energy at harmonic order q should scale as $U_q \propto I^q$. This measurement was performed by adjusting the laser pulse energy using a $\lambda/2$ waveplate and polarizer immediately before the focusing lens and at a Cs pressure of $\sim$ 60Torr. Plotted on a linear scale, the harmonic yield

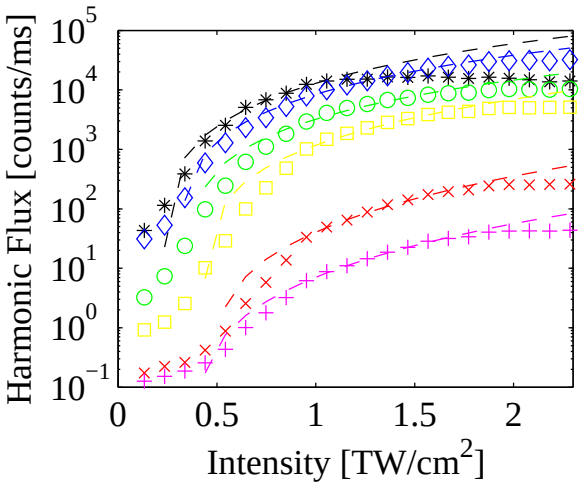

Figure 4.23: Intensity dependence of harmonic yield. H5 (black, star), H7 (blue, diamond), H9 (green, circle), H11 (yellow, square), H13 (red, X), and H15 (magenta, plus). Best-fit power-law scalings for each harmonic order are shown in dashed lines. Fitting was only performed for data points below the observed saturation of harmonic yield.

at each order was observed to saturate at intensities ranging from 1.2-1.6 TW/cm^2. Power-law fits were computed for each yield vs. intensity curve, using only the data below the observed saturation. Table 4.6 shows the resulting fitted power parameter: harmonics below I_p (5-11) scale as roughly I^2, while the harmonic orders above I_p scale roughly as I^3.

Harmonic Order q	x_q
5	2.161
7	2.076
9	2.034
11	2.397
13	2.971
15	2.897

Table 4.6: x_q from best-fit modeling of the harmonic yield vs. intensity using the power-law model $U_q = a_q I^{x_q}$.

A 1-D TDSE calculation [51] was also performed using a $\tau = 87.5$fs (FWHM) pulse at $I = 9 \times 10^{11}$W/cm^2, and the resulting induced dipole moment is shown in Fig. 4.24. The harmonics spectrum calculated from the induced dipole is shown

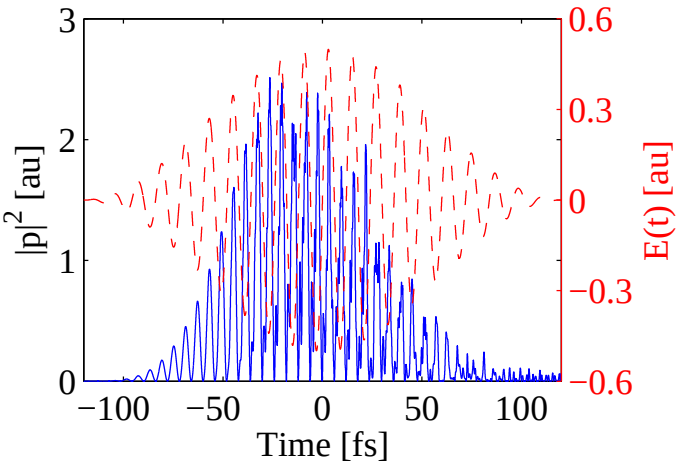

Figure 4.24: Dipole moment from a 1-D TDSE calculation (blue, solid), and 3.6μm electric field (red, dashed).

in Fig. 4.25 along with the experimentally measured power spectrum. Fitting the harmonics power as a function of ω shows that the experimentally measured harmonics decrease as $\omega^{-4.30}$ between harmonic orders 7 - 13, while the TDSE-calculated harmonics decrease as $\omega^{-4.03}$ over the same range.

The scaling of harmonic yield vs. ω is quite similar to experimental results, although some difficulty arises in attempting to obtain an exact match, since the relative harmonic spectral powers have been experimentally observed to depend strongly on phase-matching conditions, and can change dramatically with small changes in I, spot size, and focal plane location within the Cs column.

A time-frequency analysis [142] was performed on the TDSE results, and the extracted harmonic emission times were then used to compute $\mathrm{d}\phi(\omega)/\mathrm{d}\omega$. The results of this analysis are shown in Fig. 4.26, and show negative dispersion akin to experimental observations (Fig. 4.15). The factor of ~ 4 difference in the total delay

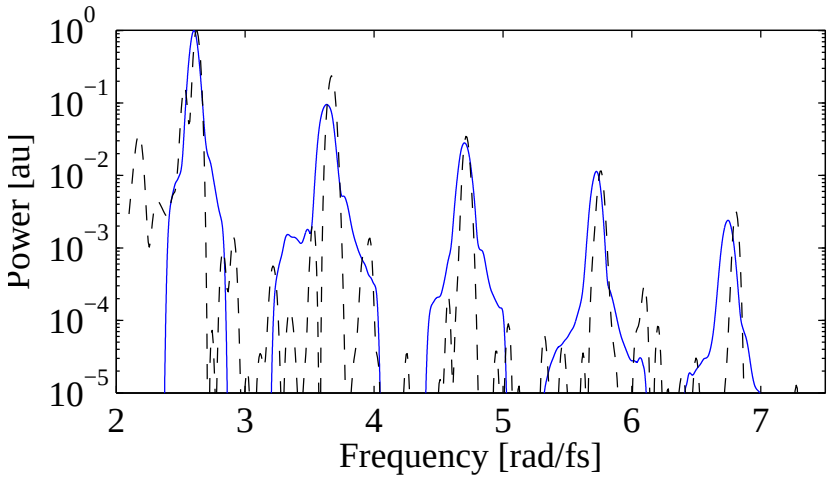

Figure 4.25: Radiated harmonics spectrum from the 1-D TDSE calculation (black, dashed) and measured power spectrum (blue, solid).

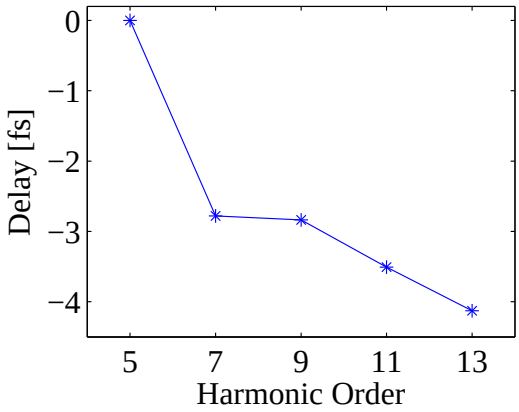

Figure 4.26: $\mathrm{d}\phi(\omega)/\mathrm{d}\omega$ extracted from a time-frequency analysis of the 1-D TDSE results.

between harmonic orders 7 and 13 may be in large part due to the macroscopic propagation effects of Cs. Further experiments are necessary to determine the exact length and density profile of the Cs column, and to discover the length and location of the zone within the Cs column over which harmonic production is phase-matched.

The existence of an non-zero $\mathrm{d}\phi(\omega)/\mathrm{d}\omega$, the lack of perturbative scaling for the harmonic energy yield vs. I or pulse duration vs. q, and the reasonable agreement between experiment and 1-D single atom calculations all speak heavily in favor of strong-field interactions being the physics underlying the generation of the observed

harmonics. Presuming strong-field HHG, the measured negative dispersion on the spectral phase indicates that the long trajectory was dominant in the production of the observed harmonics. It should be noted that one major difference exists between the presented TDSE calculation and experimental results. The TDSE calculation used $\gamma = 1.34$, while the experimental value was $\gamma = 0.78$. This difference must play a part in the slight mismatch between the calculated and observed $\mathrm{d}\phi(\omega)/\mathrm{d}\omega$, since the higher experimental intensity modifies the intensity-dependent phase.

CHAPTER V

Conclusions and Future Work

The bulk of this dissertation concerns the development of two novel time-domain measurement techniques targeted towards characterizing transient UV-VIS-NIR radiation on the few-hundred attosecond to few femtosecond time scales using solid-state nonlinearities. The extremely short nature of the pulses involved mandates that the adopted measurement schemes be free from all sources of dispersion or capable of accurately characterizing any unavoidable dispersion for later removal from the data. In a diversion from this exotic metrology, experimental observations of the generation of high energy few-cycle pulses through self-phase modulation during filamentary propagation in a self-compression regime are presented.

5.1 All-Reflective Split Mirror Autocorrelator for In-situ Measurement of Ultra-broadband Pulses

Motivated by potential high energy, attosecond timescale bursts created through relativistic laser-plasma interactions [18], an all-reflective split mirror autocorrelator designed for in-situ measurement of both the pulse spectrum and 2^{nd}-order autocorrelation was built and tested [72]. The major improvement of this scheme versus previous dispersion-free split mirror designs [29, 30, 31] is the realization that a pinhole spatial filter placed in the detection plane can dramatically improve the non-

linear IAC fringe contrast, enables the collection of linear autocorrelation (and hence the pulse spectrum), and significantly eases the computational requirements on the functional minimization routine used to reconstruct the pulse. For the target application, the ability to use a single device to quickly measure both the spectrum (linear IAC) and nonlinear IAC is paramount. The relativistic deflection that angularly isolates attosecond pulses is strongly dependent on the carrier-envelope phase (CEP) of the laser. Changes to the CEP result in changes in deflection angle and will cause the pulses under test to clip or entirely miss the entrance apertures for the employed measurement system. The current state of CEP stabilization technology can reliably lock the CEP to a fixed value for tens of minutes, at best. By simply motorizing the mount for the photodiode, a swap from linear to nonlinear detector can be accomplished in seconds. A single autocorrelation can be acquired in ~ 30 seconds. Thus, with good quality CEP control this autocorrelator allows for the collection of several linear and nonlinear autocorrelation traces without the need for any form of dispersion compensation.

Autocorrelation functions for this device were presented and shown to be conceptually equivalent to the autocorrelation functions for a whole-beam interferometer [21, 22], with the only difference being the inclusion of integrals over the spatial dimensions of the pinhole. The computational power required to compute the 2^{nd}-order IAC on each iteration of a phase retrieval algorithm was reduced by more than one order of magnitude by taking advantage of observed symmetries in the autocorrelation function to create an approximate expression for the 2^{nd}-order response. For geometries where $r/\mathrm{w}_0(\omega_h) < 0.1$, where r is the pinhole radius and $\mathrm{w}_0(\omega_h)$ is the beam waist at the largest significant frequency in the pulse it was shown that the use of the approximated autocorrelation function does not appreciably add to the

reconstruction error, provided that the autocorrelation function is sampled at 5 or more points within r. A multi-threaded adaptive genetic algorithm adapted from an earlier adaptive GA designed for coherent control applications [79] was implemented as the functional minimization routine for reconstructing the pulse from split-mirror IAC data. This algorithm was shown to provide good computational performance as measured by total time necessary to reach convergence.

Experimental results were presented and shown to provide reasonable agreement with a SPIDER [25] measurement, with a figure of merit for the autocorrelation retrieval of $\Delta = 0.0036$, very close to the target for a whole-beam IAC of $\Delta \leq 0.003$. It remains to be shown, however, that this device can be used in its designed application. At the time this work was completed, lasers producing pulses with the necessary parameters ($U > 750\mu$J, $\tau = 5$fs, contrast $> 10^{-8}$) were not available to directly test the particle-in-cell predictions of relativistically generated attosecond pulses. It still remains, then, to develop the necessary laser source and target system such that this autocorrelator can be put to its designed use. Further work is also necessary to characterize the nonlinear response of existing large-bandgap detectors to determine their suitability for use in measuring attosecond pulses with multi-octave spectra.

5.2 Spectral Broadening and Self-Compression at 800nm and 2μm via Filamentary Propagation

The search for methods by which high energy, few-cycle laser pulses can be produced motivated the studies presented on self-compression of pulses with SPM-broadened spectra emerging from regions of filamentary propagation at both $\lambda_0 =$ 800nm [73] and $\lambda_0 = 2\mu$m [74]. For this work, self-compression is defined as a flat or negative GDD profile on the measured spectral phase profile, allowing for

re-compression (if necessary) using simple bulk glass. Filamentary propagation is a balance between the $\chi^{(3)}$-induced self-focusing and self-phase modulation, ionization, diffraction, and plasma de-focusing. Upon reaching a delicate balance between these often competing processes, a pulse becomes trapped in its own self-generated channel and can propagate many Rayleigh lengths without appreciable change in beam diameter, experiencing significant spectral and temporal re-shaping during the process. The processes involved in filamentary propagation are still a very active area of research, and more work is needed to fully explain the experimentally observed negative GDD at 800nm [85]. In all cases where self-compression was observed, plasma fluorescence imaging of the filament showed two or more nonlinear focusing cycles.

For the 800nm studies, a short pulse SPIDER observed negative GDD for all self-compressed pulses, usually of the order of -200fs^2. Self-compression at 800nm was observed in Ar, Kr, Xe, and even N_2; in this last case 5 nonlinear foci were observed, and the total filament length exceeded 70cm. Experimental results show that for self-compression at 800nm the ratio if input power to the critical power for self focusing must be $P_{in}/P_{crit} > 3$. Self-compression in Ar was shown at a variety of pressures, with an optimal pressure found at 870mbar. Circularly polarized light was also tested in Ar and showed similar results to the linearly polarized case, with the exception that the divergence of the beam exiting the filament increased by a factor of ~ 2 when using circularly polarized light. Among the gases tried, Xe has the largest nonlinear index of refraction n_2 and showed the most spectral broadening; the spectrum emerging from the filament in Xe supports a pulse duration < 5fs. However, the very low Xe critical power for self-focusing limits the ability to scale a Xe-based compression system to very high pulse energies. Additionally, phase-matching limitations of the SPIDER BBO crystal prevented an accurate reconstruction of the

spectral phase over the entire pulse spectrum–the shortest measured pulse was $\sim$ 12fs, although many of the collected spectra carried bandwidths supporting shorter pulses. The advantages to filamentary propagation for broadening the pulse spectrum over other techniques are significant: with proper choice of bulk media type and pressure, input mirror focal length, and input beam size, self-compressed pulses with sub-3-cycle duration and millijoules of energy should be possible [41].

Self-compressed pulses were also observed at $\lambda_0 = 2\mu$m for a variety of Xe pressures: 1.6bar, 1.87bar, 2.15bar, and 2.44bar. The diagnostic scheme for temporally characterizing these filament-compressed pulses was a Michelson interferometer with linear and nonlinear photodiode detectors: the most classic example of a whole-beam interferometric autocorrelator. For the 2.15bar and 2.44bar cases, reconstructions from the autocorrelation measurements show pulses with duration $\tau = 17.9$fs and $\tau = 13.6$fs, respectively. These $<$ 3-cycle pulses were observed to carry $\sim 54\%$ of the input pulse energy in a nearly transform-limited pulse spectrum. Since the difference-frequency optical parametric amplifier used to generate the 2μm light intrinsically locks the carrier-envelope phase to a fixed offset [91], it becomes interesting to examine if the CEP stability of the laser is maintained through the filament. f-to-$2f$ interferometry between the blue tail of the pulse spectrum and the frequency-doubled central portion of the spectrum show that the CEP drift is $<$ 0.1rad RMS over nearly 9000 consecutive pulses.

The availability of high energy, few cycle, long wavelength radiation will be of great benefit to future investigations into the long wavelength scaling behavior predicted for strong field processes (e.g. harmonic generation) [54]. Using such a source, attosecond pulse synthesis using photon energies $\gg$ 100eV should be possible. In order to further aid the development of a filament compression scheme for long-

wavelength sources, a strongly advised first step is to implement a real-time FROG or SPIDER capable of handling the extreme bandwidths involved, allowing for fine tuning of the Xe pressure, beam focusing, etc. to optimize the filament output for pulse duration, output energy, and spectral content.

5.3 Temporal Characterization of Scaled System Harmonics using Cross-Correlation Frequency Resolved Optical Gating

The Keldysh scaling model predicts that for laser-atom interactions where the adiabicity parameter γ is the same, the physics of the interaction should be quite similar. This gives rise to the scaled system concept, where a long-wavelength laser driving an atom with low I_p is the scaled version of a more conventional laser driving an atom with higher I_p. In this work the scaled system considered uses a 3.6μm laser driving processes in Cs at $\gamma \sim 1$, which is the scaled version of an 800nm laser with an Ar target at $\gamma \sim 1$. Conveniently, harmonic orders 3 - 19 of a 3.6μm laser lie below the VUV cutoff, giving rise to the possibility for using conventional solid-state nonlinearities for temporally characterizing these harmonics. A cross-correlation frequency resolved optical gating scheme designed to characterize harmonic orders 5 - 15 was designed and implemented. For Cs ($I_p = 3.89$eV) harmonic orders 5 - 11 all lie below I_p, providing a unique opportunity for time-resolved studies of harmonics on bound-bound transitions.

With great care taken to eliminate or ameliorate dispersion in the measurement system, the deployed XFROG was shown to be capable of resolving the relative temporal delay between harmonic orders to within $\pm$180as by using a combination of LiF windows on the output of the Cs heat pipe. XFROG results for harmonic orders 5 - 13 show negative dispersion, or a negative slope to the extracted $\mathrm{d}\phi(\omega)/\mathrm{d}\omega$, indicative of long-trajectory selection under the model given by the strong field approxima-

tion [62]. Furthermore, the negative chirp extracted for harmonic orders 11 and 13 is consistent with this finding; orders 5 - 9 show higher order phase contributions. The measured pulse duration for each harmonic order was shown to entirely fail to follow the perturbative scaling $\tau_q = \tau_{3.6\mu\mathrm{m}}/\sqrt{q}$, both for the reconstructed pulses and their transform limits. Ancillary measurements reveal that the harmonic yield vs. intensity also fail to follow the model given by perturbation theory, $U_q \propto I^q$. Instead, harmonic orders 5 - 9 scale as $\sim I^2$, while harmonic orders 11 and 13 scale as $\sim I^3$. Combined, the presence of a non-zero $\mathrm{d}\phi(\omega)/\mathrm{d}\omega$ and the failure of the harmonics to follow perturbative scaling laws for energy or pulse duration speaks strongly in favor of strong field processes being responsible for the generation of these harmonics. 1-D TDSE calculations show similar behavior to that observed in experiment: the scaling of harmonic power vs. ω is nearly identical, and both show negative $\mathrm{d}\phi(\omega)/\mathrm{d}\omega$ on the order of a few femtoseconds between harmonics 5 - 13. The difference in $\mathrm{d}\phi(\omega)/\mathrm{d}\omega$ between experiment and simulation may be due to macroscopic propagation effects; further experiment is necessary to determine if this is indeed true.

Having developed and proven this particular measurement technique, there are still many experiments to be conducted before conclusive statements can be made about the behavior of the 3.6μm Cs scaled system as compared to its 800nm Ar cousin. The first experiment to be conducted is to complete the window swapping procedure and characterize both LiF windows at harmonic order 15, which was not completed on previous experimental runs. Phase matching between harmonic order 15 and the 1.8μm gate has been demonstrated in air, but remains to be accomplished using the current vacuum-based design. After completing the measurements necessary for removal of the LiF contribution from the data, it is not necessary to apply the window swapping technique on future experimental runs, therefore subsequent

experiments should proceed with greater rapidity. The simplest and most important experiment to be conducted is to fix all experimental parameters at the settings used in the reported results and change only the Cs pressure. If the recovered $\mathrm{d}\phi(\omega)/\mathrm{d}\omega$ does not change, it can safely be assumed that propagation effects in Cs are unimportant and that the observed group delay is representative of the single-atom response. If $\mathrm{d}\phi(\omega)/\mathrm{d}\omega$ is observed to change, further experiments are necessary to attempt to quantify the exact amount of delay incurred by propagating through Cs. Foremost among these is to perform an absorption measurement to determine the exact length and density profile of the Cs column. Photoelectron spectra from Cs at $\gamma \sim 1$ would also help to confirm the strong field physics diagnosis for the observed harmonic generation.

Time-resolved studies of the scaled 3.6μm/Cs system are severely hampered by the high reactivity of Cs. The Cs densities required to achieve harmonics energies sufficient for measurement mandate the use of a spectroscopic heat pipe. Absent a differential pumping system to operate the heat pipe without an output window, a complicated and potentially dangerous setup, any measurement technique must be capable of accounting for the dispersion of the window. This XFROG employs a novel method of completely characterizing the dispersion of two unknown windows without any additional experimental setup by simply varying the output window configuration and acquiring repeated data sets. Using this scheme, the relative delay between harmonic orders 5 - 13 was measured, for the first time providing a view of the temporal properties of the harmonic generation process in the scaled system.

BIBLIOGRAPHY

BIBLIOGRAPHY

[1] A. L. Schawlow and C. H. Townes. Infrared and Optical Masers. *Phys. Rev.*, 112:1940–1949, 1958.

[2] T. H. Maiman. Stimulated Optical Radiation in Ruby. *Nature*, 187:493–494, 1960.

[3] F. J. McClung and R. W. Hellwarth. Giant Optical Pulsations from Ruby. *J. Appl. Phys.*, 33:828–829, 1962.

[4] W. E. Lamb. Theory of an Optical Maser. *Phys. Rev.*, 134:A1429–A1450, 1964.

[5] L. E. Hargrove, R. L. Fork, and M. A. Pollack. Locking of He[Single Bond]Ne laser modes induced by synchronous intracavity modulation. *Appl. Phys. Lett.*, 5:4–5, 1964.

[6] D. H. Sutter, G. Steinmeyer, L. Gallmann, N. Matuschek, F. Morier-Genoud, U. Keller, V. Scheuer, G. Angelow, and T. Tschudi. Semiconductor saturable-absorber mirror assisted Kerr-lens mode-locked Ti:sapphire laser producing pulses in the two-cycle regime. *Opt. Lett.*, 24:631–633, 1999.

[7] D. Strickland and G. Mourou. Compression of amplified chirped optical pulses. *Opt. Comm.*, 56:219–221, 1985.

[8] M. D. Perry, D. Pennington, B. C. Stuart, G. Tietbohl, J. A. Britten, C. Brown, S. Herman, B. Golick, M. Kartz, J. Miller, H. T. Powell, M. Vergino, and V. Yanovsky. Petawatt laser pulses. *Opt. Lett.*, 24:160–162, 1999.

[9] V. Yanovsky, V. Chvykov, G. Kalinchenko, P. Rousseau, T. Planchon, T. Matsuoka, A. Maksimchuk, J. Nees, G. Cheriaux, G. Mourou, and K. Krushelnick. Ultra-high intensity- 300-TW laser at 0.1 Hz repetition rate. *Opt. Express*, 16:2109–2114, 2008.

[10] L. V. Keldysh. Ionization in the field of a strong electromagnetic wave. *Sov. Phys. JETP*, 20:1307, 1965.

[11] K. J. Schafer, B. Yang, L. F. DiMauro, and K. C. Kulander. Above threshold ionization beyond the high harmonic cutoff. *Phys. Rev. Lett.*, 70:1599–1602, 1993.

[12] P. B. Corkum. Plasma perspective on strong field multiphoton ionization. *Phys. Rev. Lett.*, 71:1994–1997, 1993.

[13] P. M. Paul, E. S. Toma, P. Breger, G. Mullot, F. Auge, Ph. Balcou, H. G. Muller, and P. Agostini. Observation of a Train of Attosecond Pulses from High Harmonic Generation. *Science*, 292:1689–1692, 2001.

[14] M. Hentschel, R. Kienberger, Ch. Spielmann, G. A. Reider, N. Milosevic, T. Brabec, P. Corkum, U. Heinzmann, M. Drescher, and F. Krausz. Attosecond metrology. *Nature*, 414:509–513, 2001.

[15] J. L. Krause, K. J. Schafer, and K. C. Kulander. High-order harmonic generation from atoms and ions in the high intensity regime. *Phys. Rev. Lett.*, 68:3535–3538, 1992.

[16] E. Goulielmakis, M. Schultze, M. Hofstetter, V. S. Yakovlev, J. Gagnon, M. Uiberacker, A. L. Aquila, E. M. Gullikson, D. T. Attwood, R. Kienberger, F. Krausz, and U. Kleineberg. Single-Cycle Nonlinear Optics. *Science*, 320:1614–1617, 2008.

[17] S. V. Bulanov, N. M. Naumova, and F. Pegoraro. Interaction of an ultrashort, relativistically strong laser pulse with an overdense plasma. *Phys. Plasmas*, 1:745–757, 1994.

[18] N. M. Naumova, J. A. Nees, I. V. Sokolov, B. Hou, and G. A. Mourou. Relativistic Generation of Isolated Attosecond Pulses in a λ^3 Focal Volume. *Phys. Rev. Lett.*, 92:063902, 2004.

[19] B. Dromey, M. Zepf, A. Gopal, K. Lancaster, M. S. Wei, K. Krushelnick, M. Tatarakis, N. Vakakis, S. Moustaizis, R. Kodama, M. Tampo, C. Stoeckl, R. Clarke, H. Habara, D. Neely, S. Karsch, and P. Norreys. High harmonic generation in the relativistic limit. *Nat. Phys.*, 2:456–459, 2006.

[20] J. E. Rothenberg and D. Grischkowsky. Measurement of optical phase with subpicosecond resolution by time-domain interferometry. *Opt. Lett.*, 12:99–101, 1987.

[21] K. Naganuma, K. Mogi, and H. Yamada. General method for ultrashort light pulse chirp measurement. *IEEE J. Quant. Elect.*, 25:1225–1233, 1989.

[22] J. W. Nicholson and W. Rudolph. Noise sensitivity and accuracy of femtosecond pulse retrieval by phase and intensity from correlation and spectrum only (PICASO). *J. Opt. Soc. Am. B*, 19:330–339, 2002.

[23] J. Chung and A.M. Weiner. Ambiguity of ultrashort pulse shapes retrieved from the intensity autocorrelation and the power spectrum. *IEEE J. Sel. Top. Quant. Elect.*, 7:656–666, 2001.

[24] K. W. DeLong, R. Trebino, J. Hunter, and W. E. White. Frequency-resolved optical gating with the use of second-harmonic generation. *J. Opt. Soc. Am. B*, 11:2206–2215, 1994.

[25] C. Iaconis and I. A. Walmsley. Spectral phase interferometry for direct electric-field reconstruction of ultrashort optical pulses. *Opt. Lett.*, 23:792–794, 1998.

[26] A. Baltuška, M. S. Pshenichnikov, and D. A. Wiersma. Amplitude and phase characterization of 4.5-fs pulses by frequency-resolved optical gating. *Opt. Lett.*, 23:1474–1476, 1998.

[27] L. Gallmann, D. H. Sutter, N. Matuschek, G. Steinmeyer, U. Keller, C. Iaconis, and I. A. Walmsley. Characterization of sub-6-fs optical pulses with spectral phase interferometry for direct electric-field reconstruction. *Opt. Lett.*, 24:1314–1316, 1999.

[28] A. Euteneuer, H. Giessen, and M. Hofmann. U.S. Patent No. 6,671,053, International Patent No. WO 00/77482 A1 (filed 21 December, 2000).

[29] H. Mashiko, A. Suda, and K. Midorikawa. All-reflective interferometric autocorrelator for the measurement of ultra-short optical pulses. *Appl. Phys. B*, 76:525–530, 2003.

[30] I. Z. Kozma, P. Baum, U. Schmidhammer, S. Lochbrunner, and E. Riedle. Compact autocorrelator for the online measurement of tunable 10 femtosecond pulses. *Rev. Sci. Instrum.*, 75:2323–2327, 2004.

[31] P. Tzallas, D. Charalambidis, N. A. Papadogiannis, K. Witte, and G. D. Tsakiris. Direct observation of attosecond light bunching. *Nature*, 426:267–271, 2003.

[32] E. Goulielmakis, G. Nersisyan, N. A. Papadogiannis, D. Charalambidis, G. D. Tsakiris, and K. Witte. A dispersionless Michelson interferometer for the characterization of attosecond pulses. *Appl. Phys. B*, 74:197–206, 2002.

[33] Diana C. Skigin, Hung Loui, Zoya Popovic, and Edward F. Kuester. Bandwidth control of forbidden transmission gaps in compound structures with subwavelength slits. *Phys. Rev. E*, 76:016604, 2007.

[34] J. K. Ranka, A. L. Gaeta, A. Baltuška, M. S. Pshenichnikov, and D. A. Wiersma. Autocorrelation measurement of 6-fs pulses based on the two-photon-induced photocurrent in a GaAsP photodiode. *Opt. Lett.*, 22:1344–1346, 1997.

[35] Alexandre M. Streltsov, Jinendra K. Ranka, and Alexander L. Gaeta. Femtosecond ultraviolet autocorrelation measurements based on two-photon conductivity in fused silica. *Opt. Lett.*, 23:798–800, 1998.

[36] P. M. Sandvik, D. Walker, P. Kung, K. Mi, F. Shahedipour, V. Kumar, X. Zhang, J. E. Diaz, C. L. Jelen, and M. Razeghi. Solar-blind $Al_xGa_{1-x}N$ p-i-n photodetectors grown on LEO and non-LEO GaN. *Photodetectors: Materials and Devices V*, 3948:265–272, 2000.

[37] A. Braun, G. Korn, X. Liu, D. Du, J. Squier, and G. Mourou. Self-channeling of high-peak-power femtosecond laser pulses in air. *Opt. Lett.*, 20:73–75, 1995.

[38] A. Couairon and A. Mysyrowicz. Femtosecond filamentation in transparent media. *Phys. Rep.*, 441:47–189, 2007.

[39] S. L. Chin, S. A. Hosseini, Q. Luo W. Liu, F. Théberge, N. Aközbek, A. Becker, V. P. Kandidov, O. G. Kosareva, and H. Schroeder. The propagation of powerful femtosecond laser pulses in opticalmedia: physics, applications, and new challenges. *Can. J. Phys.*, 83:863–905, 2005.

[40] A. Couairon, J. Biegert, C. P. Hauri, W. Kornelis, F. W. Helbing, U. Keller, and A. Mysyrowicz. Self-compression of ultra-short laser pulses down to one optical cycle by filamentation. *J. Mod. Optics*, 53:75–85, 2006.

[41] A. Couairon, H. S. Chakraborty, and M. B. Gaarde. From single-cycle self-compressed filaments to isolated attosecond pulses in noble gases. *Phys. Rev. A*, 77:053814, 2008.

[42] M. Nisoli, S. De Silvestri, O. Svelto, R. Szipöcs, K. Ferencz, Ch. Spielmann, S. Sartania, and F. Krausz. Compression of high-energy laser pulses below 5 fs. *Opt. Lett.*, 22:522–524, 1997.

[43] Lukas Gallmann, Thomas Pfeifer, Mark J. Abel, Phillip M. Nagel, Daniel M. Neumark, and Stephen R. Leone. Direct Comparison of the Hollow-Core Fiber and Filamentation Techniques for Few-Cycle Pulse Generation. In *15th International Conference on Ultrafast Phenomena*, page MH18, 2006.

[44] G. Fibich and A. L. Gaeta. Critical power for self-focusing in bulk media and in hollow waveguides. *Opt. Lett.*, 25:335–337, 2000.

[45] C.P. Hauri, W. Kornelis, F.W. Helbing, A. Heinrich, A. Couairon, A. Mysyrowicz, J. Biegert, and U. Keller. Generation of intense, carrier-envelope phase-locked few-cycle laser pulses through filamentation. *Appl. Phys. B*, 79:673–677, 2004.

[46] A. Guandalini, P. Eckle, M. Anscombe, P. Schlup, J. Biegert, and U. Keller. 5.1 fs pulses generated by filamentation and carrier envelope phase stability analysis. *J. Phys. B*, 39:S257–S264, 2006.

[47] G. Stibenz, N. Zhavoronkov, and G. Steinmeyer. Self-compression of millijoule pulses to 7.8 fs duration in a white-light filament. *Opt. Lett.*, 31:274–276, 2006.

[48] S. Skupin, G. Stibenz, L. Berge, F. Lederer, T. Sokollik, M. Schnurer, N. Zhavoronkov, and G. Steinmeyer. Self-compression by femtosecond pulse filamentation: Experiments versus numerical simulations. *Phys. Rev. E*, 74:056604, 2006.

[49] A. McPherson, G. Gibson, H. Jara, U. Johann, T. S. Luk, I. A. McIntyre, K. Boyer, and C. K. Rhodes. Studies of multiphoton production of vacuum-ultraviolet radiation in the rare gases. *J. Opt. Soc. Am. B*, 4:595–601, 1987.

[50] M. Ferray, A. L'Huillier, X. F. Li, L. A. Lompre, G. Mainfray, and C. Manus. Multiple-harmonic conversion of 1064 nm radiation in rare gases. *J. Phys. B*, 21:L31–L35, 1988.

[51] J. L. Krause, K. J. Schafer, and K. C. Kulander. Calculation of photoemission from atoms subject to intense laser fields. *Phys. Rev. A*, 45:4998–5010, 1992.

[52] T. F. Gallagher. Above-Threshold Ionization in Low-Frequency Limit. *Phys. Rev. Lett.*, 61:2304–2307, 1988.

[53] S. Augst, D. Strickland, D. D. Meyerhofer, S. L. Chin, and J. H. Eberly. Tunneling ionization of noble gases in a high-intensity laser field. *Phys. Rev. Lett.*, 63:2212–2215, 1989.

[54] J. Tate, T. Auguste, H. G. Muller, P. Salieres, P. Agostini, and L. F. DiMauro. Scaling of Wave-Packet Dynamics in an Intense Midinfrared Field. *Phys. Rev. Lett.*, 98:013901, 2007.

[55] K. D. Schultz, C. I. Blaga, R. Chirla, P. Colosimo, J. Cryan, A. M. March, C. Roedig, E. Sistrunk, J. Tate, J. Wheeler, P. Agostini, and L. F. Dimauro. Strong field physics with long wavelength lasers. *J. Mod. Optics*, 54:1075–1085, 2007.

[56] J. San Román, L. Plaja, and L. Roso. Relativistic quantum dynamics of a localized Dirac electron driven by an intense-laser-field pulse. *Phys. Rev. A*, 64:063402, 2001.

[57] Q. Su, B. A. Smetanko1, and R. Grobe. Wave Packet Motion in Relativistic Electric Fields. *Laser Phys.*, 8:93, 1998.

[58] T. O. Clatterbuck, C. Lyngå, P. M. Paul, L. F. DiMauro, M. B. Gaarde, K. J. Schafer, P. Agostini, K. C. Kulander, and I. Walmsley. Yield and temporal characterization of high-order harmonics from intense midinfrared excitation of a cesium vapor. *Phys. Rev. A*, 69:033807, 2004.

[59] Y. Mairesse and F. Quéré. Frequency-resolved optical gating for complete reconstruction of attosecond bursts. *Phys. Rev. A*, 71:011401, 2005.

[60] H. G. Muller. Reconstruction of attosecond harmonic beating by interference of two-photon transitions. *Appl. Phys. B*, 74:S17, 2002.

[61] J. Itatani, F. Quéré, G. L. Yudin, M. Yu. Ivanov, F. Krausz, and P. B. Corkum. Attosecond Streak Camera. *Phys. Rev. Lett.*, 88:173903, 2002.

[62] M. Lewenstein, Ph. Balcou, M. Yu. Ivanov, A. L'Huillier, and P. B. Corkum. Theory of high-harmonic generation by low-frequency laser fields. *Phys. Rev. A*, 49:2117–2132, 1994.

[63] M. Lewenstein, P. Salières, and A. L'Huillier. Phase of the atomic polarization in high-order harmonic generation. *Phys. Rev. A*, 52:4747–4754, 1995.

[64] W. Becker, A. Lohr, and M. Kleber. Effects of rescattering on above-threshold ionization. *J. Phys. B*, 27:L325–L332, 1994.

[65] P. Salieres, B. Carre, L. Le Deroff, F. Grasbon, G. G. Paulus, H. Walther, R. Kopold, W. Becker, D. B. Milosevic, A. Sanpera, and M. Lewenstein. Feynman's Path-Integral Approach for Intense-Laser-Atom Interactions. *Science*, 292:902–905, 2001.

[66] P. Antoine, A. L'Huillier, and M. Lewenstein. Attosecond Pulse Trains Using High-Order Harmonics. *Phys. Rev. Lett.*, 77:1234–1237, 1996.

[67] M. B. Gaarde and K. J. Schafer. Space-Time Considerations in the Phase Locking of High Harmonics. *Phys. Rev. Lett.*, 89:213901, 2002.

[68] Y. Mairesse, A. de Bohan, L. J. Frasinski, H. Merdji, L. C. Dinu, P. Monchicourt, P. Breger, M. Kovačev, T. Auguste, B. Carré, H. G. Muller, P. Agostini, and P. Salières. Optimization of Attosecond Pulse Generation. *Phys. Rev. Lett.*, 93:163901, 2004.

[69] K. Varjú, Y. Mairesse, B. Carré, M. B. Gaarde, P. Johnsson, S. Kazamias, R. López-Martens, J. Mauritsson, K. J. Schafer, Ph. Balcou, A. L'huillier, and P. Salières. Frequency chirp of harmonic and attosecond pulses. *J. Mod. Optics*, 52:379–394, 2005.

[70] Y. Mairesse, A. de Bohan, L. J. Frasinski, H. Merdji, L. C. Dinu, P. Monchicourt, P. Breger, M. Kovacev, R. Taieb, B. Carre, H. G. Muller, P. Agostini, and P. Salieres. Attosecond Synchronization of High-Harmonic Soft X-rays. *Science*, 302:1540–1543, 2003.

[71] J. Wildenauer. Generation of the ninth, eleventh, and fifteenth harmonics of iodine laser radiation. *J. Appl. Phys.*, 62:41–48, 1987.

[72] E. Power, J. Pentland, J. Nees, C. P. Hauri, M. Merano, R. Lopez-Martens, and G. Mourou. All-reflective high fringe contrast autocorrelator for measurement of ultrabroadband optical pulses. *Opt. Lett.*, 31:3514–3516, 2006.

[73] C. P. Hauri, T. Ruchon, F. Canova, E. Power, A. L'Huillier, and R. López-Martens. Self-compression by ultrashort pulses in filaments. In *Conference on Lasers and Electro-Optics*, page JThE5, 2006.

[74] C. P. Hauri, R. B. López-Martens, C. I. Blaga, K. D. Schultz, J. Cryan, R. Chirla, P. Colosimo, G. Doumy, A. M. March, C. Roedig, E. Sistrunk, J. Tate, J. Wheeler, L. F. DiMauro, and E. P. Power. Intense self-compressed, self-phase-stabilized few-cycle pulses at 2 μm from an optical filament. *Opt. Lett.*, 32:868–870, 2007.

[75] A. Papoulis. *The Fourier Integral and its Applications*. McGraw-Hill, 1962.

[76] A. Baltuška, A. Pugzlys, M. Pshenichnikov, and D. A. Wiersma. *Conference on Lasers and Elecro-Optics*, pages 264–265, 1999.

[77] W. H. Press, S. A. Teukolsky, W. T. Vetterling, and B. P. Flannery. *Numerical Recipes in C, 2nd Ed.* Cambridge University Press, Cambridge, England, 1995.

[78] J. W. Nicholson, F. G. Omenetto, D. J. Funk, and A. J. Taylor. Evolving FROGS: phase retrieval from frequency-resolved optical gating measurements by use of genetic algorithms. *Opt. Lett.*, 24:490–492, 1999.

[79] B. J. Pearson, J. L. White, T. C. Weinacht, and P. H. Bucksbaum. Coherent control using adaptive learning algorithms. *Phys. Rev. A*, 63:063412, 2001.

[80] W. H. Press, B. P. Flannery, S. A. Teukolsky, and W. T. Vetterling. *Numerical Recipes in FORTRAN: The Art of Scientific Computing, 2nd ed.* Cambridge University Press, Cambridge, England, 1992.

[81] M. Matsumoto and T. Nishimura. Mersenne Twister: A 623-Dimensionally Equidistributed Uniform Pseudo-Random Number Generator. *ACM Transactions on Modeling and Computer Simulation*, 8:3–30, 1998.

[82] Intel Corporation. *Intel Math Kernel Library Reference Manual*, March 2007.

[83] R. Chandra, R. Menon, L. Dagum, D. Kohr, D. Maydan, and J. McDonald. *Parallel Programming in OpenMP*. Morgan Kaufmann, 2000.

[84] A. V. Smith. SNLO nonlinear optics code available from A.V. Smith. Sandia National Laboratories, Albuquerque, NM 87185-1423.

[85] L. T. Vuong, R. B. López-Martens, C. P. Hauri, and A. L. Gaeta. Spectral reshaping and pulse compression via sequential filamentation in gases. *Opt. Express*, 16:390–401, 2008.

[86] D. P. Shelton. Nonlinear-optical susceptibilities of gases measured at 1064 and 1319 nm. *Phys. Rev. A*, 42:2578–2592, 1990.

[87] D. Close, C. Giuliano, R. Hellwarth, L. Hess, F. McClung, and W. Wagner. 8A2–The self-focusing of light of different polarizations. *Quantum Electronics, IEEE Journal of*, 2:553–557, 1966.

[88] G. Fibich and B. Ilan. Self-focusing of circularly polarized beams. *Phys. Rev. E*, 67:036622, 2003.

[89] S. Stagira, E. Priori, G. Sansone, M. Nisoli, S. De Silvestri, and Ch. Gadermaier. Nonlinear guided propagation of few-optical-cycle laser pulses with arbitrary polarization states. *Phys. Rev. A*, 66:033810, 2002.

[90] M. Nurhuda and E. van Groesen. Effects of delayed Kerr nonlinearity and ionization on the filamentary ultrashort laser pulses in air. *Phys. Rev. E*, 71:066502, 2005.

[91] A. Baltuška, T. Fuji, and T. Kobayashi. Controlling the Carrier-Envelope Phase of Ultrashort Light Pulses with Optical Parametric Amplifiers. *Phys. Rev. Lett.*, 88:133901, 2002.

[92] T. Fuji, Alexander Apolonski, and Ferenc Krausz. Self-stabilization of carrier-envelope offset phase by use of difference-frequencygeneration. *Opt. Lett.*, 29:632–634, 2004.

[93] C. Manzoni, G. Cerullo, and S. De Silvestri. Ultrabroadband self-phase-stabilized pulses by difference-frequencygeneration. *Opt. Lett.*, 29:2668–2670, 2004.

[94] K. Wu, X. Yang, and H. Zeng. All-optical stabilization of carrier-envelope phase by use of difference frequency generation with seeded amplification of colored conical emission. *Appl. Phys. B*, 88:189–192, 2007.

[95] C. Manzoni, D. Polli, G. Cirmi, D. Brida, S. De Silvestri, and G. Cerullo. Tunable few-optical-cycle pulses with passive carrier-envelope phase stabilization from an optical parametric amplifier. *Appl. Phys. Lett.*, 90:171111, 2007.

[96] C. Vozzi, C. Manzoni, F. Calegari, E. Benedetti, G. Sansone, G. Cerullo, M. Nisoli, S. De Silvestri, and S. Stagira. Characterization of a high-energy self-phase-stabilized near-infrared parametric source. *J. Opt. Soc. Am. B*, 25:B112–B117, 2008.

[97] G. Cirmi, C. Manzoni, D. Brida, S. De Silvestri, and G. Cerullo. Carrier-envelope phase stable, few-optical-cycle pulses tunable from visible to near IR. *J. Opt. Soc. Am. B*, 25:B62–B69, 2008.

[98] A. Baltuška, Th. Udem, M. Uiberacker, M. Hentschel, E. Goulielmakis, Ch. Gohle, R. Holzwarth, V. S. Yakovlev, A. Scrinzi, T. W. Hansch, and F. Krausz. Attosecond control of electronic processes by intense light fields. *Nature*, 421:611–615, 2003.

[99] M. Kakehata, H. Takada, Y. K., K. Torizuka, Y. Fujihira, T. Homma, and H. Takahashi. Single-shot measurement of carrier-envelope phase changes by spectral interferometry. *Opt. Lett.*, 26:1436–1438, 2001.

[100] J. Mauritsson, P. Johnsson, R. López-Martens, K. Varjú, W. Kornelis, J. Biegert, U. Keller, M. B. Gaarde, K. J. Schafer, and A. L'Huillier. Measurement and control of the frequency chirp rate of high-order harmonic pulses. *Phys. Rev. A*, 70:021801, 2004.

[101] T. S. Clement, A. J. Taylor, and D. J. Kane. Single-shot measurement of the amplitude and phase of ultrashort laser pulses in the violet. *Opt. Lett.*, 20:70–72, 1995.

[102] D. J. Kane and R. Trebino. Characterization of arbitrary femtosecond pulses using frequency-resolved optical gating. *IEEE J. Quant. Elect.*, 29:571–579, 1993.

[103] B. A. Richman, K. W. DeLong, and R. Trebino. Temporal characterization of the Stanford mid-IR FEL micropulses by FROG. *Nuc. Instr. and Methods in Phys. Research Sec. A*, 358:268–271, 1995.

[104] R. Trebino and D. J. Kane. Using phase retrieval to measure the intensity and phase of ultrashort pulses: frequency-resolved optical gating. *J. Opt. Soc. Am. A*, 10:1101–1111, 1993.

[105] B. Kohler, V. V. Yakovlev, K. R. W., J. Squier, K. W. DeLong, and R. Trebino. Phase and intensity characterization of femtosecond pulses from a chirped-pulse amplifier by frequency-resolved optical gating. *Opt. Lett.*, 20:483–485, 1995.

[106] K. W. DeLong, R. Trebino, and D. J. Kane. Comparison of ultrashort-pulse frequency-resolved-optical- gating traces for three common beam geometries. *J. Opt. Soc. Am. B*, 11:1595–1608, 1994.

[107] D. J. Kane and R. Trebino. Single-shot measurement of the intensity and phase of an arbitrary ultrashort pulse by using frequency-resolved optical gating. *Opt. Lett.*, 18:823–825, 1993.

[108] D. J. Kane, A. J. Taylor, R. Trebino, and K. W. DeLong. Single-shot measurement of the intensity and phase of a femtosecond UV laser pulse with frequency-resolved optical gating. *Opt. Lett.*, 19:1061–1063, 1994.

[109] J. N. Sweetser, D. N. Fittinghoff, and R. Trebino. Transient-grating frequency-resolved optical gating. *Opt. Lett.*, 22:519–521, 1997.

[110] R. Trebino, C. Barker, and A. Siegman. Tunable-laser-induced gratings for the measurement of ultrafast phenomena. *IEEE J. Quant. Elect.*, 22:1413–1430, 1986.

[111] T. Y. F. Tsang, M. A. Krumbugel, K. W. DeLong, D. N. Fittinghoff, and R. Trebino. Frequency-resolved optical-gating measurements of ultrashort pulses using surface third-harmonic generation. *Opt. Lett.*, 21, 1996.

[112] S. Linden, H. Giessen, and J. Kuhl. XFROG-A New Method for Amplitude and Phase Characterization of Weak Ultrashort Pulses. *Phys. Stat. Sol. (B)*, 206:119–124, 1998.

[113] S. Linden, J. Kuhl, and H. Giessen. Amplitude and phase characterization of weak blue ultrashort pulses by downconversion. *Opt. Lett.*, 24:569–571, 1999.

[114] C. Garrett and F. Robinson. Miller's phenomenological rule for computing nonlinear susceptibilities. *IEEE J. Quant. Elect.*, 2:328–329, 1966.

[115] P. Colosimo. *A Study of Wavelength Dependence of Strong-Field Optical Ionization.* PhD thesis, Stony Brook University, 2007.

[116] W. J. Tropf. Temperature-dependent refractive index models for BaF_2, CaF_2, MgF_2, SrF_2, LiF, NaF, KCI, ZnS, and ZnSe. *Opt. Eng.*, 34:1369–1373, 1995.

[117] T. Yamamuro, S. Sato, T. Zenno, N. Takeyama, H. Matsuhara, I. Maeda, and Y. Matsueda. Measurement of refractive indices of 20 optical materials at low temperatures. *Opt. Eng.*, 45:083401, 2006.

[118] P. Laporte, J. L. Subtil, M. Courbon, M. Bon, and L. Vincent. Vacuum-ultraviolet refractive index of LiF and MgF_2 in the temperature range 80-300 K. *J. Opt. Soc. Am.*, 73:1062–1069, 1983.

[119] J. H. Burnett, R. Gupta, and U. Griesmann. Absolute refractive indices and thermal coefficients of CaF_2, SrF_2, BaF_2, and LiF near 157 nm. *Appl. Opt.*, 41:2508–2513, 2002.

[120] J. C. Lagarias, J. A. Reeds, M. H. Wright, and P. E. Wright. Convergence Properties of the Nelder-Mead Simplex Method in Low Dimensions. *SIAM J. Optim.*, 9:112–147, 1998.

[121] B. Edlén. The Refractive Index of Air. *Metrologia*, 2:71–80, 1966.

[122] R. Muijlwijk. Update of the Edlén Formulae for the Refractive Index of Air. *Metrologia*, 25:189, 1988.

[123] P. E. Ciddor and R. J. Hill. Refractive index of air. 2. Group index. *Appl. Opt.*, 38:1663–1667, 1999.

[124] Y. Yamaoka, K. Minoshima, and H. Matsumoto. Direct measurement of the group refractive index of air with interferometry between adjacent femtosecond pulses. *Appl. Opt.*, 41:4318–4324, 2002.

[125] J. A. Stone and A. Stejskal. Using helium as a standard of refractive index: correcting errors in a gas refractometer. *Metrologia*, 41:189197, 2004.

[126] G. Łach, B. Jeziorski, and K. Szalewicz. Radiative Corrections to the Polarizability of Helium. *Phys. Rev. Lett.*, 92:233001, 2004.

[127] A. K. Bhatia and R. J. Drachman. Optical properties of helium including relativistic corrections. *Phys. Rev. A*, 58:4470–4472, 1998.

[128] J. J. Hurly and M. R. Moldover. Ab Initio Values of the Thermophysical Properties of Helium as Standards. *J. Res. N.I.S.T.*, 105:667–708, 2000.

[129] H. Koch, C. Hättig, H. Larsen, J. Olsen, , P. Jørgensen, B. Fernández, and A. Rizzo. The effect of intermolecular interactions on the electric properties of helium and argon. II. The dielectric, refractivity, Kerr, and hyperpolarizability second virial coefficients. *J. Chem. Phys.*, 111:10108–10118, 1999.

[130] D. J. Kane. Real time measurement of ultrashort laser pulses using principal component generalized projections. *IEEE J. Sel. Top. Quant. Elect.*, 4:278–284, 1998.

[131] D. J. Kane. Recent Progress Toward Real-Time Measurement of Ultrashort Laser Pulses. *IEEE J. Quant. Elect.*, 35:421–431, 1999.

[132] R. Trebino and D. J. Kane. Using phase retrieval to measure the intensity and phase of ultrashort pulses: frequency-resolved optical gating. *J. Opt. Soc. Am. A*, 10:1101–1111, 1993.

[133] D. J. Kane and R. Trebino. Single-shot measurement of the intensity and phase of an arbitrary ultrashort pulse by using frequency-resolved optical gating. *Opt. Lett.*, 18:823–825, 1993.

[134] H. Anton. *Elementary Linear Algebra.* 2nd Ed. New York: Wiley, 1977.

[135] R. A. Altes. Detection, estimation, and classification with spectrograms. *J. Acoust. Soc. Am.*, 67:1232–1246, 1980.

[136] S. Nawab, T. Quatieri, and Jae Lim. Signal reconstruction from short-time Fourier transform magnitude. *IEEE Trans. Acoustics, Speech, Sig. Process.*, 31:986–998, 1983.

[137] R. Trebino. *Frequency Resolved Optical Gating: The Measurement of Ultrashort Laser Pulses.* Kluwer Academic Publishers, 2000.

[138] R. B. Miles and S. E. Harris. Optical Third-Harmonic Generation in Alkali Metal Vapors. *IEEE J. Quant. Elect.*, pages 470–484, 1973.

[139] G. Pichler, S. Milošević, D. Viža, and R. Beuc. Diffuse bands in the visible absorption spectra of dense alkali vapours. *J. Phys. B*, 16:4619–4631, 1983.

[140] Z. Wang, E. Zeek, R. Trebino, and P. Kvam. Determining error bars in measurements of ultrashort laser pulses. *J. Opt. Soc. Am. B*, 20:2400–2405, 2003.

[141] Z. Wang, E. Zeek, R. Trebino, and P. Kvam. Beyond error bars: Understanding uncertainty in ultrashort-pulse frequency-resolved-optical-gating measurements in the presence of ambiguity. *Opt. Express*, 11:3518–3527, 2003.

[142] M. Gaarde. Time-frequency representations of high order harmonics. *Opt. Express*, 8:529–536, 2001.